JOHANNES KEPLER
UNIVERSITY LINZ

Submitted by
Christoph Putz, BSc.

Submitted at
Institute of Experimental Physics, Department of Soft Matter Physics (SoMaP)

Supervisor
Univ.-Prof. DI Dr. Martin Kaltenbrunner

Co Supervisor
Assoc. Univ.-Prof. DI Dr. Markus Clark Scharber

October 2020

FLEXIBLE ORGANIC SOLAR CELLS BASED ON NON-FULLERENE ACCEPTORS

Master Thesis
to obtain the academic degree of
Diplom-Ingenieur (DI)
in the Master's Program
Technical Physics

JOHANNES KEPLER
UNIVERSITY LINZ
Altenberger Straße 69
4040 Linz, Austria
jku.at

Eidesstattliche Erklärung

Ich erkläre an Eides statt, dass ich die vorliegende Masterarbeit selbstständig und ohne fremde Hilfe verfasst, andere als die angegebenen Quellen und Hilfsmittel nicht benutzt bzw. die wörtlich oder sinngemäß entnommenen Stellen als solche kenntlich gemacht habe.

Die vorliegende Masterarbeit ist mit dem elektronisch übermittelten Textdokument identisch.

Linz, Oktober 2020

Christoph Putz, BSc

Acknowledgments

First of all, I wish to express my sincere thanks to Assoc. Prof. DI Dr. Markus Scharber for his patience, motivation, immense knowledge, and for all the help to my work from beginning to the end.

I want to thank Univ. Prof. DI Dr. Martin Kaltenbrunner for allowing me to perform my master thesis as part of the SOMAP team. The door to his office was always open whenever I had a question about my research or writing.

I also want to thank o. Univ. Prof. Mag. Dr. DDr. h.c. Niyazi Serdar Sariciftci, for giving me the opportunity to perform this master thesis as part of the LIOS work group and for providing me with all the necessary facilities for the research.

I want to especially thank DI Jakob Hofinger for his time, spending countless hours discussing results, his kindness, and all the help throughout this work.

Big thanks to DI Katarina Gugujonović, DI Felix Mayr, DI Dominik Wielend, and Dr. Hathaichanok Seelajaroen for cheering me up when things didn't work and for all the fun we have had in our office.

My grateful thanks are also extended to Dr. Bekele Hailegnaw Teklemariam, for your time discussing results and all your motivational words.

I also want to thank DI Stepan Demchyshyn, and Hannes Pöhl, MSc for all your help throughout this work.

I would like to thank all members of LIOS and SOMAP for their wonderful work and kind support.

Special thanks go to the technical staff of the institute, particularly, Patrick John Denk for all his work and teaching me to make my first solar cell. I am very thankful for Dr. Munise Cobet and her hard work keeping the laboratory equipment in perfect condition.

Finally, I want to thank my family: my father for being an inspirational person and my mother for always being there for me. My sister and girlfriend, for the motivation, whenever things were complicated.

Abstract

During the past few years, organic solar cells (OSCs) based on non-fullerene acceptors (NFAs) have rapidly drawn the attention away from their fullerene acceptor (FA)-based counterparts. They show better open-circuit voltage, short-circuit current, and fill factor. While the molecular structures of NFAs and FAs are clearly different, the fundamental differences in the working mechanisms of the corresponding solar cells are not well understood. The presented work aims to elucidate this further. For this purpose, two frequently published NFAs (namely IT4F and EH-IDTBR) paired with two donor polymers (PBDB-T-2F and PTB7-Th) are compared with their FA (PC71BM)-based counterparts. The NFA-donor combinations were chosen due to their reproducible power conversion efficiency (PCE) of up to 13%.

In the first part of this work, a range of complementary steady-state and frequency domain techniques have been used to study the optoelectronic differences between NFAs- and FAs-based OSCs on rigid substrates. The photovoltaic performances were investigated with standardized device characterization methods. The charge carrier recombination resistance and effective electron lifetime were studied with intensity-modulated photovoltage spectroscopy (IMVS). Dynamic processes on the microsecond timescales have been observed. Sensitive measurements of the photocurrent ($\mathrm{EQE}_{\mathrm{PV}}$ measurement) were performed to gain a deeper understanding of the energy loss channels within the device. Low-temperature magneto-optical measurements were carried out to get a deeper insight into the radiative decay channels of organic semiconductors and to investigate fundamental mechanisms of magnetic response from nonmagnetic organic materials.

In the second part of this thesis, the focus was put on exploring the excellent applicability of NFAs for the fabrication of ultrathin flexible OSCs. The commonly used transparent indium-tin-oxide (ITO) electrodes of rigid devices have severe drawbacks for flexible OSCs. They are often accompanied by costly high-temperature vacuum processing techniques and restricted mechanical flexibility. The development of alternative liquid-processed transparent electrodes is of vital importance. In this work, a high conductive polymer namely poly(3,4-ethylenedioxythiophene):polystyrene sulphonate (PEDOT:PSS PH1000), and a silver nanowire-graphene (NW-graphene) mixture, are used as an alternative to the commonly used ITO electrodes. Based on the PBDB-T-2F:IT4F active layer materials, PCEs of up to 12 % are demonstrated for ultrathin ($< 2\,\mu$m) ITO and ITO-free flexible substrates. In addition, a straight-forward fabrication technique for laboratory-scale ultrathin and ITO-free based flexible OSCs is presented.

Kurzfassung

In den letzten Jahren haben organische Solarzellen (OSCs) auf der Basis von Nicht-Fulleren-Akzeptoren (NFAs) die Aufmerksamkeit von ihren auf Fulleren (FA)-basierenden Gegenstücke schnell auf sich gezogen. Sie zeigen nicht nur eine bessere Effizienz, sondern auch eine höhere Leerlaufspannung, Kurzschlussstrom und Füllfaktor. Während die Unterschiede in den molekularen Strukturen von NFAs und FAs bekannt sind, sind die grundlegenden Unterschiede in den Arbeitsmechanismen der entsprechenden Solarzellen noch nicht vollständig verstanden. Die vorgestellte Arbeit soll dies weiter erläutern. Zu diesem Zweck werden zwei häufig diskutierte NFAs (IT4F und EH-IDTBR), gemischt mit zwei Donorpolymeren (PBDB-T-2F und PTB7-Th), mit den auf FA (PC71BM)- basierenden Solarzellen verglichen. Die NFA-Donor Materialkombinationen wurden ausgewählt, da sie bei hoher Reproduzierbarkeit bemerkenswerte Wirkungsgrade von bis zu 13 % aufweisen.

Im ersten Teil dieser Arbeit wurde eine Reihe von optischen- und frequenzbasierten Techniken verwendet um die optoelektronischen Unterschiede zwischen NFAs und FAs auf starren Substraten zu untersuchen. Die photovoltaischen Eigenschaften wurden mit standardisierten Methoden zur Solarzellencharakterisierung untersucht. Der Rekombinationswiderstand der Ladungsträger und die effektive Elektronenlebensdauer wurden mit intensitätsmodulierter Photospannungsspektroskopie (IMVS) untersucht. Hierbei wurden dynamische Prozesse im Mikrosekundenbereich gemessen. Sensitive Messungen des Photostroms ($\mathrm{EQE_{PV}}$-Messung) wurden durchgeführt, um ein tieferes Verständnis der Energieverluste innerhalb der Solarzelle zu erhalten. Magnetooptische Niedriegtemperaturmessungen wurden durchgeführt, um einen Einblick in die strahlenden Rekombinationskanäle organischer Halbleiter zu erhalten. Darüber hinaus werden die grundlegende Mechanismen der Magnetfeldabhängigkeit von nichtmagnetischen organischen Materialien untersucht.

Im zweiten Teil dieser Arbeit lag der Schwerpunkt auf der Untersuchung der hervorragenden Anwendbarkeit von NFAs für die Herstellung ultradünner flexibler OSCs. Die bei starren Solarzellen erfolgreich eingesetzten transparenten Indium-Zinn-Oxid (ITO)-Elektroden, weisen teilweise große Nachteile für flexible OSCs auf. Sie werden häufig von kostspieligen Hochtemperatur-Vakuumverarbeitungstechniken und eingeschränkter mechanischer Flexibilität begleitet. Die Entwicklung alternativer flüssigkeitsprozessierter transparenter Elektroden ist von entscheidender Bedeutung. In dieser Arbeit werden ein hochleitfähiges Polymer, nämlich Poly (3,4-ethylendioxythiophen):Polystyrolsulfonat (PEDOT:PSS PH1000), und ein Silber-Nanodraht-Graphen (NW-Graphene) Gemisch als Alternative zu den üblichen ITO-Elektroden verwendet. Basierend auf den aktiven Schichtmaterialien PBDB-T-2F:IT4F werden Wirkungsgrade von bis zu 12 % für ultradünne ($< 2\,\mu$m) ITO- und ITO-freie flexible Substrate gemessen. Darüber hinaus wird eine einfache Herstellungstechnik für ultradünne und ITO-freie flexible organische Solarzellen vorgestellt.

Contents

1 Introduction to organic solar cells

After the discovery of high conductivity in perylene iodine in the 1950s, the field of organic semiconductors has become a relatively large area of research [1]. The first potential applications emerged when Tang et al. demonstrated the first working organic light-emitting diode (OLED) in 1986 [2]. Over the years, the unique properties of organic semiconductors such as thinness, flexibility, transparency, and ease of processing have led to many applications. Today's solar cell technologies can be divided into three so-called generations [3]. The first generation includes silicon solar cells made of poly– or monocrystalline silicon wafers with a thickness between 100 and 300 μm. Conventional module top efficiencies are 26% for monocrystalline solar cells, and 23% for polycrystalline solar cells [4]. A significant disadvantage of wafer technology is the high energy costs incurred in the production of high-purity silicon.

The second generation includes thin–film solar cells made of amorphous silicon, copper indium gallium diselenide (CIGS), or cadmium telluride/cadmium sulfide (CdTe / CdS). They are commercially available and enable large–scale production of solar modules with significantly reduced material expenditure. Despite the significantly lower material requirements, second–generation solar cells are rarely used as they often contain toxic materials like cadmium or rare ingredients such as tellurium.

The third-generation includes solar cell concepts such as tandem and concentrator solar cells. These enable efficiencies of over 30% [4]. Sean E. Shaheen expanded the definition of the third generation with an addition, which encompasses solar cell technologies with very low manufacturing costs [5]. The ability of low–cost solar cells arises through the use of cheap roll–to–roll printing techniques and photoactive layers made out of carbon–based conjugated polymer materials. In addition to dye synthesized solar cells, this area also includes the organic solar cells (OSCs) discussed in this work.

From the beginning 2000s, fullerene acceptors (FAs) were extensively used in OSCs. Besides their efficient percolation and high electron mobility, fullerene based solar cells encounter a limited efficiency. The energy levels are challenging to alter, and the optical bandgap cannot be tuned widely. Moreover, they show a weak absorption in the visible spectral region [6]. Small–molecule non–fullerene acceptors (NFAs) can easily overcome these deficiencies. Benefiting from two decades of experience in fullerene-based bulk heterojunction (BHJ) systems, in the past two years the community has made rapid progress on non-fullerene based solar cells. Today's OSCs can provide efficiencies of up to 18% and thus have the potential to further reduce the energy payback time to well under a year [7, 8]. They can be manufactured in custom–shaped modules for integration into roofs, facades and even clothing [9, 10].

2 Theoretical background

The following chapter provides an introduction to the fundamentals and physical processes of and in organic solar cells.

2.1 The sun as a radiation source

The surface temperature of the sun is about 5800 K, which is generated by the nuclear fusion process of hydrogen to helium. At this temperature, the radiated energy of the sun can be represented as that of a black body. The intensity of the emitted radiation (emitted power per unit area) of a black body depends on the wavelength λ and the temperature T, according to Plank's law of radiation [11]:

$$I_\lambda(\lambda, T)d\lambda = \left(\frac{2hc^2}{\lambda^5}\right) \cdot \frac{1}{e^{hc/\lambda kT} - 1}\,, \tag{2.1}$$

where $h = 6.62 \times 10^{-34}$ Js the Plank constant, $c = 3 \times 10^{8}$ m/s the speed of light in free space and $k = 1.38 \times 10^{-23}$ J/K the Boltzmann constant.

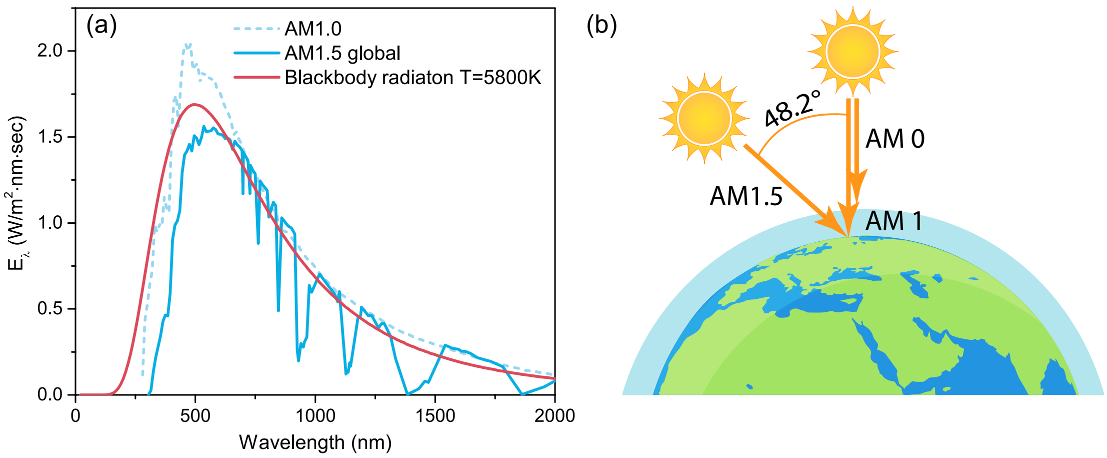

Figure 2.1: (a) Spectral radiation power of the sun compared to the blackbody radiation with a temperature $T = 5800$ K. (b) Schematic representation of the light paths for AM0, AM1.0 and AM1.5, respectively.

Fig. 2.1(a) compares the spectral radiation power density E_λ of a blackbody at 5800 K with the spectral distribution outside the earth's atmosphere and on the earth's surface [12]. Since the sun rays are not always perpendicular to the earth's surface, the so-called Air Mass (AM) is introduced as a measure of the weakening by the atmosphere. AM0 denotes the extraterrestrial radiation power in space. AM1 describes the radiation power of the sunlight at normal incidence, around the equator, and at sea level. A schematic representation of the different sunray light paths is shown in Fig. 2.1(b). Air mass 1.5 is of particular interest. Compared to AM1, 1.5 times the air mass has to be transmitted. The spectrum measured within the atmosphere also includes the absorptions through different molecules in the air. AM1.5 represents a global standard spectrum for the determination of the efficiency of a solar cell. This default spectrum is also defined in terms of temperature, total irradiance, and spectral irradiance. The standard temperature is 25 °C, and the total irradiance intensity is 100 mW cm^{-2}, which is also defined as one sun [13]. This standard spectrum can be easily simulated in a laboratory, with so–called solar–simulators, and solar cells can, therefore, be measured under uniform conditions.

2.2 Organic semiconductors

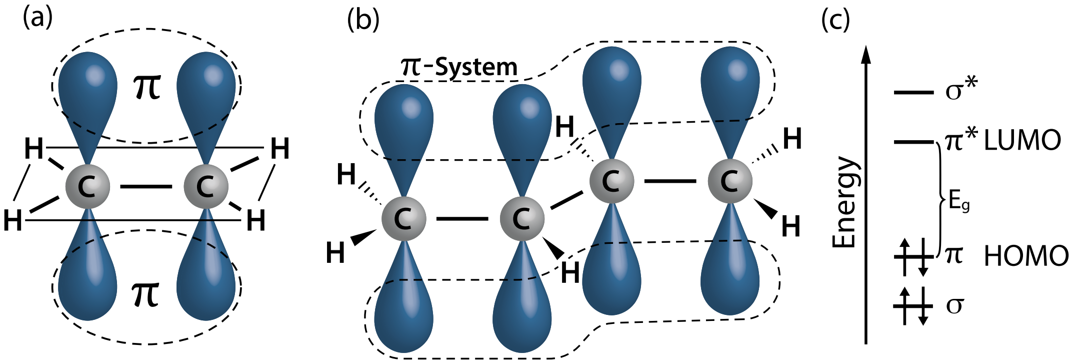

Figure 2.2: (a) The $2sp^2-$ hybridorbitals of the ethene molecule (C_2H_4). (b) $\pi-$ system of buta-1,3-diene. (c) Schematic energy level diagram. Redrawn from [14]

Organic semiconductors are molecular materials or polymers (i.e., macromolecules) that consist predominantly of hydrocarbon compounds possessing semiconductor properties [15]. Carbon atoms first require a particular configuration of the orbitals to be able to bond with each other [16]. A configuration like this results in the hybridization of the $2s-$ orbital and two of the three $2p-$ orbitals to three $2sp^2-$ orbitals. The simplest example of this is the ethene molecule (C_2H_4), in which each of the two carbon atoms has only three binding partners. An orbital model of the ethene molecule is shown in Fig. 2.2(a). Here the $2sp^2-$ hybrid orbitals are in plane with the carbon and hydrogen atoms. The $2sp^2-$ hybrid orbitals form $\sigma-$bonds. These stable covalent bonds form the backbone of a molecule and provide its stability. The not hybridized $2p_z-$ orbitals (blue) are perpendicular to the carbon-hydrogen plane. They are aligned parallel to each other and yield a binding $\pi-$molecular orbital and an antibonding π^*- molecular orbital. If single and double bonds are alternating on a molecule, which is the case for the buta-1,3,-diene molecule shown in Fig. 2.2(b), the $\pi-$bond is no longer strongly localized, and one can speak of a so-called $\pi-$conjugated system. The semiconducting properties are derived from that conjugated $\pi-$electron system. Delocalization allows the $\pi-$electrons to move freely throughout the conjugated molecule.

The energies of the electrons in the interacting orbitals can be illustrated by the term schema shown in Fig. 2.2(c). The highest occupied level π is represented as HOMO (highest occupied molecular orbital), and the lowest unoccupied level π^* is represented as LUMO (lowest unoccupied molecular orbital) of an unexcited molecule. Transitions between the HOMO and the LUMO are usually in the range of 1.5 to 3 eV and are responsible for the semiconducting properties of the molecules.

2.3 Operating principles of organic solar cells

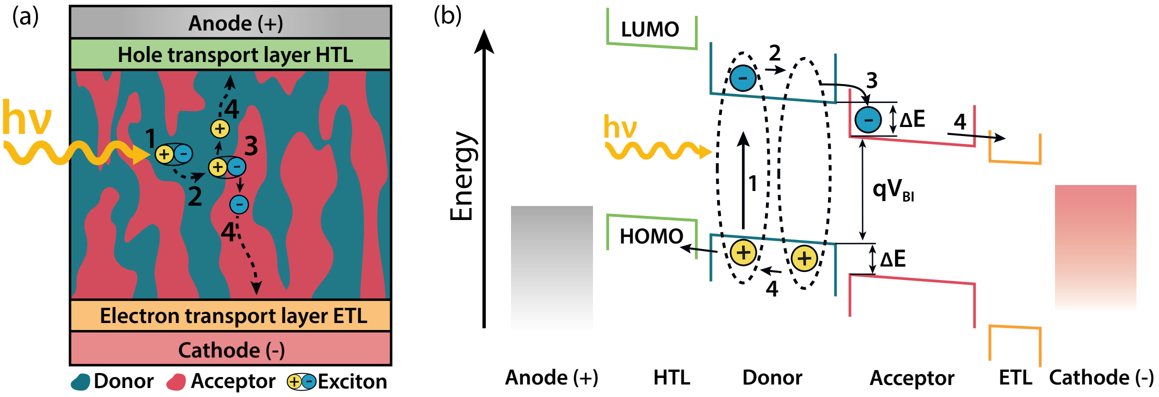

Figure 2.3: (a) Schematic of an inverted *Bulk–Heterojunction* (BHJ) solar cell structure. (b) Band diagram of an organic solar cell. (1) A photon of sufficient energy $h\nu$ is absorbed by the donor material in the active layer and an electron is excited from the HOMO into the LUMO of the polymer. (2) The charge carriers are bound in an exciton and diffuse to the interface of the acceptor. (3) The electron is transfered to the energetically lower LUMO level of the acceptor and the exciton is dissociated via CT– and CS–states. (4) The charge carriers diffuse to the corresponding electrodes under the force of a built–in potential V_{bi}. Redrawn and adapted from [14]

Converting solar energy into electrical energy in a solar cell includes the following steps schematically depicted in Fig. 2.3(a,b): (1) absorption of light and exciton generation, (2) exciton diffusion, (3) exciton dissociation, and (4) charge transport to the respective electrodes under the force of a built–in potential. The next chapter concentrates on these intermediate steps in organic semiconductors [17].

Absorption of light

An efficient solar cell is always accompanied by an effective absorption of light. Incident photons on a solar cell are either reflected at the surface, absorbed in the active material, or transmitted through the cell. For photovoltaic devices, it is evident that two of the named processes constitute a loss mechanism, and only absorbed photons can be converted into a photocurrent. The key parameter for the absorption of light is the so-called absorption coefficient α.

Organic semiconductors have a comparatively high absorption coefficient of about $10^5\,\mathrm{cm}^{-1}$ what makes it possible to absorb a significant part of the irradiated sunlight already with layer thicknesses of about 100 nm [18]. In optical absorption experiments, it is common to give the dimensionless product A of the absorption coefficient and the absorber thickness $A = \alpha \cdot z$, which is called the absorbance or optical density. However, the optical density is defined using the decadic logarithm and is therefore expressed with

$$\log\left(\frac{I}{I_0}\right) = \log T = -A\ , \tag{2.2}$$

where T is the transmittance of the sample.

The optical properties of organic semiconductors are primarily determined by the energy difference E_g between the HOMO and LUMO level. As with inorganic semiconductors, this can be termed an energy band gap. This band gap determines the broadness of the absorbed solar spectrum. A small bandgap results in a broad absorbed solar spectrum, while for large band gap materials, most of the solar spectrum is not absorbed. Nunzi J.M. et al. reported that a band gap of 1.1 eV is capable of absorbing 77 % of the irradiated solar spectrum [19]. Designing organic materials with low band gap is a crucial step to build highly efficient OSCs.

Exciton generation

A photon with an energy greater than the bandgap energy can excite an electron from the HOMO– into the LUMO–level of the semiconductor and generate an electron–hole pair. However, the charge carriers of the electron–hole pair are still bound by the Coulomb binding energy as a so–called exciton. In contrast to inorganic semiconductors, the resulting electron-hole pair is strongly bound and is usually located on only one molecule. Due to the high localization, it is therefore called a Frenkel–exciton. The exciton binding energy E_C can be calculated with

$$E_\mathrm{C} = \frac{e^4 \mu^*}{2(4\pi\varepsilon_0\varepsilon_\mathrm{r}\hbar)^2} \tag{2.3}$$

Here, e correspsonds to the elementary charge, ε_0 to the dielectric field constant, ε_r to the relative permittivity, μ^* to the effective mass of the electrons and $\hbar$ the reduced Planck constant. Due to the chemical structure, organic semiconductors show quite low relative permittivity (typical between 2 and 4). The exciton binding energy E_C is in the range of 0.3 to 1.0 eV [20]. This value is very high compared to the thermal energy at room temperature of about 25 meV. Therefore, the absorption of light in organic semiconductors does not automatically lead to free charge carriers, but first to Frenkel–excitons. These excitons are very immobile with diffusion lengths of only a few nanometres [21]. The materials are therefore also called excitonic semiconductors. If no dissociation occurs, the charge carriers recombine back to their ground state via radiative or nonradiative pathways.

Exciton diffusion

The existence of strongly bound excitonic excitation states has significant consequences for the use of organic semiconductors in devices. However, the challenge is to separate the excitons into free charge carriers. In this case, the excitons first need to diffuse to a donor–acceptor interface, where they can be split into negative and positive charges. The limiting parameter for this is the exciton lifetime and the associated diffusion length. Exciton diffusion lengths in organic semiconductors are typically in the range of $10-20$ nm [19]. Thus, small diffusion lengths are limiting the thickness of the active layer and the donor–acceptor phase separation length [22]. In order to increase the layer thickness of the absorber layer and thus the absorption of the solar cell, Yu et al. developed the concept of the bulk–heterojunction (BHJ) [23]. Therefore, the acceptor and donor materials are mixed in the same solution and deposited together during the device fabrication. Fig. 2.3(a) illustrates the morphology of the resulting interpenetrating structure of the material domains that form in the active layer. The size and structure of these material domains can be influenced by various process technologies and heat treatment methods. An efficient morphology has domain sizes in the range of the diffusion length and percolation paths to the corresponding electrodes.

Exciton dissociation

In order to separate the strongly bound charge carriers, either strong external electric fields or the local electrical fields which arise at the donor–acceptor interfaces must be present. The electrical field at this interfaces form due to significant changes in the potential energy of the donor and acceptors. Therefore, the neutral excitons can be effectively split into separate charges in such blends of conjugated donor materials and electron acceptors.

A small energy offset ΔE between the LUMO of the donor and the LUMO of the acceptor material for the electrons (see Fig. 2.3(b)) and a donor–HOMO and acceptor–HOMO energy–offset for the holes, of usually $-0.3\,\text{eV}$ is sufficient for an effective charge separation [24]. However, due to the short spatial distance, the charge carriers are still weakly bound by coulombic attraction in a so-called charge transfer state (CT state). If the charge carriers in the CT state have sufficient energy, they can dissociate through several charge-separated states (CS state). The charge carriers are spatially separated and dissociate into free charge carriers [25].

Charge carrier transport to the electrodes

A crucial point for an efficient OSC is the effective separation of the charge carriers and the transport to the respective electrodes. In inorganic semiconductors like silicon (Si) and germanium (Ge), the charge carriers travel as highly delocalized plane waves and therefore often high carrier mobilities μ, exceeding $1\,\text{cm}^2/\text{Vs}$, can be observed. In these materials, increasing temperature leads to reduced carrier mobility due to carrier scattering. The atoms within an organic semiconductor molecule are bonded to each other by conjugated $\pi-$bonds. The bonding energy of organic semiconductor molecules is of the same order as molecular vibrational energy at room temperature. In contrast to the strong covalent structure of inorganic semiconductors, the molecules in an organic semiconductor are held together mainly by weak Van der Waal's forces [15, 16]. Therefore, they exhibit lattice vibrations at relatively low energies ("soft" phonons), which are much more excited than within inorganic semiconductors and contribute to the scattering of the charge carriers [26]. Therefore, the charge carrier mobilities are many orders of magnitude lower than for crystals. In general, the values at room temperature are below $10^{-5}\,\text{cm}^2/\text{Vs}$. In addition, the distances between the molecules are sufficiently large for the molecular orbitals to overlap. In these systems, the charges move by incoherent hopping from one molecule or polymer chain to the next. This hopping transport differs from the band transport by an opposite temperature dependence: the hopping of the charge carriers is thermally assisted, thus the mobility increases with the temperature. The relationship between carrier mobility μ and temperature T can be expressed with

$$\mu = \mu_0 \exp\left[-\left(\frac{T_0}{T}\right)^{\frac{1}{\alpha}}\right], \text{with } \alpha \text{ between 1 and 4.} \tag{2.4}$$

The hopping transport of the electrons and holes is assisted by a driving–force that exists between the materials of the solar cell. The energy offset between the HOMO level of the donor, and the LUMO level of the acceptor material is called the built–in potential V_{BI}

$$V_{\mathrm{BI}} = \frac{1}{q}(E^{\mathrm{A}}_{\mathrm{LUMO}} - E^{\mathrm{D}}_{\mathrm{HOMO}}) \ . \tag{2.5}$$

Here, $E^{\mathrm{A}}_{\mathrm{LUMO}}$ is the LUMO energylevel of the acceptor material $E^{\mathrm{D}}_{\mathrm{HOMO}}$ the HOMO energylevel of the donor material, and q is the elementary charge.

A second contribution to the driving–force for the charge carriers exists through the electrochemical potential difference of the electrodes. Therefore, two electrodes with a high and a low work function, respectively, are used. The work function of the electrodes has to be chosen well to match the HOMO and LUMO levels of the donor and acceptor correctly (see Fig. 2.3(b)). Electron (ETL) and hole transport layers (HTL) are introduced between the organic semiconductor and metal interfaces to tune the electrochemical potential of the electrodes and to ensure that the charge carriers reach the correct electrodes.

Fig. 2.3 shows the shematic structure of a so–called *inverted* OSC. The structure is vice–versa for the so–called *standard* configuration.

If the charge carriers are finally collected by the electrodes, and the OSC is at open-circuit condition, the accumulated charge carriers form a potential difference V_{oc} which cancels out the built–in potential V_{BI}. The next chapter will discuss the origin of this potential V_{oc}, called open-circuit voltage.

2.4 Origin of the open–circuit voltage

The open–circuit voltage V_{oc} is a result of the energy difference between the electron e and the hole h quasi–Fermi energy level E_{Fe} and E_{Fh} under illumination.

$$V_{\mathrm{oc}} = \frac{1}{q}(E_{\mathrm{Fh}} - E_{\mathrm{Fe}}) \ . \tag{2.6}$$

It turned out, that in real OSCs, this is not the common case. Scharber et al. [27] found an empirical relationship between the built–in potential V_{BI} discussed in chapter 2.3 and the open–circuit voltage V_{oc} of the solar cell. Thus, V_{oc} can be estimated by

$$V_{\mathrm{oc}} = \frac{1}{q}(E^{\mathrm{A}}_{\mathrm{LUMO}} - E^{\mathrm{D}}_{\mathrm{HOMO}}) - 0.3\,\mathrm{V} \ , \tag{2.7}$$

where q is the elementary charge, $E^{\mathrm{A}}_{\mathrm{LUMO}}$ is the LUMO energy level of the acceptor, and $E^{\mathrm{D}}_{\mathrm{HOMO}}$ the HOMO level of the donor. Here, the value 0.3 V is empirical and can also be higher or lower.

There are numerous studies for the factors that can negatively affect the V_{oc}. For an in–depth

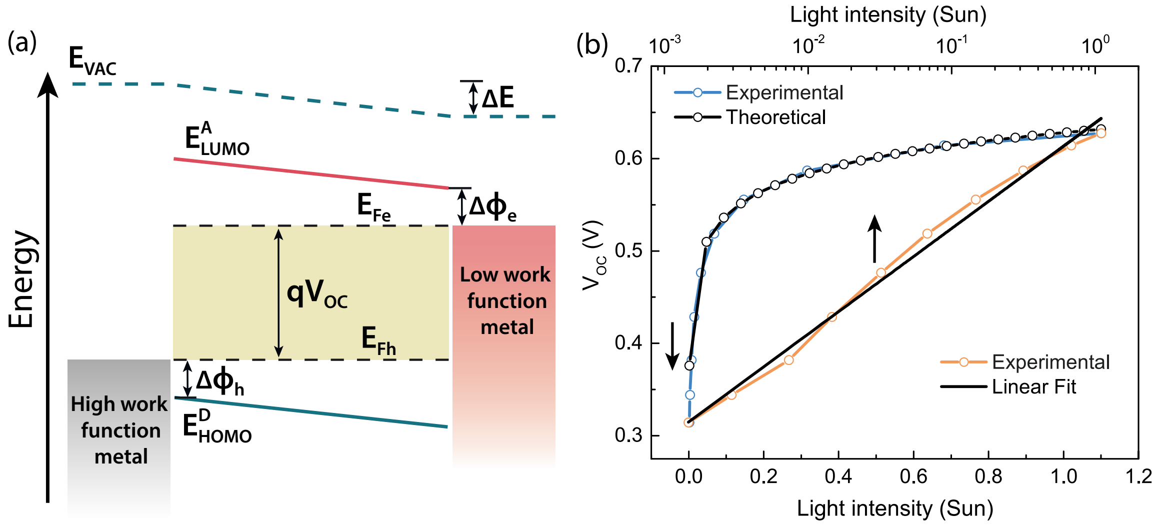

Figure 2.4: (a) Energy level diagram of an OSC under open–circuit condition. E_{Fe} and E_{Fh} are the quasi Fermi energy level of the electron and the hole. $\Delta\Phi_e$ and $\Delta\Phi_h$ are the electron and hole injection barriers, respectively. (b) Light intensity dependence of the open–circuit voltage V_{oc} shown as experimental results (blue) and theoretical values (black) from Eq. 2.9. The orange experimental values are shown as a semi–lofarithmic plot (top–x axes).

review of these factors, the reader is referred to a publication from Naveen K. Elumalai et al.[28]. Fig. 2.4(a) shows an energy level diagram of an OSC under open–circuit condition with the described energy levels.

A steady–state equation for V_{oc} is given by

$$V_{\mathrm{oc}} = \frac{m k_{\mathrm{B}} T}{q} \ln\left(\frac{j_{\mathrm{sc}}}{j_0}\right) + \frac{1}{q \cdot d}\left(E^{\mathrm{A}}_{\mathrm{LUMO}} - E^{\mathrm{D}}_{\mathrm{HOMO}}\right) . \tag{2.8}$$

Here, k_{B} is the Boltzmann constant, T the temperature, q the elementary charge, m the ideality factor of the diode, j_0 the dark saturation– , and j_{sc} is the short–circuit current–density, respectively, and $E^{\mathrm{A}}_{\mathrm{LUMO}}$ is the LUMO energy level of the acceptor and $E^{\mathrm{D}}_{\mathrm{HOMO}}$ the HOMO level of the donor. The prefactor d, with $d > 1$, is introduced to the take non-ideal effects into account [28]. It is noteworthy to mention that the ideality factor m, is not to be confused with the traditionally Shockley diode ideality factor n, because m is significantly different for dark and light measurements. Here, if $m = 1$, it denotes that the carrier recombination in the depletion zone can be neglected, and the diffusion current is dominant. The situation is vice versa if $m = 2$. For real OSCs, both carrier recombination and diffusion current arise, and m should be between one and two. On first approximation, a factor > 1 indicates that trap states are involved during charge carrier recombination [29].

From Eq. 2.8 and after assuming a linear dependency of the light intensity to the short–

circuit current j_{sc} [30], one can find an equation to estimate the light intensity dependence of the V_{oc}

$$V_{\mathrm{oc}} = \frac{mk_{\mathrm{B}}T}{q}\ln\left(\frac{I}{I_0}\right) + \frac{1}{q \cdot d}(E^{\mathrm{A}}_{\mathrm{LUMO}} - E^{\mathrm{D}}_{\mathrm{HOMO}}) \ , \tag{2.9}$$

where I is the light intensity and I_0 the light intensity at 1 Sun AM1.5 conditions. Fig. 2.4(b) shows the experimentally taken light intensity dependence of the V_{oc} in comparison to the theoretically calculated values from Eq. 2.9. Here, the value d and m were chosen in the way to fit the experimental data.

From the slope of a linear fit to the semi–logarithmic plots of the V_{oc} against the log–light intensity (cf. Fig. 2.4(b)), one can calculate the the ideality factor m_{voc} from V_{oc} with

$$m_{\mathrm{voc}} = \frac{q}{2.303 \cdot k_{\mathrm{B}}T} \cdot \frac{\partial V_{\mathrm{oc}}}{\partial \log I} \ . \tag{2.10}$$

The prefactor 2.303 is the conversion factor from the natural logarithm to the decadic logarithm.

2.5 Recombination lifetime

In a simple picture, the recombination lifetime of a charge carrier is the average time it takes before it recombines. Recombination processes of charge carriers within organic semiconductor blends often occur by transferring a carrier between two different phases. In such organic systems, the charge transfer process is often influenced by disorder, trap or midgap states, and a combination of different transfer states. Therefore, the charge carrier lifetime requires a careful definition, and for a more detailed description, the reader is referred to [31]. In this work, the determination of the recombination lifetime τ is based on small perturbation measurements, and therefore a suitable definition for τ is given below.

Assuming an electronic state within a semiconductor that is populated with a number of excess electrons, with volume density n, the decay of the population is determined by

$$\frac{dn}{dt} = -U_{\mathrm{n}}(n) \ , \tag{2.11}$$

where U_{n} corresponds to the recombination rate per unit volume. For a p–doped semiconductor, where the hole volume density p is basically the constant equilibrium density p_0, the simplest linear recombination model can be described by

$$U_{\mathrm{n}}(n) = Bp_0(n - n_0) \ . \tag{2.12}$$

Here, U_{n} only depends on the injected excess electron density $(n-n_0)$, with n_0 the equilibrium electron volume density. The prefactor B is a coefficient that depends on temperature and other factors. It is a common convention to denote $k_{\mathrm{rec}} = Bp_0$ as the recombination rate. The inverse of the recombination rate can be attributed to the electron lifetime τ_{n} with

$$\tau_{\mathrm{n}} = \frac{1}{k_{\mathrm{rec}}} \ . \tag{2.13}$$

If the recombination of the electron–hole pairs occurs before the exciton dissociation, it is called geminate recombination. Linking Eq. 2.11 with Eq. 2.12 and rewriting $(n - n_0)$ as Δn, the excess electron decay as a function of time has the form

$$\Delta n(t) = \Delta n(0) e^{(-t/\tau_{\mathrm{n}})} \ . \tag{2.14}$$

Now considering a small time dependent perturbation $\hat{n}(t)$ much smaller than the average value, caused by for example an alternating illumance, on the steady–state electron density $\bar{n}$, leads to the density dependence on time as

$$n(t) = \bar{n} + \hat{n}(t) \ . \tag{2.15}$$

The small perturbation electron density decays by the modified law of Eq. 2.11 with

$$\frac{d\hat{n}}{dt} = -\frac{dU_{\mathrm{n}}}{dn}\hat{n} \ . \tag{2.16}$$

In general we can define the recombination time τ as

$$\tau_{\mathrm{n}} = \left(\frac{\partial U_{\mathrm{n}}}{\partial n}\right)^{-1}_{\bar{\mathrm{n}}} = \frac{\hat{n}}{d\hat{n}/dt} \ . \tag{2.17}$$

This general defintion applies to measurements were the excess electrons are not extracted at the contacts. Such small perturbation measurements can be done with so–called intensity modulated photovoltage spectroscopy experiments, which will be discussed in chapter 2.7.4.

2.6 Solar cell parameters

Current–voltage characteristic

The current–voltage $I(V)$ characteristic of a solar cell describes the relationship between the electric current through the cell and the corresponding voltage. It is an excellent method to determine the key data such as open–circuit voltage V_{oc}, short–circuit current density j_{sc}, fill factor FF and power conversion efficiency PCE of a solar cell.

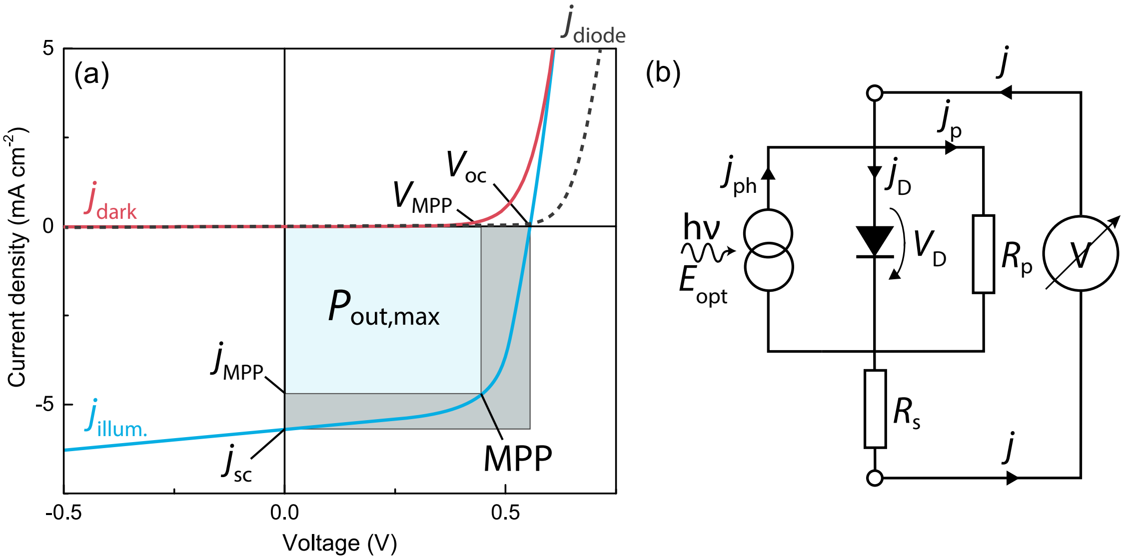

Figure 2.5: (a) Current density–voltage curve measured for an OSC. The curve shows the total current of the solar cell measured under dark conditions j_{dark} and with illumination $j_{\text{illum.}}$ The dashed gray line corresponds to a diode $j(V)$ curve. (b) Simplified equivalent circuit diagram of an ideal pn-solar cell with contacts.

For the measurement of the current–voltage characteristic a DC voltage U is applied to the contacts of the solar cell and the current I is measured. This is done for different voltages to determine the characteristic current-voltage curve. To provide comparable values for the current I, usually and within this work, $I(V)$ curves are given as current density j–voltage V plots and denoted by $j(V)$. Fig. 2.5(a) shows an experimentally measured $j(V)$ curve of an OSC. Details for the measured solar cell will not be discussed here. The figure shows the total current–density under illumination with an AM1.5 solar spectrum $j_{\text{illum.}}$ and the current–density under dark conditions j_{dark} compared to the $j(V)$ curve of a diode j_{diode}. The open–circuit voltage V_{oc} describes the voltage at zero current, whereas the short–circuit current j_{sc} describes the current at zero voltage. Both values can provide information about the condition of a solar cell. A very good comparative value offers the fill factor FF. The FF is most commonly determined from the $j(V)$ curve, and it is a measure of the 'squareness' of the curve. It is defined as the maximum power, which is given by the product of $(j_{\text{MPP}} \cdot V_{\text{MPP}})$ with MPP as the maximum power point, divided by the product of $(j_{\text{sc}} \cdot V_{\text{oc}})$, i.e.:

$$\text{FF} = \frac{j_{\text{MPP}} \cdot V_{\text{MPP}}}{j_{\text{sc}} \cdot V_{\text{oc}}} \; . \tag{2.18}$$

The most important parameter of a solar cell is its power conversion efficiency PCE. It can be calculated with

$$\text{PCE} = \frac{j_{\text{MPP}} \cdot V_{\text{MPP}}}{E_{\text{opt}}} = \frac{j_{\text{sc}} \cdot V_{\text{oc}} \cdot \text{FF}}{E_{\text{opt}}} \; . \tag{2.19}$$

The PCE is defined as the ratio of the energy output from the solar cell to the energy input from the light source [32]. In Fig. 2.5(a) it can be seen that the j_{dark} curve progression of a solar cell is similar to that of a diode. Therefore, the easiest current–voltage curve can be derived from the semiconductor–equations of a diode. A simplified equivalent circuit diagram of a pn–semiconductor solar cell with contacts is shown in Fig. 2.5(b). In the simplest representation, the solar cell consists of a power source and an ideal diode. The power source generates the photocurrent j_{ph}. R_{p} denotes the parallel resistance or sometimes also called shunt resistance of the cell and R_{s} the series resistance, respectively. The current j_{D} through an illuminated solar cell can in the simplest way be expressed with

$$j_{\text{D}} = j_0 \cdot [\exp\left(\frac{q \cdot (V - j \cdot R_{\text{s}})}{n \cdot k_{\text{B}} \cdot T}\right) - 1] + \frac{V - j \cdot R_{\text{s}}}{R_{\text{p}}} - j_{\text{ph}} \ , \tag{2.20}$$

where q is the elementary charge, k_{B} the Boltzmann constant, T the temperature and n the ideality–factor of the diode. The ideality factor gives a measure of how close the diode follows the ideal diode equation and is typically in the range between 1 and 2 [33]. The first term of the equation corresponds to the current through a diode and is therefore referred to as the diode–term, the second term describes the current through the parallel resistance R_{p} and j_{ph} denotes the produced photocurrent under illumination. The series resistance R_{s} considers the losses in the conductors (contacts) and solar modules also the losses at the connections between the individual cells. Considerable R_{s} influence the short-circuit current j_{sc} and the resistance should, therefore, be as low as possible. The parallel resistance is mainly due to defects which cause a forward leakage path of minority carriers [34]. For good solar cells, it is in the order of $R_{\text{p}} > 1k\Omega cm^2$. R_{p} predominantly influences the open circuit voltage V_{oc}. A detailed influence of the resistors R_{p} and R_{s} on the $j(V)$ characteristic is given in the following chapter.

Influence of the series resistance on the $j(V)$ characteristic

Resistive effects in solar cells reduce the efficiency of solar cells due to power dissipation in the resistors [35]. Such resistors cannot be removed from the solar cell compound and therefore are called parasitic resistors. The effect of such parasitic resistors can immediately be seen in the $j(V)$ curve. As a consequence, the key impact of a parasitic resistance is the reduction of the fill factor. Graphically, the resistances can be estimated from the slope of the $j(V)$ characteristic at suitable sections where the influence of the respective other resistor is not high. R_{s} is typically estimated at $V > V_{\text{oc}}$ in the forward bias direction and R_{p} at very small voltages determined as a tangent at $V = 0\,\text{V}$. The value for the resistance is highly dependent on the area of the solar cell, therefore a common unit for resistances is Ωcm^2 or often denoted as $(\Omega\square)$. The area normalization is easily obtained by replacing the

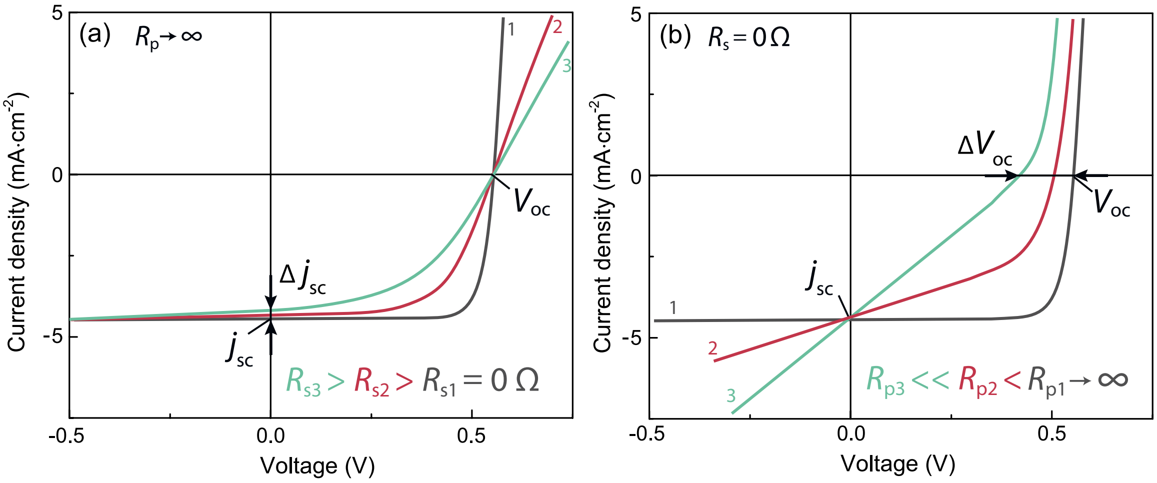

Figure 2.6: (a) Current density–voltage curves for different series resistors R_s. (b) $j(V)$ curves for different parallel resistors R_p.

current with the current density in Ohm's law like

$$R'(\Omega cm^2) = \frac{V}{j} \ . \tag{2.21}$$

The effect of the series resistance R_s is shown in Fig. 2.6(a). The graph shows three different $j(V)$ curves for different series resistors. The V_{oc} of the cell is unaffected by the R_s, whereas for very large resistances the j_{sc} is lowered. However, the series resistance strongly affects the curve near open–circuit voltage point. Therefore, a straightforward method to estimate the series resistance of the solar cell is to find the slope of the $j(V)$ curve at V_{oc}.

Power losses in solar cells are often due to manufacturing defects and the consequent presence of a parallel resistance. A low parallel resistance causes an alternate current path for the generated photocurrent and therefore reduces the voltage of the solar cell. The influence is particularly severe at low light intensities since also the photocurrent gets smaller. Fig. 2.6(b) shows three $j(V)$ curves for different parallel resistors. The $j(V)$ characteristic is strongly altered as the resistance is decreased. Low parallel resistance can decrease the V_{oc}. The value for the resistance can be estimated in a similar manner to that used to estimate the series resistance, by finding the slope of the $j(V)$ curve near the j_{sc}.

For real optimized OSCs the influence of R_s and R_p might not be that obvious as shown in Fig. 2.6. Hence, it is common to represent $j(V)$ curves in a semilogarithmic plot. A schematic $j(V)$ curve is shown in Fig. 2.7. The influence of the parasitic resistances are most visible in the $j(V)$ curves measured under dark conditions. The interesting regions of R_s and R_p are indicated with dashed ellipses. In addition, the region most assigned by the exponential term of the diode current equation (Eq. 2.20) is indicated. To point out

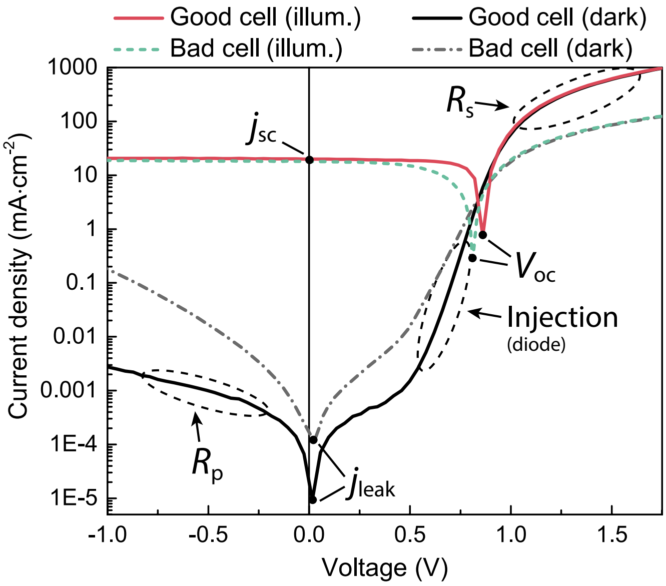

Figure 2.7: Schematic semilogarithmic representation of the $j(V)$ curve under illumination and dark conditions. The regions affected by R_s, R_p, and the diode related injection, are marked with dashed ellipses.

the effect of a high R_s and a low R_p on the $j(V)$ curve, the curve of a bad example cell is shown with the dashed green line (under illumination) and the dash–dotted grey line (dark conditions). The slope of the curve in the R_s–affected region is lower compared to the slope of a good cell (solid red line). In the negative bias region the slope of the curve is higher than for the good cell. The solar cell device parameters such as V_oc, j_sc, and the dark leakage current–density j_leak are indicated in the plot. The dark leakage current in an OSC is the undesired current thru the R_p injected from the electrodes under dark conditions [36]. The direction of the leakage current is opposite to the photocurrent and, therefore, reduces the j_sc of the device.

External quantum efficiency

The external quantum efficiency (EQE) relates the photons incident on the solar cell to the number of charge carriers collected by the cell [37]. The EQE is wavelength dependent and can be measured by illuminating the solar cell with a monochromatic light source with particular wavelength λ and measuring the photocurrent I_ph flowing through the cell. It can be expressed by

$$\mathrm{EQE}(\lambda) = \frac{I_\mathrm{ph}(\lambda)}{q\psi_{\mathrm{ph},\lambda}} \,, \tag{2.22}$$

here $\psi_{\mathrm{ph},\lambda}$ is the spectral photon flow incident on the solar cell and q is the elementary charge. Usually $\psi_{\mathrm{ph},\lambda}$ is measured with a reference photodiode under the same light conditions.

Fig. 2.8 shows an example of an experimentally taken EQE measurement as a function of the wavelength λ in (a) and the photon–energy (eV) in (b).

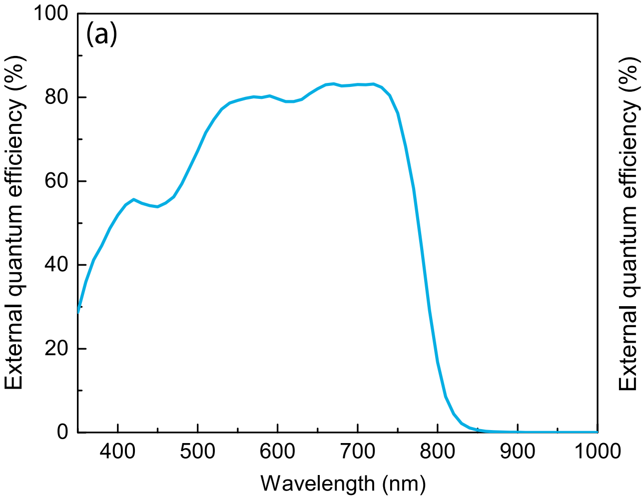

Figure 2.8: The external quantum efficiency EQE of an OSC as a function of (a) wavelength and (b) photon–energy.

Such EQE spectra are measured using a so–called spectral response setup [37]. In such a setup, usually a wavelength selective light source is used to illuminate the solar cell. A commonly used light source is a xenon discharge lamp with a very broad light spectrum that provides all the important wavelengths of the sunspectrum (cf. Fig. 2.1(a)). Filters and monochromators are used to select a very narrow wavelength band of photon energies that then can be incident on the solar cell. While the electric current through the cell can easily be measured with a suitable Ampere meter, the incident photon flow can only be determined indirectly. Therefore, the spectral photocurrent $I_{\mathrm{ph}}^{\mathrm{ref}}(\lambda)$ of a calibrated reference photodetector (usually a Si–photodiode), with known spectral $\mathrm{EQE}^{\mathrm{ref}}(\lambda)$ is measured initially. One can find

$$\psi_{\mathrm{ph},\lambda} = \frac{I_{\mathrm{ph}}^{\mathrm{ref}}(\lambda)}{q\mathrm{EQE}^{ref}(\lambda)} \ , \tag{2.23}$$

and together with Eq. 2.22 this leads to

$$\mathrm{EQE}(\lambda) = \mathrm{EQE}^{\mathrm{ref}}(\lambda)\frac{I_{\mathrm{ph}}(\lambda)}{I_{\mathrm{ph}}^{\mathrm{ref}}(\lambda)} \ , \tag{2.24}$$

Therefore, the EQE can be determined by performing two current measurements. A detailed setup will be explained in the experimental section.

Another advantage of a spectral response setup is that the short-circuit current j_{sc} can be calculated from the EQE measurement. Normally, the accuracy of a $j(V)$ curve measurement depends strongly on the spectral shape of the used light source. Furthermore, the solar cell area is often not determined accurately enough. The j_{sc} is calculated by integrating the product of the EQE(λ) with the known spectral photon flux $\Phi_{\text{ph},\lambda}^{\text{AM1.5}}$ (for AM1.5 conditions) across the relevant wavelength range

$$j_{\text{sc}} = -q \int_{\lambda_1}^{\lambda_2} \text{EQE}(\lambda)\Phi_{\text{ph},\lambda}^{\text{AM1.5}} d\lambda \; . \tag{2.25}$$

2.7 Impedance spectroscopy

Impedance spectroscopy is a powerful technique to investigate the electrical properties of a large field of devices. The following chapter will give a brief introduction to electrical impedance spectroscopy and its related intensity modulated spectroscopy.

2.7.1 Electrical impedance

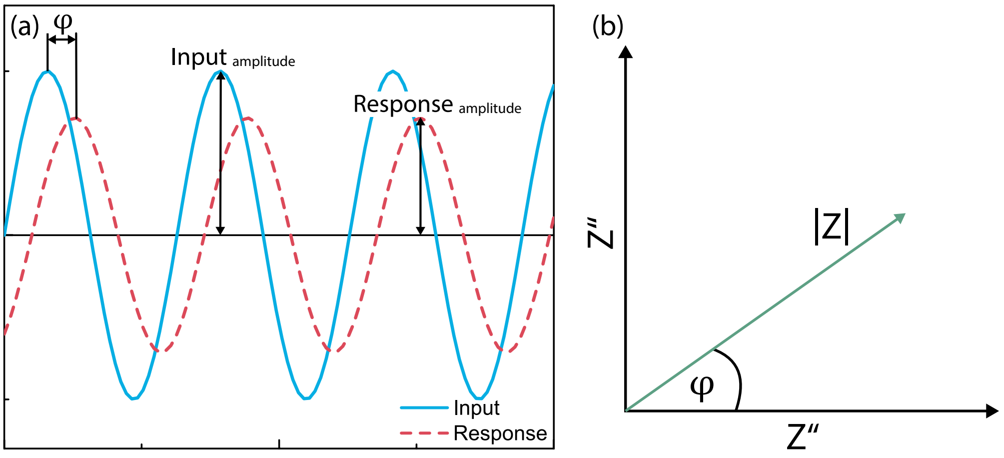

Figure 2.9: (a) Illustration of input and response signals showing a change in amplitude and phase shift, redrawn from [38]. (b) Nyquist plot of an impedance transfer function.

The electrical impedance is the alternating current (AC) resistivity of an electrical device. Usually the impedance is denoted with Z and relates the current I and the voltage U by the AC form of Ohm's law i.e. $Z = V/I$. Fig. 2.9(a) shows an illustration of the input and the response signal of an electric device. The sinusoidal input voltage signal can be written as

$$V(t) = V_0 \cos(\omega t + \varphi_U) \; , \tag{2.26}$$

where V_0 is the input amplitude, φ_U the phase and ω is the angular frequency given by $\omega = 2\pi f$, where f is the frequency. The measured response of the electric device is the induced current I, which can be written as

$$I(t) = I_0 \cos(\omega t + \varphi_I) \ . \tag{2.27}$$

Here, I_0 denotes the response amplitude and φ the phase shift of the output signal. Then, the complex impedance can be given by

$$Z(j\omega) = \frac{V(j\omega)}{I(j\omega)} = \frac{V_0}{I_0} \cdot e^{-j\varphi} = |Z| \cdot e^{j \cdot \varphi} = \mathrm{Re}(Z) + j \cdot \mathrm{Im}(Z) \ . \tag{2.28}$$

The identity $\varphi = \varphi_U - \varphi_I$ is the phase angle between $U(t)$ and $I(t)$. From Eq. 2.28 one can calculate the real and imaginary part of the Impedance Z and represent it in a so-called Nyquist plot. An example is given in Fig. 2.9(b).

2.7.2 Impedance response of simple circuit elements

The impedance response of simple electrical components such as resistor and capacitor is well defined for AC signals [38]. An ohmic resistor R emerges no phase shift when it is operated with an AC voltage, thus voltage and current are in phase ($\varphi = 0$). The impedance Z is therefore

$$Z_R = \frac{V_0}{I_0} = R \tag{2.29}$$

The impedance thus has no imaginary component. The value of the impedance is just the resistance. The corresponding Nyquist plot is shown in Fig. 2.10(a).

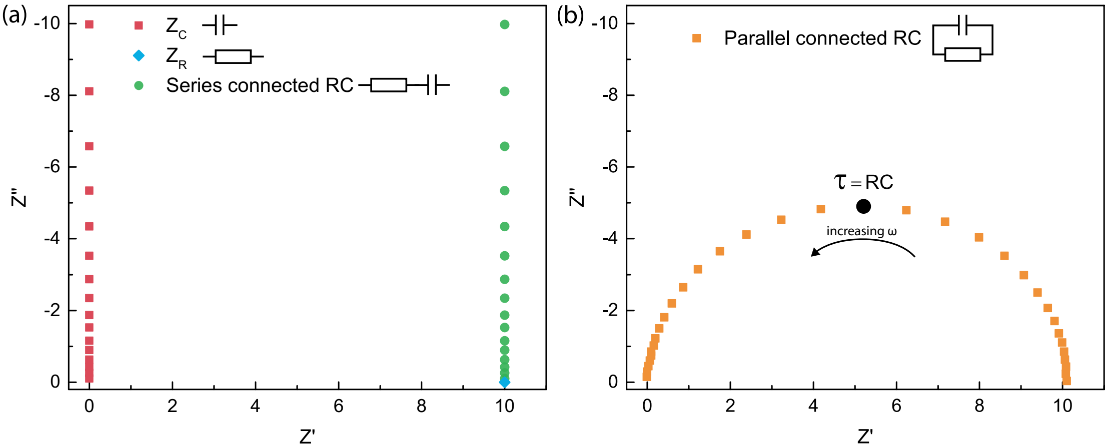

Figure 2.10: (a) Nyquist plot of a capacitor and a resistor and the series connection of them. (b) Nyquist plot of parallel connected RC.

For a capacitor C, connected to an AC signal, the current–voltage relationship is given by

$$I(t) = C \cdot V_0 \cdot j\omega e^{j\omega t} \tag{2.30}$$

With Ohm's law the impedance can be given by

$$Z_C = \frac{V}{I} = \frac{1}{j\omega C} \tag{2.31}$$

Here one can see that the impedance of a capacitor has no real component. Thus the current leads the voltage by 90°. With increasing frequency the impedance decreases. In the Nyquist plot this is represented by a vertical line at $Z' = 0$ (cf. Fig. 2.10(a)).

2.7.3 Impedance response of simple circuits

The impedance for combinations of electrical devices such as resistor R and capacitor C can also be calculated. In series connection the impedance is given by

$$Z_{tot} = \sum_i Z_i = Z_R + Z_C = R + \frac{1}{j\omega C} \tag{2.32}$$

In the Nyquist plot this is represented by a vertical line at $Z' = R$ (cf. Fig. 2.10(a)). In contrast, the parallel connection is the summation of the electric conductance (reciprocal value) of each component. The impedance response for a parallel connection is given by

$$\frac{1}{Z_{tot}} = \sum_i \frac{1}{Z_i} = \frac{1}{Z_R} + \frac{1}{Z_C}\ , \tag{2.33}$$

The total impedance written in terms of R and C

$$Z_{tot} = \frac{1}{\frac{1}{Z_R} + \frac{1}{Z_C}} = R\frac{(1 - j\omega RC)}{(1 + \omega^2 R^2 C^2)} \tag{2.34}$$

The notation $Z_{tot} = \mathrm{Re}(Z_{tot}) + j\,\mathrm{Im}(Z_{tot})$ for the imaginary and real parts results in:

$$\mathrm{Re}(Z_{tot}) = Z'(\omega) = \frac{R}{(1 + \omega^2 R^2 C^2)}, \qquad \mathrm{Im}(Z_{tot}) = Z''(\omega) = -\frac{\omega R^2 C}{(1 + \omega^2 R^2 C^2)} \tag{2.35}$$

Fig. 2.10(b) shows the plot of the impedance for a parallel connection of a R and C element. For a high frequency ($\omega \to \infty$) the impedance is zero. The capacitor is simply to slow to charge/discharge at such high frequencies and therefore behaves as a short-circuit. At very low frequency ($\omega \to 0$), the impedance simplifies to R. No current flows through the capacitor, once it is fully charged, so the current flows through the resistor. In the Nyquist plot this is represented by a semicircle. The maximum point of the semicircle is called the

$RC = \tau$ time constant. The reciprocal value $\tau^{-1} = \omega = 2\pi f_\mathrm{p}$ is known as the characteristic frequency of the system. f_p corresponds to the peak frequency of the maximum point of the semicircle.

A Bode plot is used to show the frequency– dependence of dielectric circuit components.

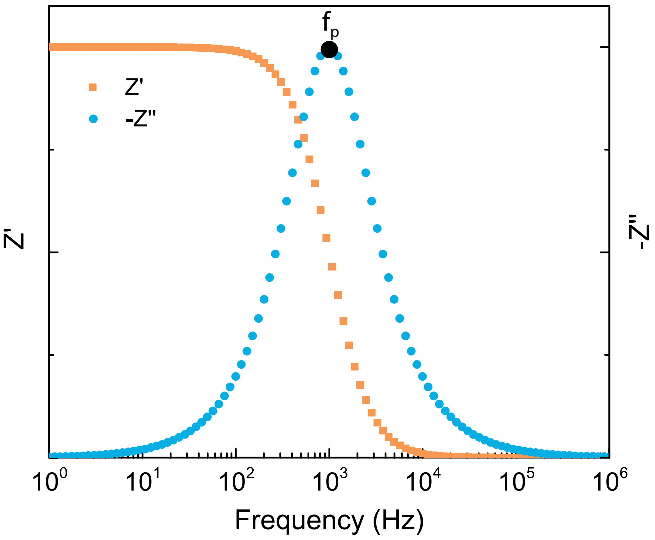

Figure 2.11: Bode plot of the impedance spectrum of a RC parallel connection for the real and imaginary part of the impedance. The peak frequency $f_\mathrm{p} = \omega/2\pi$ is indicated.

Usually, the real part Z' as a function of frequency and the imaginary part Z'' versus frequency, of Eq. 2.7.3, for the RC parallel circuit, are represented in a graph like Fig. 2.11. The peak frequency $f_\mathrm{p} = \omega/2\pi = \tau^{-1}$ is indicated in the graph. The RC circuit is a basic tool for modeling the impedance response of physical samples.

2.7.4 Intensity modulated impedance spectroscopy of solar cells

In contrast to the electric impedance spectroscopy (EIS) it is also possible to use other stimuli signals than an alternating voltage signal. Intensity modulated impedance spectroscopy uses modulated light as the perturbation signal. A solar cell is illuminated with a specific DC light intensity, which is superimposed with an alternating AC light intensity. This will produce a similar effect to electrical impedance spectroscopy. With this technique the key processes of a solar cell

- charge transport
- charge storage
- electron-hole recombination

- interfacial charge transfer

can be reflected in the impedance response.

Intensity modulated photovoltage and photocurrent methods

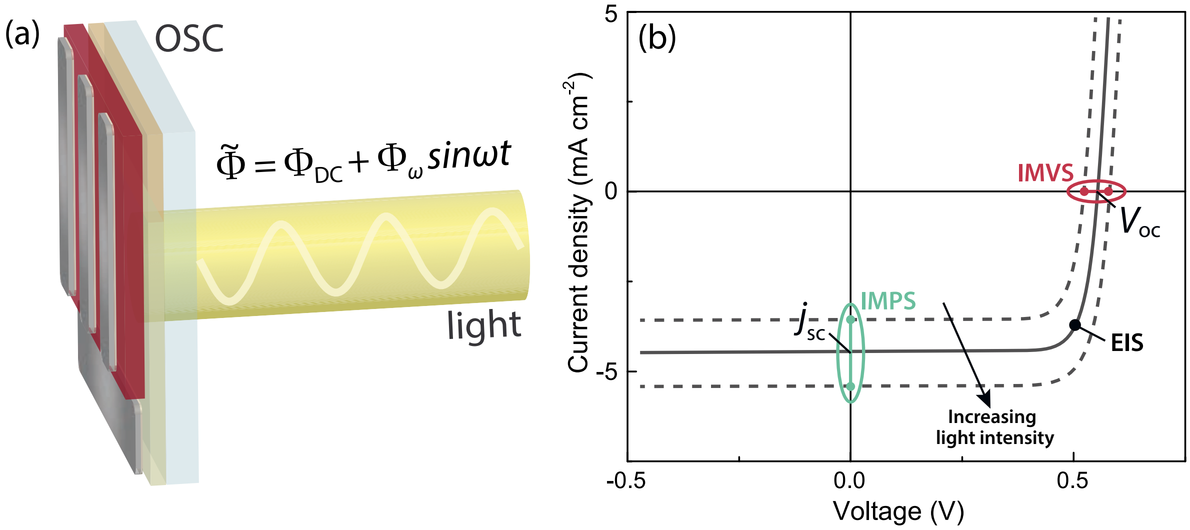

Figure 2.12: (a) Illustration of the intensity modulated spectroscopy method. (b) Effect of IMVS and IMPS shown on $j(V)$ curve.

Intensity modulated photovoltage spectroscopy (IMVS), and intensity modulated photocurrent spectroscopy (IMPS) are two closely related techniques in which the light input flux Φ_{DC} of a light source is overlapped by an alternating light Φ_{ω} (usually a few % < 10% of the DC light flux) resulting in a total input photon flux function $\tilde{\Phi} = \Phi_{\mathrm{DC}} + \Phi_{\omega}\sin(\omega t)$. The response (current or voltage) of the cell is then measured as a function of the modulation frequency ω. Fig. 2.12(a) shows a schematic representation of such an IMVS or IMPS measurement. In IMVS, the solar cell is normally held at open–circuit. As no charge is extracted, it mainly gives information about the charge recombination within the cell. In Fig. 2.12(b) one can see the effect of the alternating light intensity I_{ω} (compare light intensity dependence of the open–circuit voltage in chapter 2.4) on the $j(V)$ curve of the examined cell. IMPS measurements are normally held at short–circuit and give information about the charge carrier transport. The resulting effect of the IMPS measurement on the $j(V)$ curve is shown in Fig. 2.12(b). For both techniques the relationship between the modulated input photon flux function $\tilde{\Phi}$ and the modulated current or voltage response is defined by the frequency–dependent transfer function H:

$$H_{\mathrm{IMVS}}(\omega) = \frac{\tilde{U}_{\mathrm{ph}}(\omega)}{\eta q \tilde{\Phi}} \qquad H_{\mathrm{IMPS}}(\omega) = \frac{\tilde{I}_{\mathrm{ph}}(\omega)}{\eta q \tilde{\Phi}} \tag{2.36}$$

Here the $\sim$ symbol indicates the AC components of the variables, η corresponds to the quantum efficiency for charge generation, and q is the elementary charge. From H_{IMVS}, one can see that the transfer function has units of Ωcm^2, which can be related to the impedance. In contrast, H_{IMPS} is dimensionless.

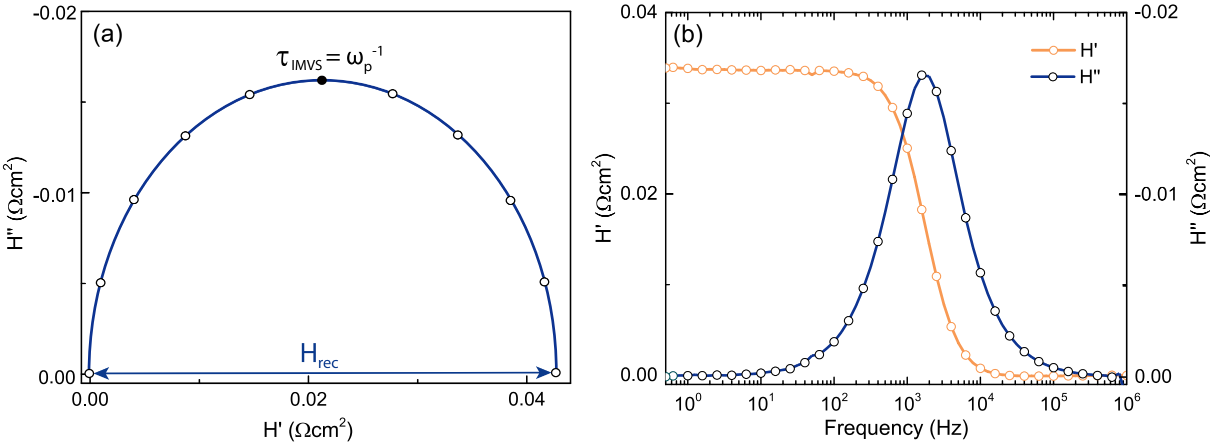

Figure 2.13: (a) Example for an IMVS response and the extraction of the time constant τ at the maximum point of the semicircle. The diameter of the semicircle can be linked to the recombination impedance H_{rec}. (b) Bode plot of the real H' and imaginary H'' response of the transfer function H.

Fig. 2.13(a,b) shows the typical transfer function H response from an IMVS measurement. The arc can be attributed to the recombination processes in the photoactive material [39], to the capacitance, resistance, and effective electron lifetime. The spectrum obtained from IMVS (cf. Fig. 2.13(a)) is similar to the measured spectrum from electrical impedance measurements (cf. Fig. 2.10(b)). The time constant τ is related to the effective electron lifetime in OSCs. The diameter of the semicircle can be connected to a so–called charge recombination resistance R_{rec} [38]. As the response of the IMVS only gives a transfer function H, this will further be called the recombination impedance H_{rec}.

The line–shape of the real H' and imaginary part H'' of the transfer function H (Eq. 2.36) shown in Fig. 2.13(b), closely resembles the line shapes of the real and imaginary part of the impedance spectrum of parallel–connected RC circuit components with a single time constant $\tau = R \cdot C$, shown in Fig. 2.11. Therefore, the simplified equivalent circuit diagram of an ideal OSC shown in Fig. 2.5 (b) can be expanded with a capacitive circuit element. Fig. 2.14(a) shows the equivalent circuit diagram of Fig. 2.5 (b) for a planar solar cell, with a capacitive circuit element C_{tot} (marked in red color) in parallel connection to the recombination resistance R_{rec}. C_{tot} is the total capacitance of the device. It is the sum of the geometric capacitance formed by the charge stored in the contacts, and the chemical capacitance emerged by the photogenerated charge in the bulk–heterojunction of the OSC

[38]. The multiplication of R_rec and C_tot gives the effective electron lifetime τ in OSCs.

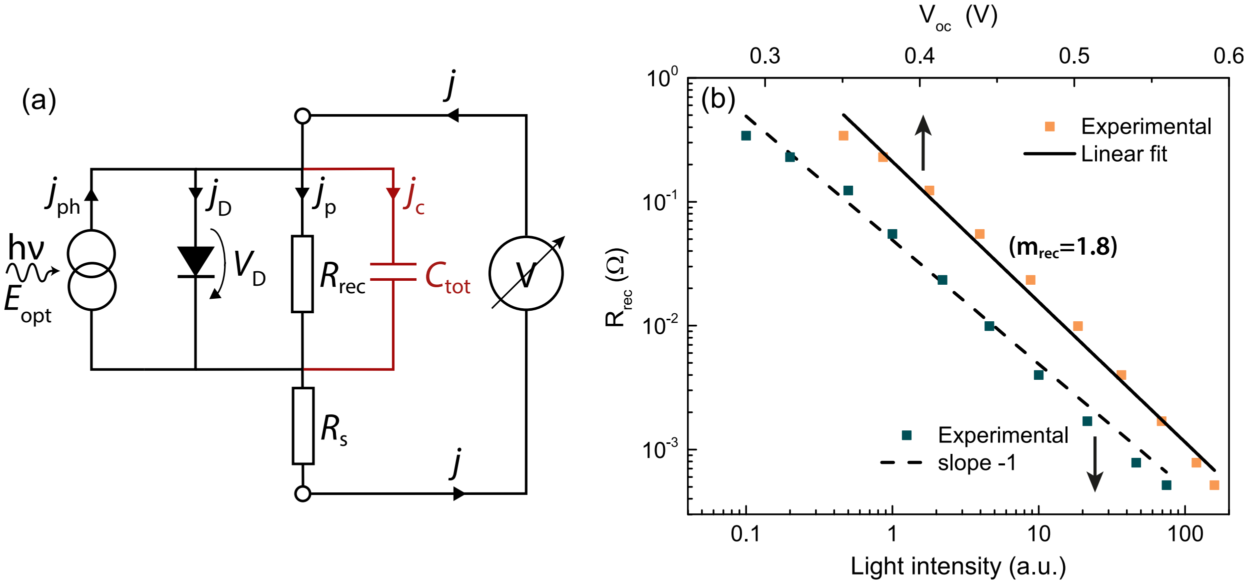

Figure 2.14: (a) Simplified equivalent circuit diagram of an ideal OSC (cf.Fig. 2.5(b)) expanded with a capacitive circuit element C_tot shown in red. (b) Linear dependence of the recombination resistance R_rec to the light intensity. The dashed–line with a slope $= -1$ corresponds to a linear dependence. The experimental values in orange correspond to $\log R_\text{rec}$ against V_oc (top–x axes).

Germa Garcià –Belmonte et al. showed that a linear dependence of R_rec to the light intensity (as shown by the slope of -1 in a log–log plot Fig. 2.14(b)), indicates that R_rec is indeed a recombination resistance [40]. Furthermore, using the logarithmic dependence of the V_oc to the light intensity (see Eq. 2.9), they find that R_rec is related to the recombination current density j_rec, V_oc and the device area A via

$$R_\text{rec} = \frac{1}{A}\left(\frac{dj_\text{rec}}{dV_\text{oc}}\right)^{-1} . \tag{2.37}$$

From Eq. 2.9 and Eq. 2.37 the relationship

$$m = \frac{q}{2.303 \cdot k_\text{B}T} \cdot \frac{\partial V_\text{oc}}{\partial \log R_\text{rec}} , \tag{2.38}$$

for the ideality–factor m is derived. The dimensionless number 2.303 is the conversion factor from the natural logarithm to the decadic logarithm. The fraction $\partial V_\text{oc}/\partial \log R_\text{rec}$ is evaluated by a linear fit of the data in the semi–logarithmic plot (cf. Fig. 2.14(b)).

2.8 Magnetic field effects in organic semiconducting materials

Introduction

Early studies in the 1960 and 1970s showed that weak magnetic fields can effectively change the optical and electrical properties of nonmagnetic organic semiconductors [41]. These studies opened the door for the field of organic spintronics and the associated application. The interesting magnetic field effects (MFE) for this thesis are the effects on the photoluminescence properties. Up to now, there are several studies on the photoluminescence MFE in organic semiconductors [42, 43]. Photoluminescent MFEs can reveal the origin of the intersystem crossing (ISC) between polaron pairs (pp) and the formation of pp, triplet–triplet annihilation (TTA), as well as the charge transfer state between a donor and an acceptor material, and many more. In this thesis, MFE experiments were performed to investigate charge transfer mechanisms in fullerene– and fullerene–free OSCs. A.S. Dhoot et al. showed that triplet excitons can interact with charge carriers in organic material [44]. Therefore, investigating triplet exciton evolution can give insights into the charge transport mechanisms in organic semiconductors. In principle, singlet and triplet states can influence the photocurrent generation in OSCs, it is, thererfore, interesting to investigate the origin of these excited states. Experiments were studied under low–temperature conditions (5 K). In this thermodynamic region, most molecular motion ceases, and the entropy change is zero for any adiabatic process. Therefore, thermally activated states can be neglected and do not influence the photoluminescence. In order to explain the MFEs on organic materials, several theoretical approaches exist to explain the ongoing mechanisms. These mechanisms deal with spin–carrying particles, which will be further explained in the next chapters.

The role of the electron spin

So far, the excited state picture for the electrons and holes was sufficient for the description of the working principle of OSCs (see chapter 2.3). For the description of magnetic field effects in organic semiconductors, it is required to consider the spin of the charge carriers. In a quantum mechanical picture, the electron spin is an intrinsic form of angular momentum. The total spin S of an electronic state is given by the total spin of all unpaired electrons in all orbitals [13]. A delocalized electron is exposed to many randomly orientated nuclear magnetic moments, from e.g., hydrogen or nitrogen atoms. In a semi–classical way, the sum of all these magnetic moments is often referred to as an effective magnetic field called the hyperfine field. The spectrum of this field is described by a Gaussian distribution, where the standard deviation can be referred to the field strength. The hyperfine field strength is usually in the order of several millitesla in organic semiconductors [45].

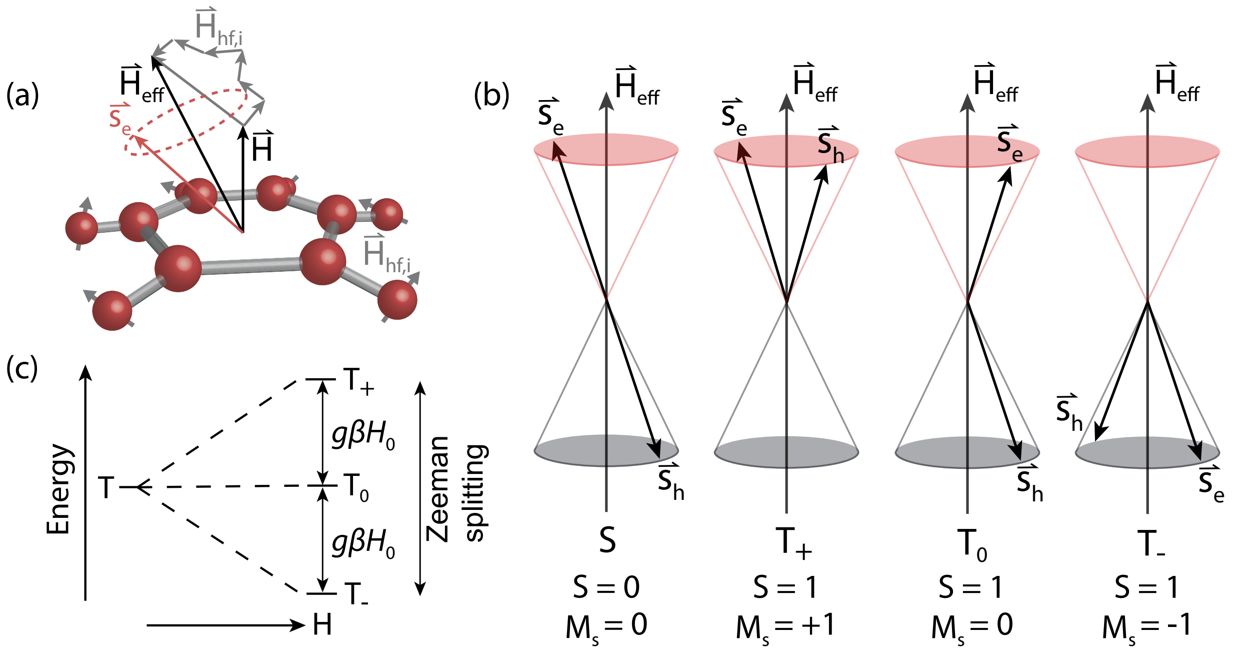

Figure 2.15: Semi–classical picture of the spin precission around an effective magnetic field H_{eff}. (b) Representation of singlet (S)– and triplet (T) states in a vector diagram of the two–particle system. The two spins, precess around an external magnetic field in z–direction. (c) Energy level diagram. The triplet energy levels are split into three sublevels in an external magnetic field.

Fig. 2.15(a) shows a schematic representation of an electron spin $\vec{s_e}$ precessing around an effective magnetic field $\vec{H_{\text{eff}}}$. They precess around the field with the Larmor frequency

$$\omega = g\beta\hbar^{-1}H_{\text{eff}} \ , \tag{2.39}$$

where g is the electron Landé's factor, β corresponds to the Bohr–magneton, and $\hbar$ is the reduced Planck constant. An unpaired hole in the ground state and an electron in the excited state form a so–called two–particle system and are referred to as a radical pair RP. The quantum mechanical description of a two–particle system in an external– or an internal nuclear–magnetic field (e.g., hyperfine–field) in the z–direction (vertical), leads to four possible eigenstates of the spin dependent wavefunction Ψ_{spin}.

$$\begin{aligned}
\Psi_{\text{spin,S}} &= \frac{1}{\sqrt{2}}(\alpha_1\beta_2 - \beta_1\alpha_2), && S = 0 \text{ and } M_{\text{S}} = 0\\
\Psi_{\text{spin,T+}} &= \alpha_1\alpha_2, && S = 1 \text{ and } M_{\text{S}} = 1\\
\Psi_{\text{spin,T0}} &= \frac{1}{\sqrt{2}}(\alpha_1\beta_2 + \beta_1\alpha_2), && S = 1 \text{ and } M_{\text{S}} = 0\\
\Psi_{\text{spin,T-}} &= \beta_1\beta_2, && S = 1 \text{ and } M_{\text{S}} = -1
\end{aligned} \tag{2.40}$$

Here, α and β correspond to the one–particle spin wavefunction, with eigenvalues $s = \pm 1/2$, $m_{\mathrm{s}} = \pm 1/2$. Index 1 and 2 correspond to electron one and two, respectively. A so–called singlet state exists when the RP has an antiparallel spin orientation, and so the total spin adds up to zero $S = 0$, with an eigenvalue $M_{\mathrm{s}} = 0$. The quantum number M_{s} corresponds to the sum of the $z-$components of the two spins. Three triplet states with parallel spin orientation are possible, where the total spin adds up to $S = 1$, with eigenvalues $M_{\mathrm{s}} = 1,\ 0, -1$.

The four eigenstates of the spin–wavefunction are schematically depicted in a vector diagram in Fig. 2.15(b). The two spins, indicated by vector $\vec{s_{\mathrm{e}}}$ and $\vec{s_{\mathrm{h}}}$ for the electron and the hole, respectively, precess around the vector sum $\vec{H_{\mathrm{eff}}}$ of all nuclear hyperfine fields and the external magnetic field. For an antiparallel singlet state configuration, the spins precess 180° out of phase, which leads to a vector sum that is always zero. For triple states, the spins precess in phase, and the vector sum is non–zero. Fig. 2.15(c) shows the triplet eigenstates of the two–particle system (Eq. 2.40) in an energy level diagram. In the presence of a magnetic field, the triplet RP states are split by the Zeeman interaction into the three sublevels T_+, T_0 and $T_{\text{-}}$, respectively. The energy difference of the sublevels equals $g\beta H_{\mathrm{eff}}$, where g is the electron $g-$value, β the Bohr–magneton, and H_{eff} the magnetic field strength [46].

Photoluminescence

The photoluminescence of a molecule always presupposes the formation of RPs. Processes involved during the formation of RPs are often represented in so–called Jablonski diagrams (cf. Fig. 2.16(a))[47]. The energy levels of a molecule are depicted as horizontal lines and energetic transitions between them are shown as vertical arrows. An unexcited luminescent molecule is considered to be in the S_0 singlet ground state. The absorption of a photon with sufficient energy can promote an electron from the S_0 into the first excited vibronic state S_1, or in an even higher state of an organic semiconductor. Once an excited state is populated, the electron quickly relaxes to the vibrational ground state of the level S_1. This process happens non-radiatively within $\sim 100\,\mathrm{fs}$ or less and is called internal conversion (IC). The energy difference between the higher vibronic level and the vibronic ground state is released as heat.

The electron in the excited state S_1 is paired with another electron of opposite spin in the ground state (singlet configuration). Therefore, decays into the ground state S_0 are spin allowed and can happen radiatively under emission of a photon. This transition process has a lifetime in the nanosecond regime and is called fluorescence. Due to the internal conversion, the emitted photons are of lower energy than the absorbed ones, leading to a spectral

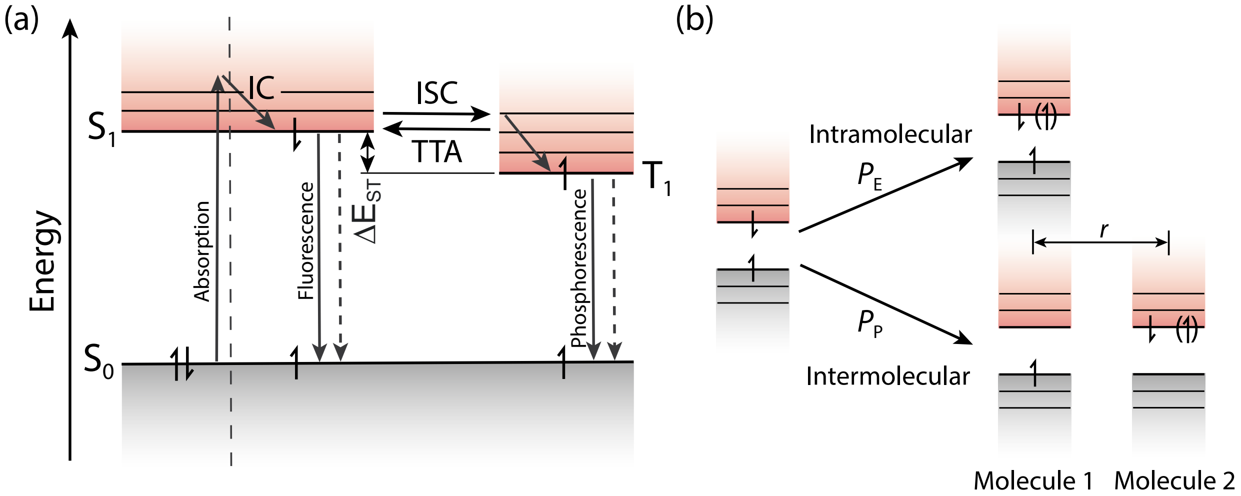

Figure 2.16: Representation of singlet (S)– and triplet (T) states. (a) S and T states in a Jablonski diagram. The horizontal line S_0 correspond to the electronic ground state and S_1, and T_0 are the first single and triplet excited state, respectively. The vertical lines denote radiative transitions between to levels. Dashed lines correspond to non radiative transitions. (b) Schematic representation of intramolecular and intermolecular excited states. The electron with upward–spin at molecule 2 denotes singlet configuration. The electron in the parentheses with downward-spin, corresponds to triplet configuration.

shift of the fluorescence towards longer wavelengths by tens of nanometers compared to the absorption. This is called a Stokes shift. However, an electron in the excited S_1 state can also perform a spin flip and transit to a vibronic triplet state of equal energy in a process called intersystem crossing (ISC) or spin–mixing. The spin conversion is possible due to the quantum mechanical coupling between spin and orbital angular momentum and is more probable for heavy atomic systems. The hyperfine interactions due to the energy of nuclear magnetic dipole moments also affect the spin conversion in organic semiconductors. From the energetically higher vibronic triplet state, the electron rapidly relaxes into the vibronic ground state of the triplet state T_1 and is paired with another electron of same spin in the singlet ground state S_0 (triplet configuration). Triplet-singlet transitions are spin-forbidden, and therefore the lifetime of phosphorescence (the radiative decay from the triplet T_1 to the singlet S_0 state) is usually much higher than the lifetime of fluorescence and can reach ms values. Since the T_1 state is usually energetically even lower than the S1 state, the Stokes shift of phosphorescence is more pronounced and is often in the range of 200 nm. The quantum–statistics of singlet and triplet spin–states yields a 1 : 3 recombination ratio for organic materials [43].

The dipole–dipole interaction between two triplet–excitons with same magnetic quantum number m_s, can lead to the conversion into one singlet–exciton in a process called triplet–triplet–annihilation (TTA) [48]. The radiative recombination from TTA generated singlet excited states is called delayed fluorescence [49]. Conversions due to TTA must obey the conservation of spin momentum and energy. Triplet to singlet transitions from $T_{\mathrm{m}=\pm 1}+T_{\mathrm{m}=\pm 1}->S_1$ also require a spin–flip mechanism, induced by hyperfine fields or spin orbit coupling. Transitions from $T_{\mathrm{m}=0}+T_{\mathrm{m}=0}->S_1$ can happen without performing a spin–flip mechanisms.

The energy difference of the first singlet and triplet state is given by the spin–exchange interaction energy ΔE_{ST}, which is also considered as twice the overlap integral of the respective RP electron wavefunctions [50].

2.8.1 External magnetic field effects

Up to now, the formation and recombination of RPs were not influenced by any external magnetic field. Magnetic fields only directly affect RPs in a quantum–state with spin $S \neq 0$. The mutual correlation between the electron and hole spin precession around the hyperfine field yields a $1:3$ singlet–triplet recombination statistic in organic materials. Therefore, in order to obtain magnetic field effects, the quantum–statistic of the spin–mixing has to be altered. An external magnetic field is able to induce an additional precession axis to the electron–hole polarization, which may interrupt the coherent spin–relation between them. The amplitude of MFEs can be expressed by the relative change in percentage, with

$$\mathrm{MFE}=\frac{I_{\mathrm{H}}-I_0}{I_0}\cdot 100\% \; . \tag{2.41}$$

Here, I_{H} and I_0 corresponds to the photoluminescence intensity with and without an external magnetic field. For low magnetic fields (LF), the MFEs, as a function of the magnetic field strength H, usually show a typical Lorentzian or non–Lorentzian lineshape (cf.Fig. 2.17(c)). These lineshapes can be defined as

$$\mathrm{MFE}_{\mathrm{LF}}(H)=\frac{H^2}{H^2+H_0^2} \qquad \text{(Lorentzian)} \; , \tag{2.42}$$

$$\mathrm{MFE}_{\mathrm{LF}}(H)=\frac{H^2}{(|H|+H_0)^2} \qquad \text{(non–Lorentzian)} \; , \tag{2.43}$$

where H is the applied magnetic field and H_0 is a material constant of typically a few mT. Usually additional high magnetic field features are observed in the measured MFE lineshape. Several mechanisms related to MFEs in organic semiconductors have been proposed, such as the hf–mechanism, the Δg–mechanism [51], and the electron spin orientation relaxation–mechanism. These mechanisms will be discussed in the following chapter.

The excited electron–hole RPs can possess different molecular excited states, with either singlet or triplet configuration. A schematic representation is shown in Fig. 2.16(b). The excited charge carriers can be split into intramolecular excitons if they are stuck on a single molecule A and intermolecular polaron pairs if electron and hole are located on two different molecules A and B, respectively. As described in the previous chapter, the radiative recombination of RPs arises from transitions from the excited states A^* or B^* into the ground states of A or B. It is obvious, that the formation of intermolecular excited states is preferable for the effective charge seperation in donor–acceptor photovoltaic devices. However, intermolecular RPs in a molecule A and B, require the preformation of an intramolecular excited state.

(1) $A \rightarrow A^*$, intramolecular exciton

(2) $A + B \rightarrow A^* + B \rightarrow (A^*B)$, intermolecular exciplex

(3) $A + B \rightarrow A^* + B \rightarrow (A^+)^* + B^- \rightarrow (A^+B^-)^*$, intermolecular charge transfer complex

(4) $A + B \rightarrow A^* + B \rightarrow (A^{\delta+}B^{\delta-})^* \rightarrow ((A^+)^* + B^-)$, donor–acceptor pairs

Scheme 1: Schematic representation of intra– and intermolecular states

As shown in the scheme 1 above, (1) corresponds to an intramolecular exciton on a single molecule A. Intermolecular states (2).–(4). can be split into exciplexes, charge transfer complexes, and donor–acceptor pairs, respectively [43]. An intermolecular exciplex (2) exists, if an excited molecule A^* is coupled with an unexcited molecule B, to form an excited complex molecule (A^*B). The state is called excimer, if molecule A and B are similar. If charge transfer occurs within an exciplex, one can speek of a so–called intermolecular charge transfere complex (3). The formation of such complexes requires the charge transfere between an excited molecule A^* and an unexcited molecule B, which leads to $(A^+)^* + B^-$, and the coupling between them $(A^+B^-)^*$. In less polar media, charge transfer complexes lead to donor–acceptor pairs shown in (4).

MFEs on intramolecular excited states

The unperturbed radiative recombination from intramolecular excited states, also yields a 1:3 singlet–triplet ratio. An external magnetic field can influence this statistic, by the redistribution of singlets and triplets in the excited states. If an external magnetic field strength is compareable to the internal hyperfine field strength, the triplet state splitting, namely the external Zeeman effect shown in Fig. 2.15(c), can alter the spin–mixing processes such as ISC and TTA. One can define two material specific requirements for the actual formation of MFEs in organic materials.

(1) $\Delta E_{\mathrm{EZ}} > \Delta E_{\mathrm{IZ}}$

(2) $\Delta E_{\mathrm{EZ}} > \Delta E_{\mathrm{ST}}$

Scheme 2: Requirements for the formation of MFEs in organic materials.

First, the external Zeeman splitting ΔE_{EZ} has to be much larger than the effect induced already by the internal Zeeman splitting ΔE_{IZ}. Secondly, ΔE_{EZ} should be in the range of the spin–exchange interaction energy ΔE_{ST} between the singlet and triplet state. The magnitude of ΔE_{ST} within the RP, rapidly decays with increasing the interradical distance r (c.f.Fig. 2.16(b)). ΔE_{ST} scales exponentially with the short–range interaction $J_0 \mathrm{e}^{-r/(2L)}$, where J_0 is the coupling matrix element of the RP wavefunctions, and L is the charge location radius. The e–h capture radius in intramolecular excitons is generally smaller than 1 nm. Usually, ΔE_{ST} can be neglected with interradical distances above 1 nm. In intramolecular excitons, ΔE_{ST} is usually in the range of 0.5 and 1.5 eV, which is much larger than the ΔE_{EZ} [43, 50]. The MFE condition (2) from scheme 2 is, therefore, not satisfied and it is unlikely for an external magnetic field to perturb the ISC channel in intramolecular excitonic states.

Another magnetic field dependent singlet–triplet transistion channel is offered by the TTA. Various studies showed, that external magnetic magnetic fields can weaken TTA in organic materials, leading to a reduced delayed fluorescence [41, 42]. This results in a negative photoluminescence MFE. However, it was shown in several studies, that the photoluminescence from intramolecular excited states shows unappreciable dependence of external magnetic fields [52, 43].

MFEs on intermolecular excited states

The intermolecular excited states (2)–(4), introduced in scheme 1, include exciplexes, excimers, charge transfer complexes, and donor–acceptor pairs, respectively. In solid organic semiconductors, the formation of intermolecular excited states implicates the energy transfer between different molecules and charge carrier diffusion. Intramolecular excitons can evolve into polaron pairs with larger electron–hole separation distance > 1 nm yielding intermolecular RPs. The dissociation can occur via the Poole–Frenkel process [53] or the Onsager process [54]. The relatively large interradical distance r in intermolecular excited states leads to a negligible spin–exchange energy ΔE_{ST}. As an immediate consequence, the required conditions in scheme 2 are fulfilled, giving rise to MFEs in intermolecular excited states.

RPs on different molecules can have either singlet or triplet electron configuration. Short– and long–range interactions between the electron and the hole, can affect the evolution of singlet and triplet excited states, on different molecules. The RPs are coupled with the long–range Coulombic attraction, which scales with $(q^2/(4\pi\varepsilon r))$. Here, ε is the dielectric permittivity and q the electron charge. The Coulombic attraction defines the binging energy in intermolecular excited states. For this study, it is noteworthy, that one can define a temperature–dependent Coulombic capture radius R_C

$$R_\mathrm{C} = \frac{q^2}{\varepsilon k_\mathrm{B} T} \; , \tag{2.44}$$

where k_B is the Boltzmann–constant and T the temperature. The Coulombic capture radius is inversely proportional to the temperature. The short–range internal magnetic interaction, like in intramolecular states, is responsible for spin–mixing mechanisms and also yields a $1:3$ singlet:triplet statistic for intermolecular RPs. In the absence of heavy–metal complex structure, the spin–mixing is led by the hyperfine fields rather than spin–orbit–coupling. The energy of an intermolecular excited state is either released radiative (photoluminescence), nonradiative, or via charge dissociation. In particular, the photoluminescence intensity I_PL of organic semiconductors consists of prompt recombination from excitons I_Exciton and from polarons I_Polaron

$$I_\mathrm{PL} = I_\mathrm{Exciton} + I_\mathrm{Polaron} \; . \tag{2.45}$$

The excitonic recombination channel can be defined as magnetic field–independent, whereas the polaronic recombination is considered as field–dependent. The magnetic field–dependence of intermolecular excited states, can in general be categorized into three possible MFE mechanisms: the $hf-$mechanism, which is the field dependent spin mixing (ISC and TTA) due to the short range interaction of radicals with nucleis, the $\Delta g-$mechanism [55], where the two radicals precess around the magnetic field with a different Larmor frequency (Eq. 2.39), and the electron spin orientation relaxation–mechanism. For the first two mechanism one can speak of reversible mechanisms, since singlet–triplet transitions have the permament character of a quantum–mechanical oscillation with a the characteristic frequency ω_ST between them. This is often referred to as the *singlet–triplet RP evolution* [46].

The first MFE mechanism corresponds to the hyperfine fields involved in intermolecular excited states and is, therefore, called $hf-$mechanism. The mechanism becomes present when the external magnetic field is in the range of the hyperfine field ($H_\mathrm{HF} \approx 10 - 100\,\mathrm{mT}$) at the position of the unpaired electron or hole. The hyperfine field acts as an additional local magnetic field and contributes to the vector sum of the effective magnetic field. The vector model introduced in (Fig. 2.15(a)), implies that with sufficient high external magnetic fields, the direction of the effective field and the external field coincides. For low magnetic fields, the effective field and the external field do not have the same direction and, therefore, the electron and hole within a RP can have a slightly different precession frequency (Eq. 2.39).

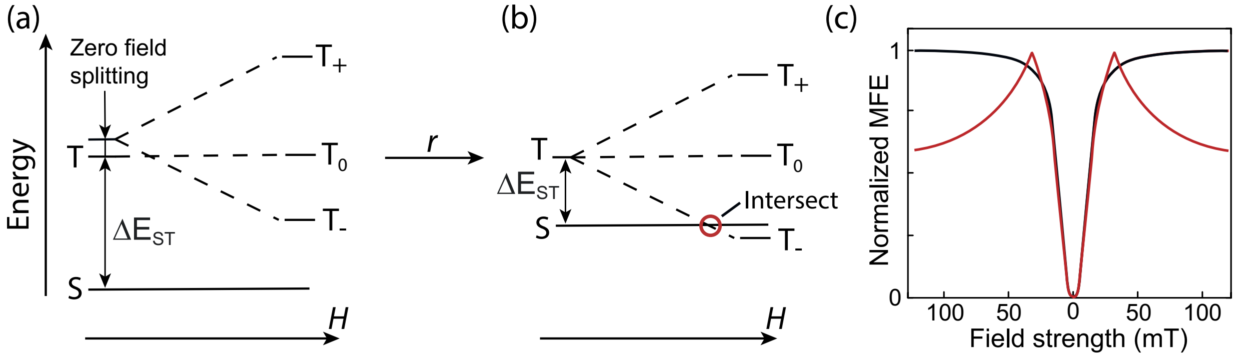

Figure 2.17: Energy level diagram of intermolecular triplet states in an external magnetic field. The spin exchange interaction energy ΔE_{ST} within the RP, rapidly decays with increasing the interradical distance r. (a) Short interradical distance (b) Large interradical distance. This can lead to an intersection point between the T_- and the singlet level. (c) Example plots of two different MFEs for short (red) and large (black) interradical distances.

As a consequence, the ISC and TTA channels are affected, which causes the redistribution of singlet–triplet excited states. The energy levels of the RPs in triplet configuration are subject to the Zeeman interaction. A sufficient high external magnetic field to satisfy the conditions in scheme 2, can induce two possible outcomes for the $hf-$mechanism. Fig. 2.17 shows a schematic representation of two intermolecular excited state configuration with (a) short– and (b) large–interradical distance. For short interradical distances, the spin–exchange energy ΔE_{ST} can be much larger than the external Zeeman splitting. An external magnetic field can reduce the energy difference between T_- and S, which is favourable for TTA, and thus increases the singlet ratio. The redistribution into singlet states has a positive effect on the photoluminescence intenisty, yielding positive MFEs. In contrast, a large interradical distance plus an external magnetic field could cause an intersection point between the T_- and the S energy level, the so–called level–crossing point (c.f. Fig. 2.17(b)). As a consequence, with increasing external magnetic field strength, this would lead to a positive MFE prior to the level–crossing point and a negative MFE after. The resulting MFE lineshape (red) is shown in Fig. 2.17(c). Even without an applied external magnetic field, the three triplet states are not degenerate. They are separated by a small energy called the zero–field splitting. The effect on the energy level diagram is shown in Fig. 2.17(a). For organometallic complexes such as, Pt–porphyrines, the zero–field increases by a factor of $10-100$ compared to pure organic semiconductors [13]. Therefore, the point of inflection in MFE experiments, would shift to higher magnetic fields depending on the actual strength of the zero–field splitting. An example will be given in the experimental section.

The second MFE mechanism arises due to slightly deviations in the Landé's $g-$factor of the two radicals (electron and the hole). Considering a situation where the radicals only feel the external magnetic field H_0, then the electron and hole precess around H_0 with the Larmor–frequency Eq. 2.39, as shown in Fig. 2.15(b). Transitions between the $S-$ to T_0-state are possible, because the precession phase difference between the electron and the hole spin $\vec{s_e}$ and $\vec{s_h}$, respectively, is 180°. Physical factors, that may dephase this mutual spin precession can induce $S-T_0$ transitions. However, dephasing of the spins cannot directly lead to $S-T_+$ or $S-T_-$ transitions, as they would require a spin–flip mechanism of one of the partners along the quantization axis. The frequency of the periodic $S-T_0$ transition can be calculated with the differences of the Larmor–frequencies

$$\omega_{\mathrm{ST0}} = \omega_{\mathrm{e}} - \omega_{\mathrm{h}} = (g_{\mathrm{e}} - g_{\mathrm{h}})\beta\hbar^{-1}H_0 = \Delta g \beta \hbar^{-1} H_0 \; , \tag{2.46}$$

where the indices e and h correspond to the electron and the hole, respectively. Organic radicals containing no heavy atoms $\Delta g \approx 0.001$ and the characteristic RP lifetime τ_{RP} is in the range of 10^{-9} s. For effective $S-T_0$ mixing the condition $\omega_{\mathrm{ST0}} \cdot \tau_{\mathrm{RP}} = 1$ should be fulfilled, which is true when $\omega_{\mathrm{ST0}} = 10^9$ rad/s, and the external magnetic field is ~ 10 T [46]. $\Delta g-$mechanisms are therefore only present with high external magnetic fields. If heavy atoms or complex ions of transition metals are involved, Δg can be even higher and, therefore, lower external magnetic fields could induce $\Delta g-$mechanisms.

2.9 Determining charge transfer states with sensitive sub–bandgap EQE measurements

Introduction

Today's polymer/non–fullerene blends in OSCs show remarkable power conversion efficiencies of up to 18%, and the extensive efforts to develop new materials are the right step towards efficient third–generation solar cells [7]. High external quantum efficiency ($\mathrm{EQE_{PV}}$) values above 80% and internal quantum efficiencies approaching 100% indicate that nearly all absorbed photons in the organic semiconductor are converted into electrons and transferred to the respective electrodes. This indicates that short–circuit currents are getting closer to the limit predicted by Shockley and Queisser [56].
However, the power conversion efficiency does not only depend on high short–circuit currents. Optimizing the open-circuit voltage is equally essential for high power conversion efficiencies. The precise measurement of the photocurrent can also give a detailed insight into the upper limit of the open–circuit voltage. As already mentioned in section 2.4, the origin of the open–circuit voltage V_{oc} can be explained with complex internal fields that arise from different work–functions within an OSC's architecture. However, the measurement of these internal fields can be highly challenging. A more accessible ansatz was offered by

Vandewal et al., who related externally measurable electro–optical spectra to the V_{oc}, by the principle of detailed balance and the quasi–equilibrium theory [57]. The fundamental theory was already answered by Shockley and Queisser in 1961 [56], where they found that V_{oc} in a p–n junction solar cell is maximal if the excited charges only recombine radiatively. In real solar cells, this is often not the case, and non–radiative decay channels lead to not negligible voltage losses. The precise characterization of these voltage loss mechanisms is crucial for understanding the vast discrepancy between the device V_{oc} and the energy gap of the dominant solar cell absorber.

Vandewal could explain the origin of the V_{oc} with the formation of ground–state charge–transfer complexes (CTC) [57, 58]. A ground–state CTC is formed between the donor and acceptor molecules of the blend film. The excitation of these newly formed states leads to the charge–transfer (CT) excitons. The energetic position of the CT state is sometimes empirically derived from the energetic difference between the HOMO level of the donor material and the LUMO level of the acceptor material. However, the precise characterization of the voltage losses in an OSC requires a more accurate determination of the CT state energy. With sensitive optical experiments, transitions from CTC– to CT–states can be visualized as additional transition bands in the low–energy tail of the absorption and EQE spectrum. EQE spectra were measured with an amplified spectral response setup (compare section 4.1.5). The radiative decay of the CT excitons is detected by measuring the electroluminescence (EL) spectra obtained by applying a forward voltage to the OSC (compare section 4.1.6).

Spectral broadening and the determination of the optical gap and CT state energy

The determination of the optical gap energy E_{opt} of a hypothetical solar cell with an ideal stepwise absorption spectrum is trivial. However, in real OSC materials, static and dynamic disorders, and the presence of weakly absorbing CT states, lead to rather shallow absorption tails. The absorption and emission spectra of organic semiconductor thin films typically show discrete broad peaks. The main reasons for the spectral broadening of the peaks are the electron–phonon coupling and the low–frequency molecular vibrations [59]. Fig. 2.18(a) shows optical transitions between the ground–state GS and the excited–state ES as a function of a generalized reaction coordinate in a Gibbs free–energy diagram. Energetic transitions from photon absorption (blue) and photon emission (red) are indicated with vertical arrows. The energetic transitions at the maxima of the absorption $E_{\mathrm{max,abs}}$ and the emission $E_{\mathrm{max,EL}}$ spectral are shown as solid vertical arrows. Due to the Franck–Condon principle, the reaction coordinate stays invariant during optical transitions. The horizontal lines within the GS and ES indicate the low–frequency vibrational energy levels. The spacing between them is less

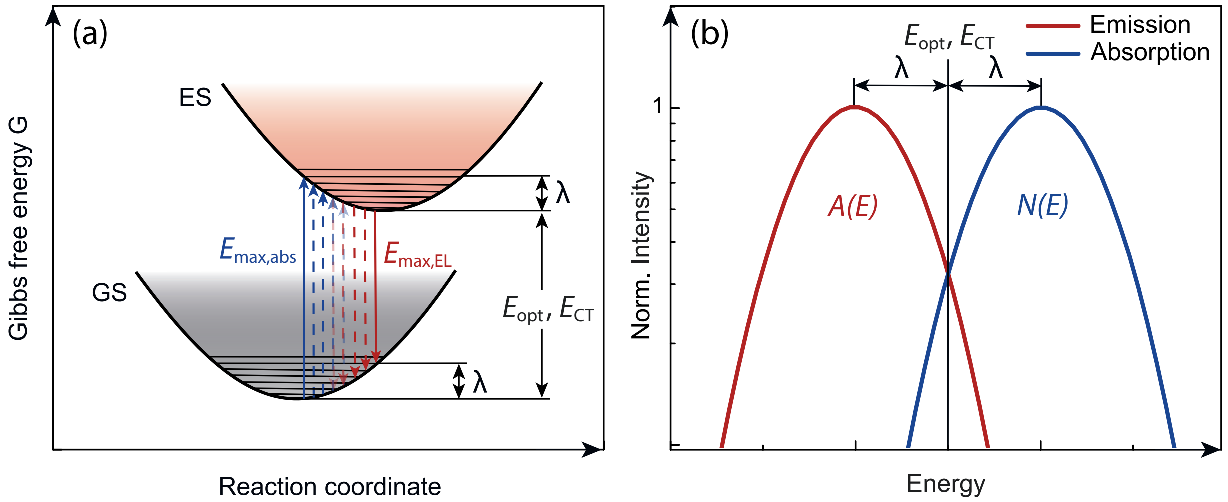

Figure 2.18: (a) Optical transitions shown in a Gibbs free–energy diagram with displaced potential wells for the ground–state GS and the excited–state ES as a function of a generalized reaction coordinate. The vertical solid arrows indicate the peak energies of the absorption $E_{\text{max,abs}}$ (blue), and the emission $E_{\text{max,EL}}$ (red) spectrum. The reorganization energy is indicated by λ. (b) Schematically absorption and emission specturm on a logarithmic scale. Graphs redrawn from [59].

than the thermal energy. The photon absorption and emission between thermally populated low–frequency vibrational states of the GS and the ES consequently result in absorption energies below $E_{\text{max,abs}}$ and emission energies above $E_{\text{max,EL}}$. These optical transitions are indicated with dashed vertical arrows. In the framework of Marcus theory, this absorption $A(E)$ and emission $N(E)$ transitions results in a Gaussian spectral lineshape as a function of photon energy E with the reorganization energy λ.

$$A(E) \sim E \ \exp\left(-\frac{(E - E_{\text{opt}} - \lambda)^2}{4\lambda k_{\text{B}} T}\right) \tag{2.47}$$

$$N(E) \sim E^3 \ \exp\left(-\frac{(E - E_{\text{opt}} + \lambda)^2}{4\lambda k_{\text{B}} T}\right) \tag{2.48}$$

Hereby, k_{B} is the Boltzmann constant and T the temperature.

Schematic plots of the normalized Eq. 2.47 (red) and Eq. 2.48 (blue) are shown in Fig. 2.18(b). The curves $A(E)$ and $N(E)$ intersect exactly at the optical gap energy E_{opt},separated by 2λ (Stokes shift). It should be noted that a so-called photothermal deflection spectroscopy (PDS) setup would be required for sufficiently accurate absorption measurements. Since the internal quantum efficiencies of the organic donor-acceptor thin films on the low-energy tails are rather constant, absorption and EQE_{PV} spectra are interchangeable here [60].

For real EQE_{PV} and emission spectra, E_{opt} and E_{CT} can be determined by fitting Eq. 2.47

to the low energy reduced $\mathrm{EQE_{PV}}$ tail and Eq. 2.48 to the high energy reduced emission tail, respectively. The so–called reduced $\mathrm{EQE_{PV}}$ and reduced emission spectrum are derived by dividing the $\mathrm{EQE_{PV}}$ spectra with E and the emission spectra with E^3. By normalizing the reduced spectra to the maximum of the fitted peaks, one can obtain the so–called mirror–image–spectra, and the intersection point of the $\mathrm{EQE_{PV}}$ and EL spectrum is exactly E_{opt} for pristine and E_{CT} for blend films.

Voltage losses

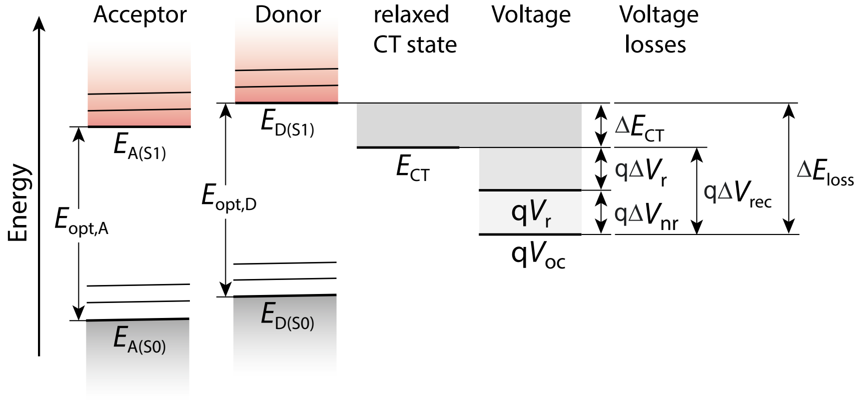

Figure 2.19: Energy level diagram showing the first excited singlet energies of the donor $E_{\mathrm{D(S1)}}$ and the acceptor $E_{\mathrm{A(S1)}}$, the intermolecular charge transfer state E_{CT}, and the voltage losses due to radiative recombination ΔV_{r}, and non–radiative recombination ΔV_{nr}. The optical bandgap energies $E_{\mathrm{opt,D,A}}$ for donor and acceptor, respectively, are determined as described in the main text.

After the determination of E_{opt} for the donor and the acceptor material, and E_{CT} of the blend film, one can now perform a detailed analysis of the voltage losses in the OSC. The V_{oc} values can be measured with a solar simulator at standard conditions (see section 4.1.2).

The total energy loss ΔE_{loss} resulting from converting an excited singlet electron pair in the donor into a free electron–hole pair with the chemical potential qV_{oc} can also be expressed with

$$\Delta E_{\mathrm{loss}} = E_{\mathrm{opt,D,A}} - qV_{\mathrm{oc}} \;, \tag{2.49}$$

where q is the elementary charge. The corresponding voltage losses are expressed with

$$\Delta V_{\mathrm{loss}} = \frac{\Delta E_{\mathrm{loss}}}{q} \;. \tag{2.50}$$

A schematic energy level diagram to illustrate the energy losses in a photovoltaic device is shown in Fig. 2.19. The indices D corresponds to the donor and A to the acceptor material.

The indices r and nr are referred to as radiative and non–radiative losses, respectively, and summarized with the recombination losses indexed with rec. The energetic loss accompanied by the CT–state is calculated with

$$\Delta E_{\mathrm{CT}} = E_{\mathrm{opt,D,A}} - E_{\mathrm{CT}} \ . \tag{2.51}$$

This energy difference is usually considered as the driving force for charge separation in OSCs [61]. Due to the different recombination channels of free charge carriers, the V_{oc} is lower as compared to E_{CT}/q. The corresponding recombination loss of the V_{oc} is expressed with

$$\Delta V_{\mathrm{rec}} = \frac{1}{q} E_{\mathrm{CT}} - V\mathrm{oc} \ . \tag{2.52}$$

At room temperature and standard illumination conditions, recombination losses in OSCs typically make up a large part of the total losses and are often in the range of $\sim 0.6\,\mathrm{V}$. The recombination losses can be split into radiative ΔV_{r} and non–radiative ΔV_{nr} losses. As already mentioned in the introduction of this chapter, if only radiative recombination would occur, V_{oc} would reach its upper limit. V_{r} can be expressed with

$$V_{\mathrm{r}} = \frac{k_{\mathrm{B}}T}{q} \ln\left(\frac{j_{\mathrm{sc}}}{j_0^r}\right) \tag{2.53}$$

Hereby, j_{sc} is the short–circuit current density obtained by integrating the $\mathrm{EQE_{PV}}(E)$ product with the the known spectral photon flux $\Phi^{\mathrm{AM1.5}}_{\mathrm{ph},E}$ for an AM1.5 spectrum (compare Eq. 2.25). The radiative limit of the dark current density j_0^r is obtained by the integration of the product of the $\mathrm{EQE_{PV}}(E)$ with the black–body spectrum at temperature T $\Phi^T_{BB,E}$.

$$j_0^r = \frac{q}{\mathrm{EQE_{EL}}} \int \mathrm{EQE_{PV}}(E)\Phi^T_{BB,E} dE \ . \tag{2.54}$$

$\mathrm{EQE_{EL}}$ corresponds to the EL external quantum efficiency, which is the ratio of the radiative decay rate to the sum of the radiative and non–radiative decay rate

$$\mathrm{EQE_{EL}} = \frac{\mathit{\Gamma}_r}{\mathit{\Gamma}_r + \mathit{\Gamma}_{nr}} \ . \tag{2.55}$$

$\mathit{\Gamma}_r$ and $\mathit{\Gamma}_{nr}$ are the radiative and non–radiative decay rate, respectively. If only radiative recombination occurs $\mathrm{EQE_{EL}} = 1$.

The $\Phi^T_{BB,E}$ spectrum is expressed with

$$\Phi^T_{BB,E} = \frac{2\pi}{h^3c^3} E^2 \exp\left(-\frac{E}{k_{\mathrm{B}}T}\right) \ . \tag{2.56}$$

Sensitive measurements of the $\mathrm{EQE_{PV}}$ are essential, as the $\Phi^T_{BB,E}$ spectrum drastically decreases with increasing energy and, therefore, only the low energy tail of the EQE contributes to the integral in Eq. 2.54. For a more detailed derivation of Eq. 2.54, the reader is referred to [57]. The resulting voltage losses due to radiative recombination can be expressed with

$$\Delta V_{\mathrm{r}} = \frac{1}{q} E_{\mathrm{CT}} - V_{\mathrm{r}} \tag{2.57}$$

The difference between the measured V_{oc} and the calculated radiative limit V_{r} is then related to the non–radiative recombination losses via

$$\Delta V_{\mathrm{nr}} = V_{\mathrm{r}} - V_{\mathrm{oc}} \ . \tag{2.58}$$

Furthermore, ΔV_{nr} can be related to the $\mathrm{EQE}_{\mathrm{EL}}$ by

$$\mathrm{EQE}_{\mathrm{EL}} = \exp\left(-\frac{q\Delta V_{\mathrm{nr}}}{k_{\mathrm{B}}T}\right) \ . \tag{2.59}$$

It is, therefore, important maximize the $\mathrm{EQE}_{\mathrm{EL}}$ in order to minimize the non–radiative recombination losses. Typical values for the $\mathrm{EQE}_{\mathrm{EL}}$ of OSCs are from 10^{-6} to 10^{-8} [62].

By the principle of detailed balance Rau [63] introduced that the external quantum efficiency and the electroluminescent emission of a solar cell can be connected via

$$\Phi_{EL}(E,V) = \mathrm{EQE}_{\mathrm{PV}} \Phi_{BB}(E) \left(\exp\!\left(\frac{qV}{k_{\mathrm{B}}T}\right) - 1\right) \ . \tag{2.60}$$

Here $\Phi_{EL}(E,V)$ is the electroluminescence spectral photon flux and $\Phi_{BB}(E)$ is the black–body spectrum at 300 K.

3 Materials

This thesis includes donor–acceptor blends consisting of two polymers, two non–fullerene acceptors, and one reference fullerene acceptor. All materials are currently used in the OSC community. The material combinations were chosen as they show remarkable power conversion efficiencies of up to 13% with high reproducibility. In this chapter the used chemicals and materials for the device fabrication are discussed.

3.1 Electrodes and interlayers

Indium tin oxide (ITO) is widely used as a transparent bottom electrode. It has excellent transmission properties in the spectral region of the sun emission (cf. Fig. 2.1(a)) while maintaining high electrical conductivity. In inverted OSCs, the ITO contact is used as the cathode and has a high work function of $\sim -4.7\,\mathrm{eV}$ (cf. Fig. 3.2(d)). The shown work function values were taken from Li Yan et al. [64]. For the organic semiconductors in the devices, the ITO work function is too high and, therefore, cannot be used directly as the cathode. A practical solution is to lower the work function of the ITO by introducing a cathode interlayer. A widely used interlayer material for OSCs is polyethylenimine (PEI). However, the development of non–fullerene small molecule acceptors also required the introduction of new interlayer materials. Lin Hu et al. showed that amine–containing interlayers, such as PEI, can chemically react with non–fullerene acceptor materials and permanently destroy the electronic structure and the intramolecular charge transfer [65]. For the inverted OSC architecture, n-type metal oxides such as zinc oxide (ZnO) is widely used as ETL instead of PEI [66]. Numerous publications among the production of thin–film ZnO layers were published. A widely used production technique is the sol–gel method, where solid films were fabricated from single molecules. The HOMO energy level of the ZnO–film derived from sol–gel methods lies at $\sim -7.7\,\mathrm{eV}$, and the LUMO–level is at $\sim -4.4\,\mathrm{eV}$. The chemical composition of the ZnO sol–gel will be discussed in the experimental section.

The analog to the electron–transport–layer on the ITO, is the hole–transport–layer (HTL) on top of the photoactive layer. A transition metal oxide, namely molybdenum oxide (MoO_x), is a widely used HTL anode interlayer [67]. It alters the work function of the metal top contact to match the HOMO energy level of the polymer material in the bulk–heterojunction.

Silver (Ag) is a commonly used low work function material and utilized as an anode in inverted OSCs. The work function of Ag is $\sim -4.3\,\mathrm{eV}$. For standard solar cell configuration aluminium Al is an often used top–contact. The work function of Al lies at $\sim -4.1\,\mathrm{eV}$. Both materials are excellent electrical conductors and easy to process in vapor deposition methods (see chapter 4.2.2).

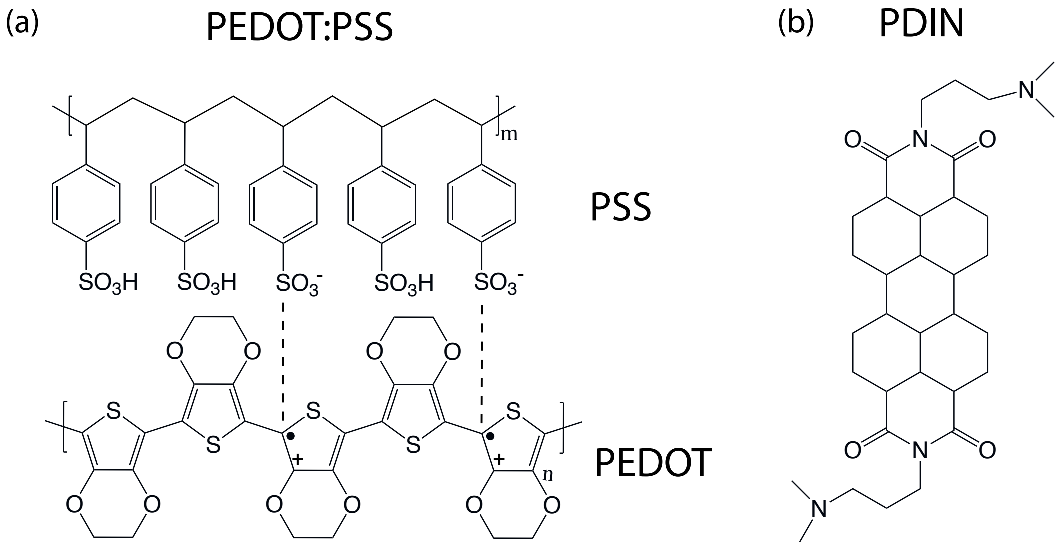

Figure 3.1: Chemical structure of (a) the conducting polymer PEDOT:PSS PH1000, and (b) the ETL interlayer perylene diimide amino (PDIN).

Flexible OSCs also require flexible transparent electrodes. A promising next–generation ITO–free electrode can be fabricated from a high conductive polymer namely poly(3,4–ethylenedioxythiophene):polystyrene sulphonate (PEDOT:PSS PH1000). This electrode has excellent optical transparance at visible spectral range and shows high flexibility and stretchability [68]. The chemical structure of PEDOT:PSS PH1000 is shown in Fig. 3.1(a). The HOMO energy level is at $\sim -5.5\,\text{eV}$. Transparent PEDOT:PSS PH1000 electrodes are a p–type material and, therefore, hole charge carrier conductive. Often a lower conductive derivative of PEDOT:PSS is added on top of the PH1000 as an HTL interlayer.

Another flexible transparent electrode system is a hybrid silver nanowire–graphene (Ag NW–Graphene) conductive film. This hybrid electrodes exhibit remarkable mechanical flexibility and transparency. The work function of Ag NW–Graphene is at $\sim -4.0\,\text{eV}$ [69]. In this work the Ag NW–Graphene cunductive film is used as a stand–alone bottom electrode.

For OSCs in the standard configuration, an ETL is introduced between the photoactive layer and top-contact. Up-and-coming solution–processed n–type materials are perylene diimides (PDI), especially with amino (PDIN) terminal substituents. The chemical structure of PDIN is shown in Fig. 3.1(b). The material has a HOMO energy level at $\sim -6.0\,\text{eV}$ and a LUMO level at $\sim -3.7\,\text{eV}$ [70]. The material's primary role is its ability to create large interfacial dipoles that induce a shift in the vacuum level, altering the work function of the top electrode.

3.2 PBDB-T-2F, IT4F and PC71BM

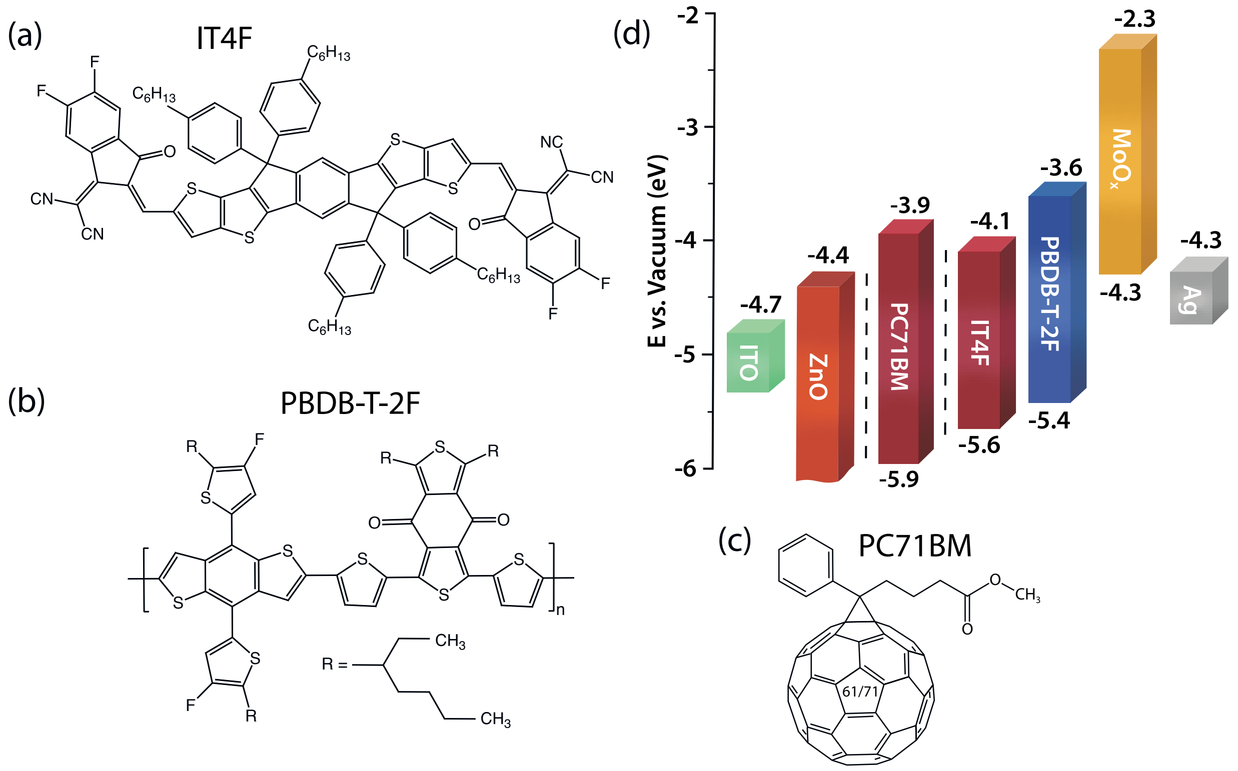

Figure 3.2: Chemical structure of the (a) IT4F non–fullerene acceptor material and the (b) PBDB-T-2F organic semiconductor polymere. (c) PC71BM fullerene structure (d) Energy level diagram of the solar cell components with contacts.

The progressive improvement of OSC performance requires the design of highly efficient acceptor materials. One representative of such acceptor materials was synthesized by Wenchao Zhao et al. and has the abbreviated name IT4F [71]. They used the rational molecular optimization of the common ITIC [72] acceptor material via fluorination to enhance the photovoltaic performance of OSCs. The fluorination of non–fullerene acceptor materials results in downshifted HOMO and LUMO energy levels without yielding strong steric hindrance of the fluorinated molecule. Fluorination also enhances inter/intramolecular interactions due to the noncovalent interactions of F to H and S to F [73]. The chemical structure of IT4F is shown in Fig. 3.2(a). This small molecule acceptor is based on a bulky seven–ring fused core indacenodithieno[3,2-b]thiophene (IT), with four 4-hexylphenyl groups on it. The IT group is end-capped with 2-(3-oxo-2,3-dihydroinden-1-ylidene)malononitrile (INCN) groups substituted with the 4-flourine atoms [72]. The IT4F molecule has a so-called Acceptor–Donor–Acceptor (A–D–A) structure, where electron–donating units constitute the core and electron–deficient groups serve as terminal blocks. The ITIC backbone molecule includes electron–pushing and electron–pulling units, where the electron–pushing units are shield by bulky non–conjugated side chains [74]. The IT4F acceptor has the HOMO energy level at $\sim -5.6\,\mathrm{eV}$ and the LUMO level at $\sim -4.1\,\mathrm{eV}$ yielding an optical bandgap of $\sim 1.5\,\mathrm{eV}$. IT4F was purchased from 1−*Material INC* and used without further purification.

In order to make good use of the broad and strong light absorption capability of IT4F without sacrificing the V_{oc}, a promissing donor material namely PBDB-T-2F or sometimes PM6 was synthesized by Maojie Zhang and coworkers [75]. They used the available PBDTBDD polymer and attached fluorine atoms onto the endcap groups to enhance the photovoltaic performance of OSCs. The chemical structure of the copolymer is shown in Fig. 3.2(b). PBDB–T–2F is based on 4,8-bis(5-(2-ethylhexyl)-4-fluorothiophen-2-yl)benzo[1,2-b:4,5-b']-dithiophene (BDT-F) and 1,3-bis(thiophen-2-yl)-5,7-bis(2-ethyl-hexyl)benzo-[1,2-c:4,5-c']-dithiophene-4,8-dione (BDD). The copolymer has a HOMO energy level of $\sim -5.4\,\mathrm{eV}$ and a LUMO level at $\sim -3.6\,\mathrm{eV}$, with a resulting optical bandgap of $\sim 1.8\,\mathrm{eV}$. The material was purchased from 1−*Material INC* and used without further purification.

In the field of bulk–heterojunction OSCs 6, 6-phenyl-C61-butyric acid methyl ester (PC61BM) is to date, one of the most studied OSC acceptors on the market [76]. Since the discovery in 1995 by G. Yu et al. [23], a tremendous number of scientific papers were published. PC61BM is a soluble FA derivative of the C_{61} buckyball, first synthesized 1995 from J.C. Hummelen et al. [77], and used as a n–type acceptor material in OSCs. The PC61BM fullerene acceptor material is also available with a C_{71} buckyball. This derivative enhances the light absorption in the visible spectral regime and increases the power conversion efficiency of polymer–fullerene blends compared to the C_{61} type.Fig. 3.2(c) shows the chemical structure of the PC61/71BM molecule. The molecule has a low HOMO energy level of $\sim -5.9\,\mathrm{eV}$ and a LUMO level of $\sim -3.9\,\mathrm{eV}$, resulting in an optical bandgap of $\sim 2.0\,\mathrm{eV}$. The PC71BM acceptor material is used within this work as a state–of–the–art fullerene reference to the non–fullerene acceptor materials. It was purchased from 1−*Material INC* and used without further purification.

3.3 PTB7-Th and EH-IDTBR

The next donor–acceptor group is represented by the polymer PTB7-Th (sometimes PBDTTT-EFT or PCE10) and the non–fullerene small molecule acceptor EH-IDTBR [78]. The PTB7-Th polymer was choosen because of its excellent stability and performance together with the EH-IDTBR acceptor. PCE of up to 11% were reported in literature [79].

The low–bandgap donor polymer PTB7-Th was syntesized by Si–Hao Liao et al. [80]. The group incorporated a 2-ethylhexyl-thienyl group to the preexisting PTB7 molecule to downshift the HOMO and LUMO level energetically. The chemical structure is shown in

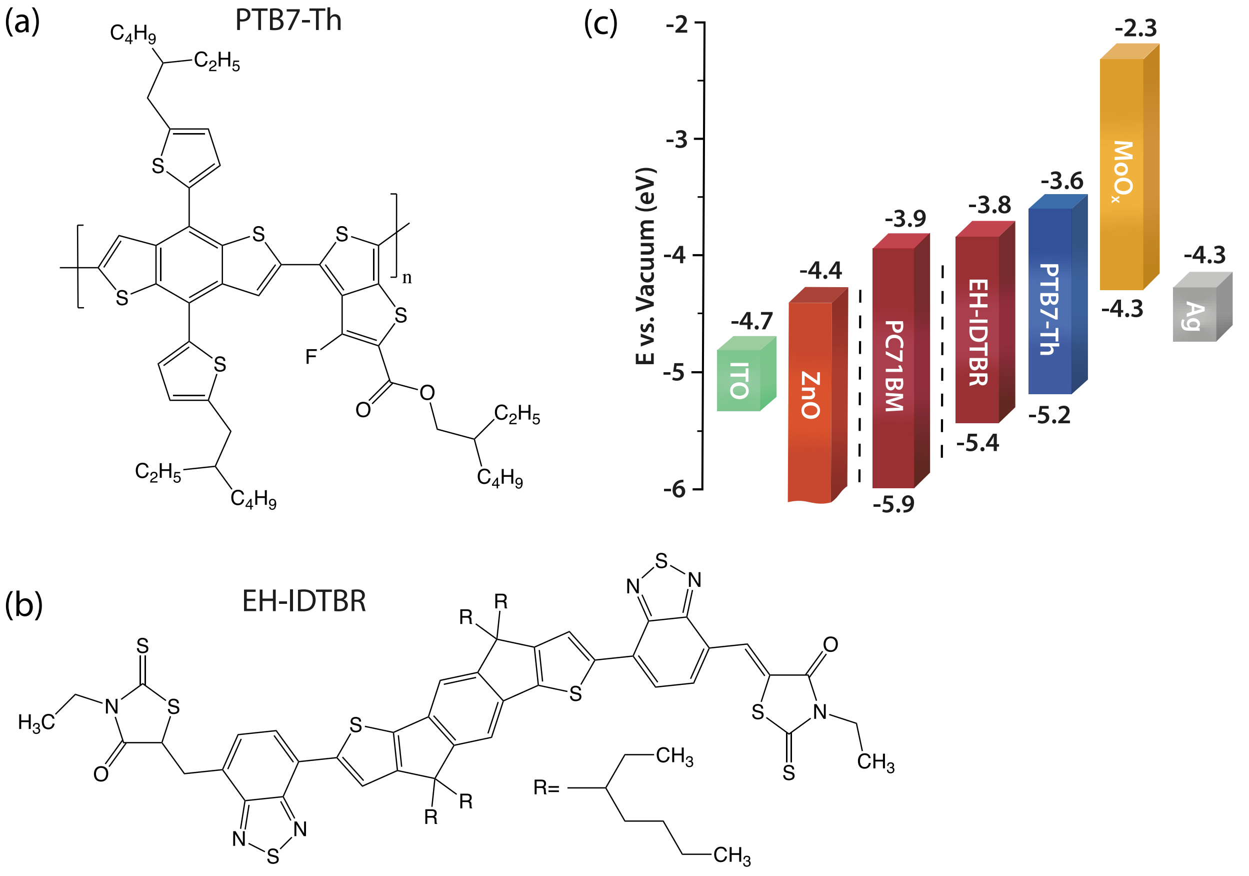

Figure 3.3: Chemical structure of the (a) PTB7-Th organic semiconductor polymere and (b) the EH-IDTBR non–fullerene acceptor material. (c) Energy level diagram of the solar cell with contacts.

Fig. 3.3(a). PTB7-Th is designed as copolymere and based on the two basic fused–ring comonomer units benzodithiophene (BDT) and fluorine–substituted thieno[3,4-b]thiophene (F-TT) with the 2-ethylhexyl carboxylate group. The full name of PTB7-Th is Poly[4,8-bis(5-(2-ethylhexyl)thiophen-2-yl)benzo[1,2-b;4,5-b']dithiophene-2,6-diyl-alt-(4-(2-ethylhexyl)-3-fluorothieno[3,4-b]thiophene-)-2-carboxylate-2-6-diyl)]. The copolymer has a HOMO energy level of $\sim -5.2\,\mathrm{eV}$ and a LUMO level at $\sim -3.6\,\mathrm{eV}$, with a resulting optical bandgap of $\sim 1.6\,\mathrm{eV}$ (cf. Fig. 3.3(c)). The material was purchased from 1−*Material INC* and used without further purification.

The small molecule acceptor EH-IDTBR was synthesized by Sarah Holliday and coworkers [78]. The chemical structure of the acceptor is shown in Fig. 3.3(b). It is based on the indacenodithiophene (IDT) core and alkylated using branched 2-ethylhexyl side chains and has the full name Poly[4,8-bis(5-(2-ethylhexyl)thiophen-2-yl)benzo[1,2-b;4,5-b']di- thiophene-2,6-diyl-alt-(4-(2-ethylhexyl)-3-fluorothieno[3,4-b]thiophene-)-2-carboxylate-2-6-diyl. EH-IDTBR has its HOMO energy levels at $\sim -5.4\,\mathrm{eV}$ and the LUMO level at $\sim -3.8\,\mathrm{eV}$, which results in an optical bandgap of $\sim 1.6\,\mathrm{eV}$. The material was purchased from 1−*Material INC* and used without further purification.

3.4 Reference materials

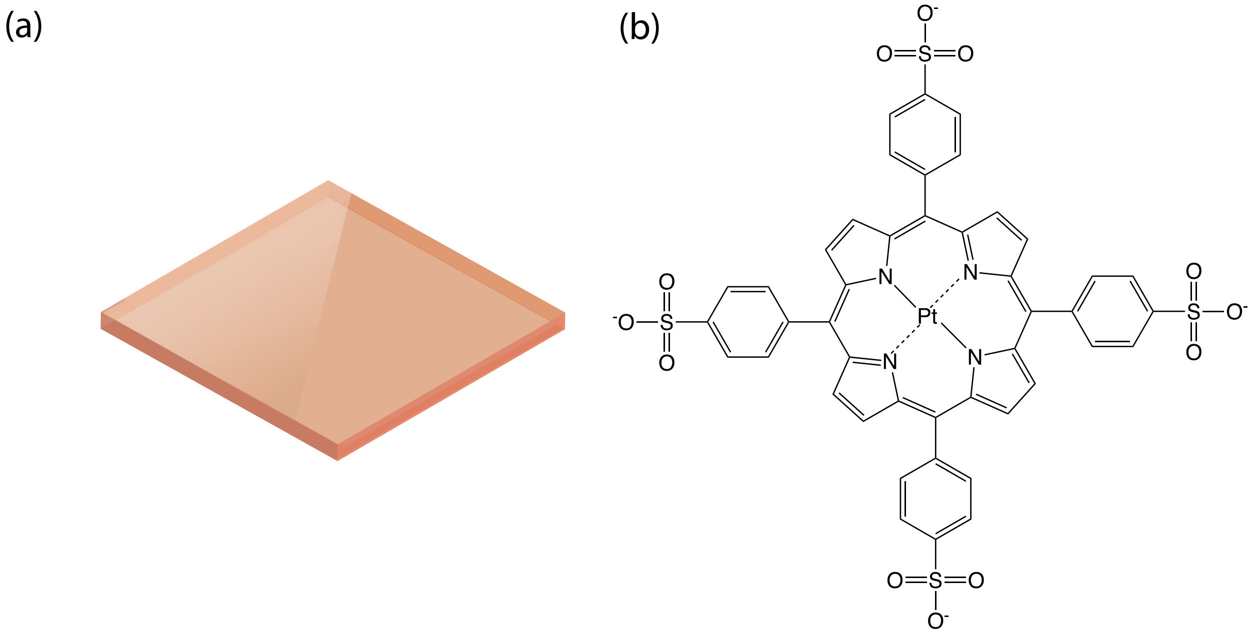

Figure 3.4: (a) Singlet emitter: orange fluorescent acryl glass. (b) Triplet emitter: organometallic Pt-TSPP porphyrin molecule.

The magnetic field effects on the photoluminescence of organic semiconductors were experimentally investigated with the magnetooptical experimental setup discussed in chapter 4.1.8. As proof of the theoretical principle, two reference materials were examined in addition to the OSC compounds. First, an orange fluorescent singlet emitter made of acrylic glass was used to show the magnetic field–independence of photons emitted from excited singlet states and second, an organometallic porphyrin molecule with a field–dependent triplet phosphorescence. Both materials are shown in Fig. 3.4.

Porphyins are a class of organic luminescent moleculse of both natural and synthetic origin. The determining characteristic is the presence of the eponymous ring structure (cf. Fig. 3.4(b)). The porphyrom ring can be described as a union of four pyrrole rings linked by four methine bridges to a macrocycle. The term macrocycle refers to the tendency of porphyrins to form square –planar complex compounds which are large enough to accept a metal ion inside. The resulting metal–porphyrin complexes (metalloporphyrins) thus differ significtantly in ther photophyiscal properties from the metal–free porphyrins. However, both classes share the fact that the $\pi-$system, which is delocalzed on the porphyrin ring, is responsible for the optical transitions. The most important difference between the metalloporphyrins and the metal–free porphyrins is their photoluminescence properties. Ther prescence of a heavy metal atom with high spin–orbit coupling in the coordination center of the porphyin ring leads to an increase in intersystem crossings (ISC). This leads to a drastic increase in phosphorescence with simultaneously reduced fluorescence. The pronounced phosphorescence of the investigated $5, 10, 15, 20-$Tetrakis-($4-$Sulfonatophenyl)porphyrin-Pt(II) (Pt-TSPP) in this work is due to the Pt(II) ion in the complex center.

4 Experimental section

4.1 Characterization methods and instruments

This chapter describes the characterization methods and the instruments used for the experiments and their relevant setups.

4.1.1 Absorption measurements

The absorbance spectra of the used materials within this work were measured with a *PerkinElmer* spectrometer. All materials were studied in a thin film configuration spin–coated on a glass microscope slide. The data analysis was provided by the built–in *PerkinElmer* software and used without further processing.

4.1.2 Solar–simulator

A solar–simulator is a tool that provides controlled solar radiation from UV to NIR spectral range on a laboratory scale. It is designed to test solar cells under standardized conditions. The most common light source used is a xenon arc-discharge lamp. Such lamps offer high intensities and a light spectrum that matches well to natural sunlight. The solar–simulator used in this work provides a continuous AM1.5 spectrum (cf.Fig. 2.1), at 1 Sun intensity, inside a nitrogen filled glove–box. A *Keithley* 2400 is used to measure the $j(V)$ curve of the examined solar cell. Data analysis was performed by using custom software written in *LabView*.

4.1.3 Profilometer

Layer thicknesses in the nanometer range can be measured with a so–called stylus–profilometer. A diamond stylus (needle) is in contact with the sample surface and moved laterally across the sample. Vertical stylus displacement caused by roughness or scratches on the sample surface is recorded as a function of the position. The layer thickness can be determined by deliberate scratches that protrude through the entire layer cross-section. *Bruker* provides an automated laboratory solution, with the type name *DektakXT*, that can measure the layer thickness of OSCs.

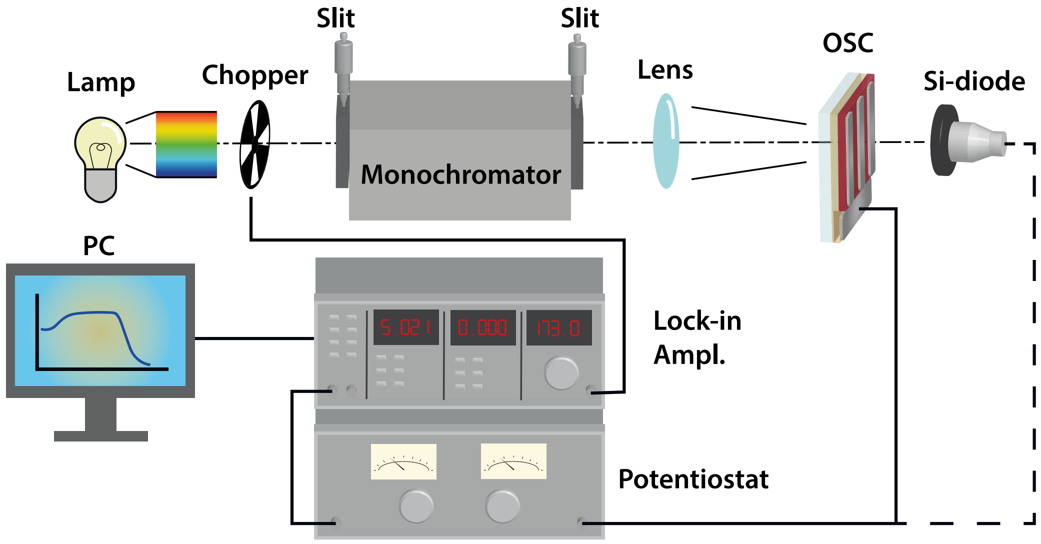

Figure 4.1: Schematic of a spectral response setup to measure the external quantum efficency of a solar cell.

4.1.4 Spectral response setup

A UV–VIS–NIR spectral response setup can be used to measure the external quantum efficiency (EQE) of a solar cell. A schematic setup is shown in Fig. 4.1. The setup consists an arc discharge lamp of *LOT* with a good spectral intensity from UV till NIR. The emitted light of the lamp, passes a chopper-wheel, which is connected to a lock-in amplifier (Stanford Research SR830). Next, a Cornerstone^{TM} 130 $1/8m$ monochromator is used to select a particular wavelength of the optical spectrum. The light exiting the monochromator passes a slit and is then focused, with a lens, onto the solar cell or a reference Si-diode. A potentiostat is used to convert the measured current into voltage and also can amplify the signal if needed. The aforementioned lock-in amplifier measures the output of the potentiostat and is connected to a PC with a data analysis program written in LabView.

4.1.5 Amplified spectral response setup

Sub–bandgap external quantum efficiencies can be measured by using a so–called amplified spectral response setup. The difference between the amplified setup and the system shown in section 4.1.4 is the Tungsten–Halogen light source, and instead of a potentiostat, it uses an instrumentation amplifier. The *Acton ARC* Tungsten–Halogen light source model TS–428S provides a good light intensity in the NIR spectral region. With the help of the instrumentation amplifier, one can measure quantum efficiencies with a magnitude down to

10^{-5}. The sample solar cell is directly placed at the exit slit of the *Acton ARC* SpectraPro–300i spectrometer and shielded against ambient lights. Longpass filters (600, 650, 700 nm) were put in the beam path before the entrance slit of the spectrometer to cut off the VIS spectral region.

4.1.6 Electroluminescence setup

The electroluminescence EL of the OSCs can be measured by applying a forward voltage to the contacts of the cell and analyzing the emitted photons with a spectrometer. The cell is therefore directly placed at the entrance slit of a monochromator. A spectrometer from *ANDOR* SR303i in combination with a iDUS CCD Si camera, is used to record the EL spectrum. A *Keithley* 2400 is used to apply the voltage to the contacts of the cell. The iCCD spectrometer was calibrated with a tungsten halogen radiometric standard lamp from *Ocean Optics* (HL–3plus–cal).

4.1.7 ModuLab XM PhotoEchem optical and electrical measurement system

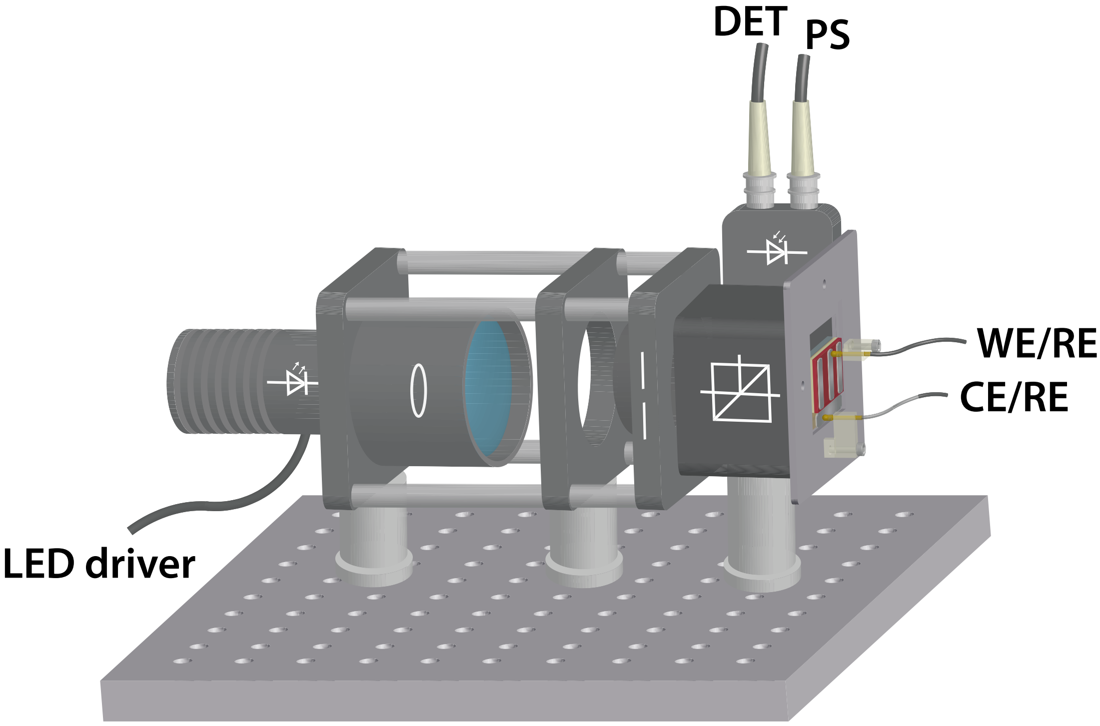

Figure 4.2: Schematic representation of the ModuLab XM PhotoEchem optical and electrical measurement system.

Intensity modulated photocurrent-, or photovoltage spectroscopy (IMPS/IMVS) measurements were carried out with the ModuLab XM PhotoEchem optical and electrical measurement system from *Solartron Analytical, AMETEK*. This system is a fully integrated photoelectrochemical measurement system with automated data analysis software. A full description of the ModuLab XM PhotoEchem system, including example experiments and results, is available in an application note from Solartron Analytical. The optical setup consists of a 575 nm LED (*Thorlabs* M575L2), which is controlled by the attached *Thorlabs* DC2100 LED driver. The light is then focused with a lens into the sample plain. An aperture reduces the beam size and the remaining ambient light. A 50 : 50 anti–reflective coated beam splitter directs an equal amount of light onto the solar cell and the NIST traceable reference Si–photodetector (*Thorlabs* PDA36A-EC). The photodetector is connected to the detection input (DET) of the potentiostat/galvanostat and the power supply (PS). Working electrode (WE), counter electrode(CE) and reference electrode (RE) of the potentiostat are directly connected to the contacts of the solar cell. IMVS measurements were performed under open–circuit conditions under illumination, with a 10% modulation amplitude. The light modulation frequency was altered with ten steps per decade from 1 Hz to 1 MHz. IMPS measurements were carried out under short–circuit conditions and with the same data acquisition settings as with the IMVS measurements. Data analysis was performed by using custom software written in *Mathematica*.

The ModuLab XM PhotoEchem optical and electrical measurement system was originally designed for the characterization of dye synthesized solar cells (DSSC). The timescales for transport processes in organic polymer solar cells are several orders of magnitude lower than for DSSCs. It is, therefore, not possible to study electron transport processes of organic polymer solar cells with the used setup, even with a maximum frequency of the potentiostat of 1 MHz.

In addition to the IMVS and IMPS measurements, it is possible to measure the monochromatic light dependence of the open–circuit voltage. As the absorption strength at a particular excitation wavelength can vary for different solar cell configurations and materials, it is useful to write the light intensities in terms of so–called sun–equivalents (Sun eq.). Sun–equivalent is defined as the monochromatic light intensity that would arise the same open–circuit voltage as an equivalent AM1.5 spectrum at a solar–simulator (see chapter 4.1.2).

4.1.8 Magneto–optical–experiment

Magnetic field effects on the photoluminescence of organic semiconducters were carried out in a magneto-optical experimental setup. The centerpiece of such a setup is the Physical Property Measurement System (PPMS) Dynacool type from *Quantum Designs*. The PPMS Dynacool is equipped with a single two-stage pulse tube cooler for cooling both the temper-

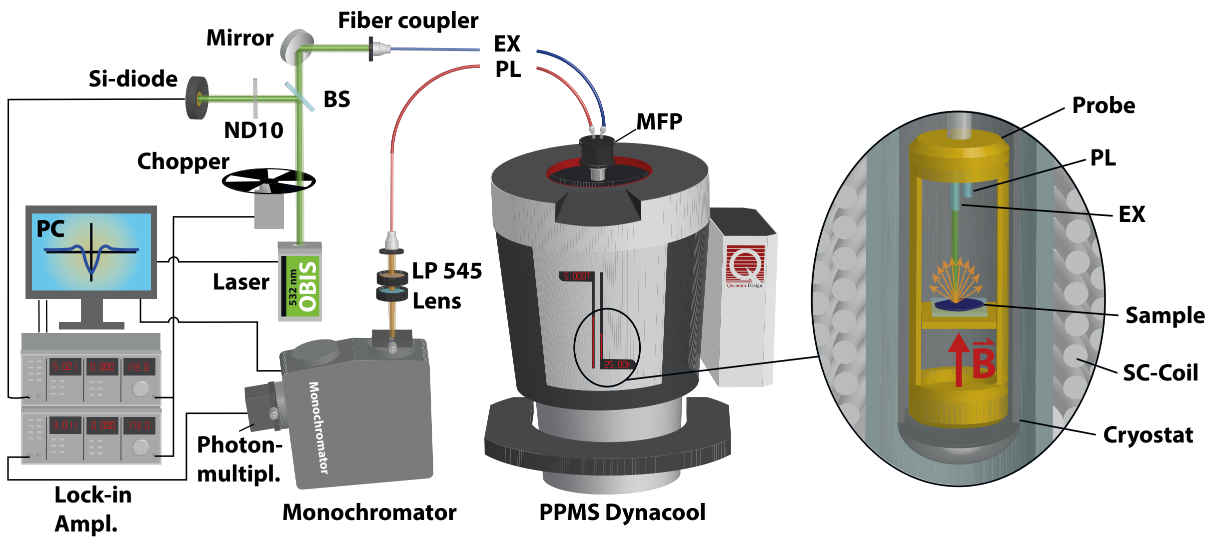

Figure 4.3: Schematic representation of the magneto–optical experimental setup. Laser excitation (EX) and photoluminescence (PL) detection paths on the left side of the PPMS. The oval shaped inset on the right hand side shows the multi–function–probe (MFP) with the sample placed in the center.

ature control system and the superconducting magnet. The cryostat offers a temperature range from 1.8 K to 400 K. The electromagnet made of superconducting material delivers a field strength of up to ±9 T. A more detailed description of the PPMS Dynacool system can be found on the product website [81].

A schematic representation of the complete experimental setup is shown in Fig. 4.3. The setup can be split into two parts: the excitation (EX) and the photoluminescence (PL) path. The excitation path starts with an OBIS 532 nm laser diode with variable output power from *Coherent*. The laser beam passes a chopper–wheel connected to two lock–in amplifiers (SR830) from *Stanford Research*. A 1 mm glass microscope slide is used as a beam–splitter, and directs a tiny portion of laser light through a neutral density filter (ND10) onto a Si–diode, which is connected to a lock-in amplifier and acts as a reference signal. The excitation laser light is then coupled, into a single–mode optical fiber with good transparency in the UV spectral region. The optical fiber guides the light to the so–called multi function probe (MFP). The MFP is directly offered by *Quantum Design* in the „A–Type, Photoconductivity Variant“. This MFP includes two 1 mm core diameter optical fibers running down from the top plate to the sample mounting stage for material excitation and spectroscopy. The organic semiconductor, dissolved in chlorobenzene, is pre–drop cast onto a 15 × 15 mm microscope slide with a thickness of 1 mm. It is positioned horizontally, with the semiconducting material facing upwards, mounted in the center of the sample probe. Exciting the sample material leads to a photoluminescence light, which is then collected with the spectroscopy optical fiber and guided internally back to the top plate of the MFP. The PL detection path starts with a single–mode optical fiber with good near IR transparency, which is connected to the spectroscopy output on the top plate of the MFP. A fiber port collimator (Thorlabs) at the end of the fiber is used to create a collimated PL beam. The beam passes a 545 nm long pass filter (LP 545) to avoid reflacted laser light from the sample. A 170 mm collecting lens is focuses the light through the entrance slit of the monochromator (*Acton* SpectraPro 2300i). The optical output of the monochromator is equipped with a photon multiplier, that is connected to a lock–in amplifier. All components of the magneto–optical setup were controlled and read out via a custom data acquisition software written in *LabView*.

4.1.9 Sheet–resistance measurements

The sheet resistance of the transparent electrodes was measured with the so–called four–probe method. A plug–and–play four–probe setup from *Signatone Corp.* in combination with a *Keithley* 2400 was used to determine the sheet resistance.

4.1.10 Atomic force microscopy AFM

An atomic force microscope (AFM) from *Bruker* Innova was used to study the surface profile of the transparent electrodes of the individual substrates used within this work. For further information on AFM techniques, the reader is referred to [82].

4.1.11 Maximum power point tracker

To study the steady–state stability of the OSCs, the encapsulated cells can be measured with a so–called maximum power point tracker (MPP–tracker). A MPP–tracker is basically a solar–simulator (section 4.1.2) with an additional control unit (*LabView*) that tracks the MPP with an iterative algorithm as a function of time. An *ATLAS* solar simulator (SoTest 1200) was used with an AM 1.5 solar spectrum under $100\,\mathrm{mW}\cdot\mathrm{cm}^{-2}$ illumination intensity. A ventilation system was used to keep the temperature of the solar cells close to the room temperature. The self written *LabView* program collects PCE of the solar cell.

4.2 Device fabrication methods

In this section, the methods used for sample preparation are explained in more detail.

4.2.1 Spin coating

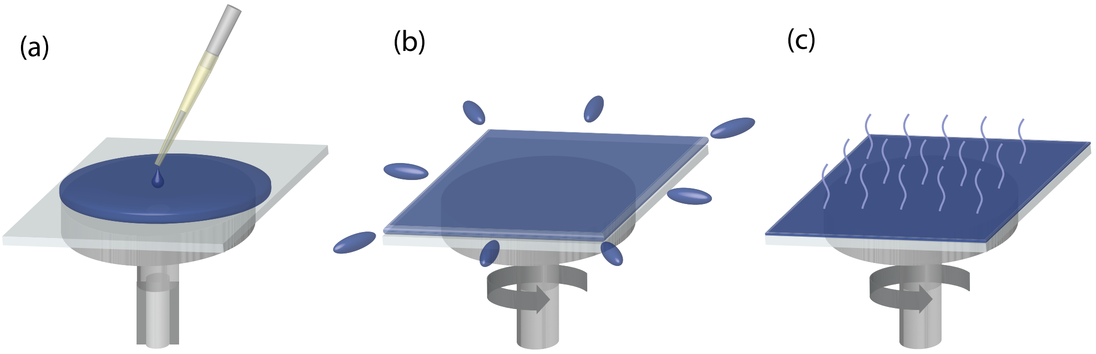

Figure 4.4: Schematic of spin coat technique. (a) Material deposition (b) Spin-off (c) Evaporation

Spin coating is one of the most common techniques for the production of OSCs on a laboratory scale. This is a procedure used to deposit a uniform thin film onto flat substrates. A schematic of the procedure is shown in Fig. 4.4. Therefore, a small amount of coating material is applied to the centre of the substrate (a). Usually, the substrate is held by the spin coater via a vacuum pump on the rotating stage. The substrate is then rotated at high speed in order to spread the coating material on the sample surface by centrifugal force. A high spin speed leads to a thin layer and vice versa. The excess material is spun away from the sample, which can be seen in (b). In the last stage of the spin coating process, the remaining solvent evaporates out of the film (c). With this technique, layer thicknesses from a few nanometres up to several micrometres can be achieved.

4.2.2 Vacuum deposition

Physical vapour deposition or thermal evaporation is an established method to deposit thin metal and metal oxide layers on a substrate. Fig. 4.5 shows a schematic representation of a vacuum deposition setup. In the deposition process operated at high vaccuum (a) ($p < 10^{-5}\,\mathrm{mbar} = 10^{-3}\,\mathrm{Pa}$), the substance to be evaporated is heated to its boiling temperature or sublimation temperature in a suitable container (b) (ceramic crucible, tungsten boat e.g.). The resulting material steam condensing on the substrate (c) finally forms an extremely homogeneous layer, which can range from a thickness of one atom up to millimetres. Usually a rotating shadow mask (d) is used to pattern the coating of the material on the substrate.

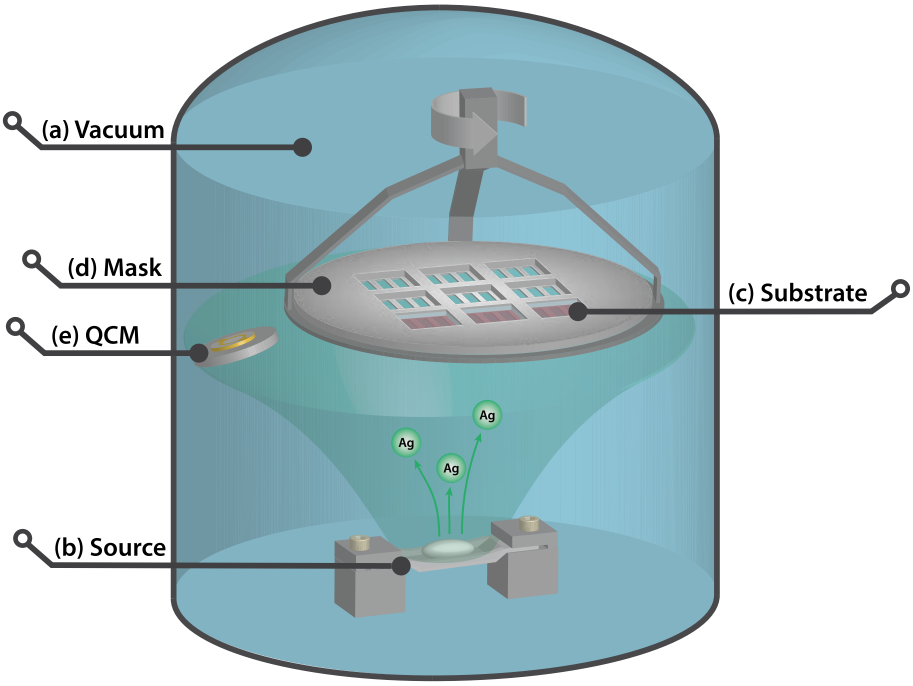

Figure 4.5: Schematic representation of the vacuum deposition method. (a) High vacuum pressure ($p < 10^{-5}$ mbar $= 10^{-3}$ Pa). (b) Material source in tungsten boat. (c) Substrate. (d) Evaporation mask. (e) Quartz crystal microbalance (QCM).

Quartz crystal microbalance (QCM) (e) or optical density (OD) measurements are commonly used for monitoring the thickness and homogeneity during the vapour deposition process.

4.3 Rigid organic solar cell device fabrication

All rigid non–fullerene and fullerene OSCs, within this work, were fabricated with the inverted device architecture ITO/ZnO/BHJ/MoO_x/Ag. Fig. 4.6 illustrates the different intermediate processing steps during device fabrication. The 25.4 × 25.4 mm pre–patterned ITO glass substrates (a) with a sheet–resistance of 15 Ω□, were purchased from Xin Yan Technology LTD. The sheet–resistance of the electrode was measured with a four–wire probe measurement. The specifications of the substrate are shown in Fig. 4.7(a,b). At first, the ITO substrates were wiped with a microfiber cloth soaked in toluene and successively cleaned in an ultrasonic bath with acetone and isopropyl alcohol for 10 min. Second, the substrates were treated in an ultraviolet–ozone chamber for 5 min at 50 W. A 90 nm Ag herringbone back–contact (b) was evaporated with the selfmade mask shown in Fig. 4.7(e). The ZnO precursor sol–gel solution was prepared by dissolving 1 g of zinc acetate dihydrate ($Zn(CH_3COO)_2{\cdot}H_2O$) in 10 ml of 2-methoxyethanol ($CH_3OCH_2CH_2OH$), and 0.28 g of ethanolamine (EA) ($NH_2CH_2CH_2OH$) was subsequently added as a sol–gel stabilizer to

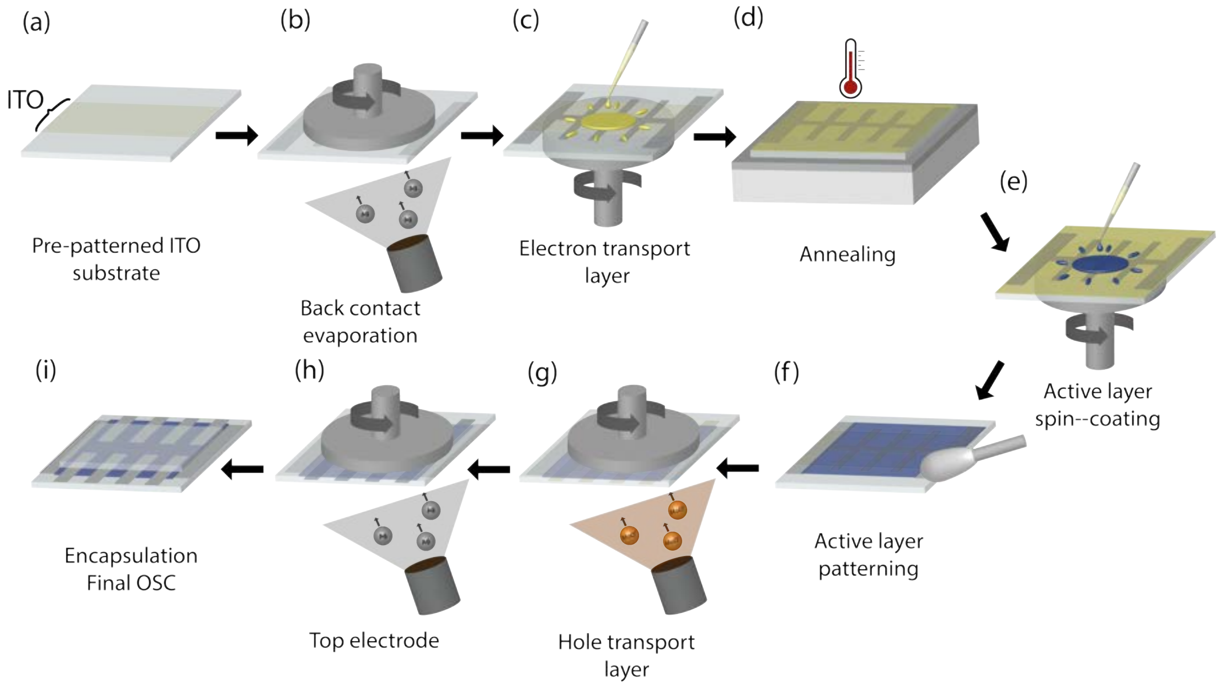

Figure 4.6: Schematic representation of the processing steps for OSCs. (a) Glass substrate with a pre–patterned indium tin oxide electrode. (b) Ag back contact evaporation. (c) Electron transport layer (ETL) spincoating. (d) ETL annealing step 155° for 15 min. (e) Active layer spin coating. (f) The active layer is then patterned with an eartip and toluene. (f) MoO_x hole transport layer vacuum deposition. (g) Silver top electrode vacuum deposition. (h) Encapsulation and final OSC.

the solution keeping the molar ratio of ($Zn(CH_3COO)_2 \cdot H_2O$) to EA at 1.0. The resulting solution was then stirred overnight at room temperature. The slightly yellowish ZnO sol–gel solution was spin–coated onto the ITO substrates Fig. 4.6(c) at 2000 rpm for 45 sec to obtain a film thickness of approximately 30 nm. After annealing the ZnO layer (d) for 15 min at 155 °C, the substrates were transferred into a nitrogen–filled glove box.

The **PBDB-T-2F:IT4F** active layer materials in a 1 : 1 (w/w) ratio were dissolved in a chlorobenzene (CB):1,8-diiodooctane (DIO) (99.5:0.5 volume ratio) solution with a total concentration of 20 mg/ml. DIO was purchased from Sigma–Aldrich and used without further purification. The fullerene **PBDB-T-2F:PC71BM** reference solar cells, were prepared with a total concentration of 15 mg/ml, and a 1:1 (w/w) ratio in a CB solution. The **PBDB-T-2F:EH-IDTBR** blend solution was prepared with a 1 : 2.5 (w/w) ratio with a total concentration of 24 mg/ml dissolved in CB solution. The solutions were stirred at least for 4 hours at 65 °C and 500 rpm in a nitrogen–filled glove box.

The **PTB7-Th:EH-IDTBR** non–fullerene OSCs were fabricated by dissolving the materials with 1:2.5 (w/w) ratio in CB with a total concentration of 24 mg/ml. **PTB7-Th:PC71BM** fullerene blends were prepared with a 1:1.5 (w/w) ratio in CB with a total concentration of 24 mg/ml. **PTB7-Th:IT4F** cells were prepared by dissolving the pristine materials with a $1:1$ (w/w) weight ratio in CB at a total concentration of 24 mg/ml. The solutions were stirred overnight at 60 °C and 500 rpm in a nitrogen–filled glove box.

The resulting dark blue solutions were cooled till room temperature and spin–coated inside the glove box onto the ZnO layer at 1500 rpm for 2 sec followed by 4000 rpm for 20 sec to obtain an active layer thickness of approximately 100 nm (cf. Fig. 4.6(e)). The thickness of the active–layer was measured with a DekTak profilometer (see section 4.1.3). Both fullerene and non–fullerene films were not thermally annealed. The active layer material was then carefully removed at the position of the top– and back–contact with an eartip and toluene (f).

The device fabrication was completed by thermally evaporating a 10 nm–thick MoO_x HTL–layer (g) and a 100 nm–thick silver top electrode (h) under vacuum at a pressure of 1×10^{-5} Pa. The resulting active layer thickness of the individual solar cell pixels was 10 mm^2. Finally, the active–area was encapsulated inside the glove box (i), with a glass plate and epoxy–glue (EMCAST 1500) to shield the active material from oxygen.

It is common to compare the blend solar cells to the donor–only and acceptor–only devices. Therefore, the neat **PBDB–T–2F** and **PTB7–Th** materials were dissolved in CB with a total concentration of 10 mg/ml. However, the material morphology is different for pristine and blend materials. In the blend, the small molecule acceptors are dispersed in the matrix of the polymer, while in the pristine film the molecules are closely packed, and potentially leading to strong aggregation and bad film quality. While this is no problem for pristine polymer films, it is not trivial for the small molecule acceptors IT4F and EH–IDTBR. In order to get a better film quality the **IT4F** and **EH–IDTBR** acceptors were blended with the insulting polymer polystyrene (PS) in a $1:1$ (w/w) ratio at a total concentration of 20 mg/ml.

4.3.1 Device fabrication for magneto–optical experiments

All samples for the magneto–optical characterization were prepared by dissolving the materials in CB. The concentration for all blend configurations was 20 mg/ml and 10 mg/ml for the neat materials.

The w/w ratio of the donor:acceptor blends was set in the same way as for solar cell preperation. In addition to that, a $1:0.1w/w$ ratio was prepared for all blends, to test the magnetic field effects below the percolation threshold of the BHJ.

The solutions were then drop–casted onto a 15×15 mm microscope glass slide and dried in the GB.

4.4 Flexible organic solar cell device fabrication

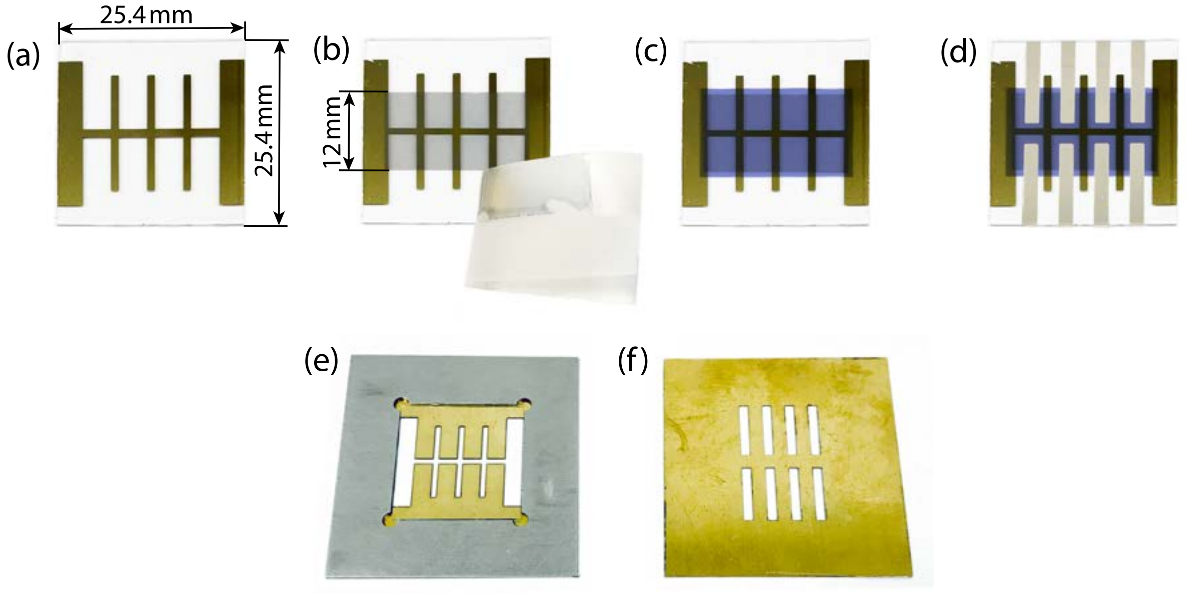

Figure 4.7: Intermediate steps during device fabrication. (a) Flexible substrate on solid support with Cr/Au back–contact. (b) PEDOT:PSS PH1000 patterning with *3M* scotch tape. (c) Spin–coated low–conductive PEDOT:PSS and active layer. (d) Evaporated Al top–contact. (e-f) Selfmade evaportation masks for back– and top–contact.

Flexible OSCs were fabricated to demonstrate the tremendous applicability and processibility of organic semiconductors. Therefore, the solar cell parameters were studied for three different types of flexible substrates.

4.4.1 Ultrathin ITO–free flexible PH1000–PET substrate

Ultrathin ITO–free flexible OSCs were fabricated based on a 1.4 μm thick PET foil (*Mylar* 1.4 CW02). The substrate preparation procedure is based on the original published protocol from Martin Kaltenbrunner et al. [83].

The fabrication of such ultrathin flexible OSCs requires a special preperation of the substrates in order to use common processing techniques such as spin coating and vacuum evaporation. Therefore, the PET foil was transfered onto a solid supporting substrate. In this work, a 25.4 × 25.4 mm microscope glass slide was used as the solid support. The glass substrates were thoroughly cleaned with toluene, and a microfiber cloth, acetone and isopropanol in an ultrasonic bath sequentially for 10 min. In order to reversible attache the PET foil to the solid support, polydimethylsiloxane (PDMS) (*Sylgard* 184 Silicone Elastomer) was used as a thin adhesive layer. The PDMS mixture was prepared by mixing 3 g silicon elastomer base with 0.3 g curing agent in 3.3 g of n–Hexane. A glass rod was used to stirr the mixture until it appeared homogenous. The freshly prepared PDMS mixture was than deposit onto the solid substrate using a syringe with a 0.45 μm PTFE filter. The substrate was then spun with the spin–coater at 4000 rpm for 60 s. Right after spin–coating the samples were put on a heating plate for 10 min at 150 °C to cross–link the PDMS film. During the heat–treatment the substrates were covered with a large glass beaker to avoid dust particles on the surface of the substrate. After the preparation of the adhesive PDMS layer, the PET foil was laminated onto the solid support and the protruding residues of the PET foil were ripped off the edges of the glass support. The laminated PET foil adheres through weak van der Waals forces to the PDMS. Directly after the lamination of the PET foil, the substrates were placed onto a heating plate for 10 min at 110 °C to remove access gas under the foil. No ultraviolet–ozone treatment was performed for any flexible substrate.

A 90 nm Au back–contact was evaporated onto the flexible substrates with the mask shown in Fig. 4.7(e). The attachment of the Au back–contact to the PET foil is enhanced with an evaporated 10 nm thick CrO_3 interlayerlayer. A transparent electrode was fabricated from a stock conducting polymer poly(3,4–ethylenedioxythiophene):polystyrene sulphonate (PEDOT:PSS) from *Clevios* PH1000 with 5 vol% dimethylsulphoxide (DMSO) and 0.7 vol% Zonyl FS–300 fluorosurfactant *Fluka*. The solution was mixed vigorously with a magnetic stirrer over night and stored in the fridge for later use. The solution was transfered onto the substrate with a syringe and a *Minisart* RC hydrophilic 0.45 μm filter. The substrate was then spun at 1500 rpm for 45 s and subsequently dried at 122 °C for a few seconds. The PEDOT:PSS PH1000 film was then patterned by applying a *3M* scotch tape at the places to be removed, and then carefully pealing of the tape (cf. Fig. 4.7(b)). The transparent electrode was patterned resulting in the same sizes as for the rigid ITO substrated shown in Fig. 4.7(a). The substrates were then annealed at 122 °C for 15 min. The conductivity of the PEDOT:PSS PH1000 can be significantly improved by simple film treatment with isopropanol [68]. Therefore, the PEDOT:PSS PH1000 film is washed by spin coating 400 μL isopropanol at 2000 rpm for 2 s followed by 4000 rpm for 10 s from the surface. The substrate is then annealed again at 122 °C for 15 min.

As the PEDOT:PSS PH1000 transparent electrode is hole charge carrier selective, the solar cells were fabricated in the so–called standard configuration. A schematic representation of the solar cell configuration is shown in Fig. 4.8(a) [84]. A low–conductive (LC) PEDOT:PSS (*Clevios* P VP 4083) was filtered thru a 0.45 μm filter and spin–coated with 3000 rpm for 30 s onto the transparent electrode to form a uniform hole–transport–layer (HTL). The low–conductive PEDOT:PSS layer is used to increase the work–function of the PEDOT:PSS PH1000 towards the HOMO energy level of the polymers. An energy level alignment diagram is shown in Fig. 4.8. The samples were then transfered into a nitrogen filled glove box.

The active layers PBDB–T–2f:IT4F 1:1 (w/w) ratio were prepared in the same way as for

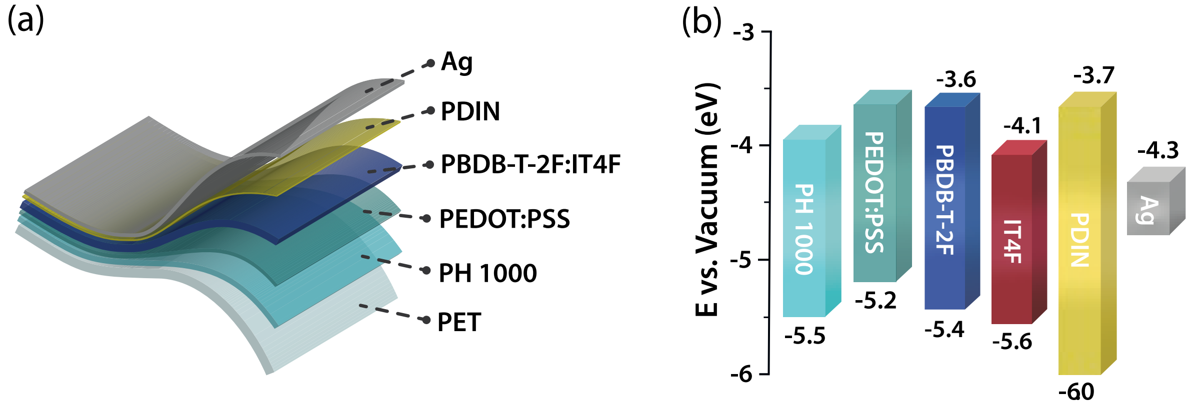

Figure 4.8: (a) Device architecture of the flexible ITO–free PET OSC in the standard configuration. (b) Energy levels of the device components.

the rigid OSCs presented in section 4.3. Subsequently, a perylene diimide with amino as the terminal substituent (PDIN), dissolved in methanol at a concentration of (1.5 mg/ml), was spin–coated onto the active layer at 5000 rpm for 30 s. Finally, the solar cell was completed by thermally evaporating a 100 nm Ag top–contact with the mask–shown in Fig. 4.7(f). The cells were stored under dark conditions, inside a nitrogen filled glove box until further use.

4.4.2 Ultrathin ITO–PI flexible substrate

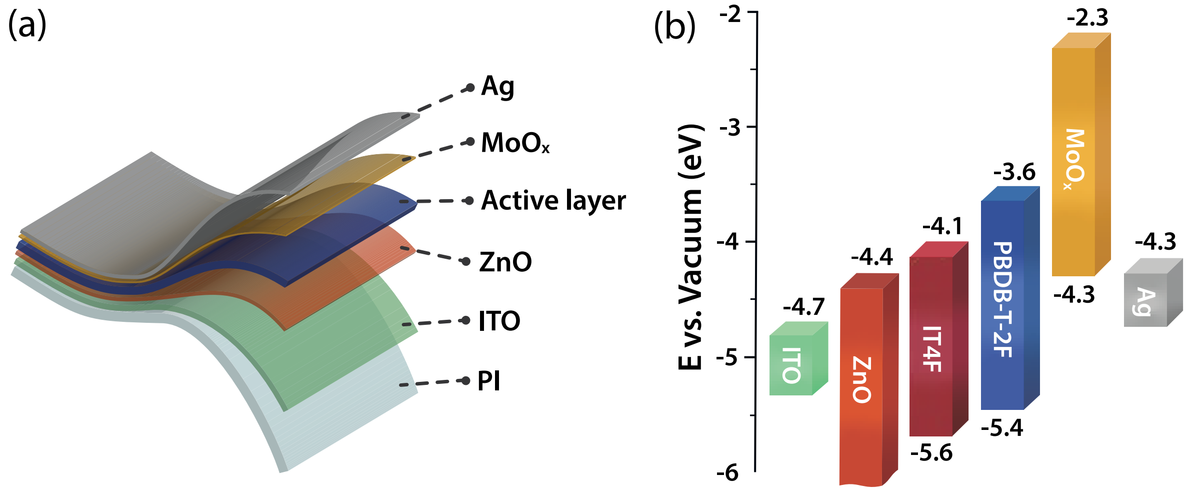

Figure 4.9: (a) Device architecture of the flexible PI OSC in the inverted configuration. (b) Energy levels of the device components.

The group of Takao Someya provided a 1.3 μm thick transparent polyimide (PI) foil with a 100 nm sputtered ITO transparent electrode on top [85]. The transparent electrode has a sheet–resistance of 7 Ω□. The sheet–resistance of the electrode was determined with a four–wire probe measurement (see section 4.1.9). The thin PI substrate was already laminated onto a 25.4 × 25.4 mm solid support glass, and was used as received. The flexible substrate was carefully cleaned by rinsing the surface with isopropanol and subsequently dried in a nitrogen air–flow. A 90 nm Ag back–contact was evaporated onto the flexible substrate with the mask shown in Fig. 4.7(e).

The flexible OSCs were fabricated with the inverted cell configuration ITO/ZnO/BHJ/MoO_x/Ag.The solar cell was then fabricated by following the same procedure as presented in section 4.3 and Fig. 4.6. The cells were stored inside the nitrogen filled glove box under dark conditions.

4.4.3 Flexible PEN Ag nanowire/graphene substrate

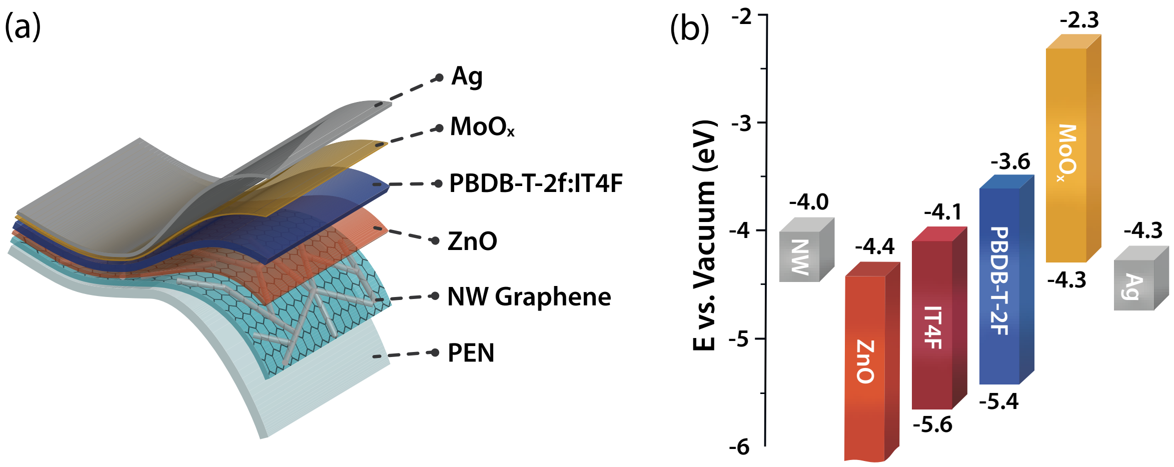

Figure 4.10: (a) Device architecture of the flexible PEN OSC based in Ag nanowire/graphen electrode in the inverted cell configuration. (b) Energy levels of the device components.

A 125 μm thick flexible PEN substrate with a Ag nanowire:graphene transparent electrode was provided by the group of Kim Wonjae from VTT institute Finland. The flexibel PEN substrates were transfered to a 25.4 × 25.4 mm solid microscope glass substrate with the same procedure as for the ITO free PET substrates presented above. A sheet–resistance of 25 Ω□ was determined for the transparent NW–graphene electrode (see section 4.1.9).

The OSCs were fabricated in the inverted cell configuration NW–graphene/ZnO/BHJ/MoO_x/Ag in the same way as for the rigid IT–Glass substrates presented in section 4.3 and Fig. 4.6. A schematic representation of the solar cell layers is shown in Fig. 4.10(a). The energy levels of the device components are presented in Fig. 4.10(b).

4.4.4 Delamination technique

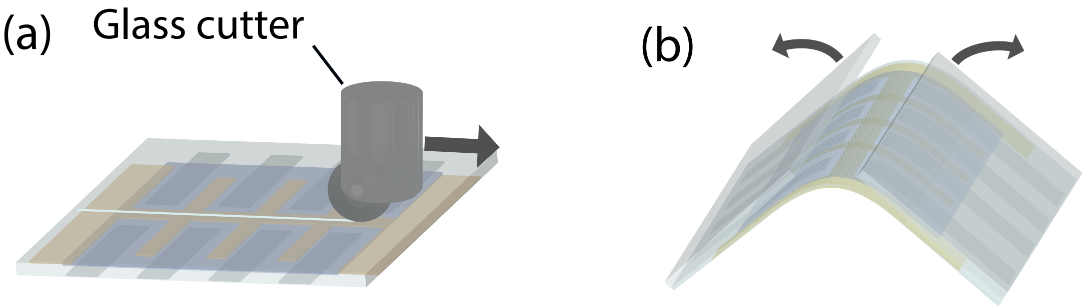

Figure 4.11: Delamination of the flexible substrate from the solid support. (a) Scratching the glass in the middle of the cell at the back with a diamond glass cutter. (b) The broken glass halves are carefully torn apart.

To detach the flexible substrate from the solid support, the back of the glass is scratched with a glass cutter in the middle of the cell. The glass is then carefully cracked, and the two glass halves can be easily peeled off the flexible substrate. A schematic representation of this technique is shown in Fig. 4.11.

5 Results and discussion

In this chapter the obtained measurement results are shown an discussed.

5.1 Materials and absorption spectra

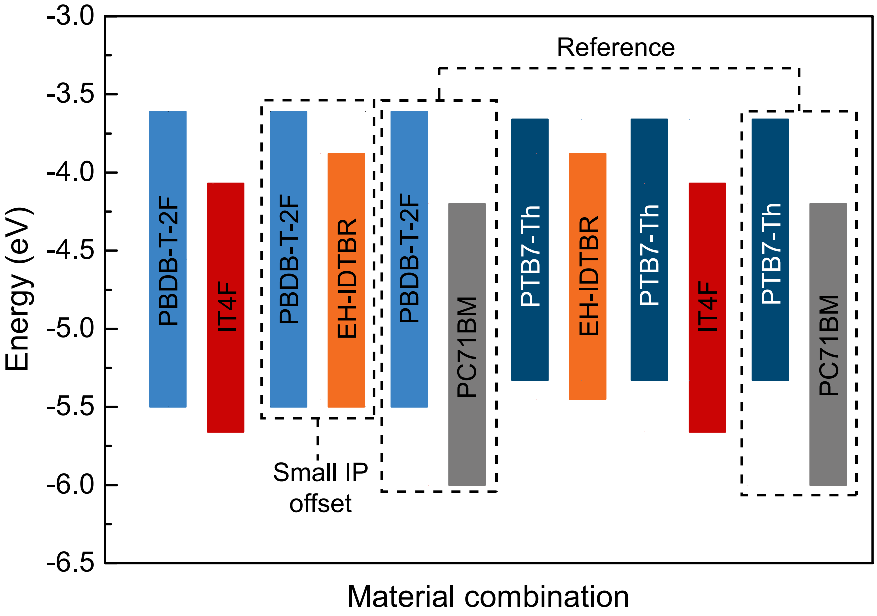

Figure 5.1: Energy levels for the studied material combinations. Values were taken from [71, 75, 78, 86].

The energetic HOMO and LUMO levels of the studied material combinations (see section 3) are schematically depicted in Fig. 5.1. All shown values were taken from [71, 75, 78, 86] and were estimated from cyclic–voltammetry measurements. Apart from the donor–PC71BM blends, which were used here as a state–of–the–art fullerene reference, the energetic difference of the ionization potential (IP) is small ($< 0.3\,\mathrm{eV}$) in all other cases. The electron affinity (EA) is greater than 0.3 eV in all combinations except for PTB7–Th:EH–IDTBR. A detailed analysis of the shown materials combinations is given in the following sections. The colors of the shown energy levels, as well as the depicted curves in the measurement graphs, were chosen that all cells containing IT4F are red–squares, all cells with EH–IDTBR are represented with orange–down triangles, and PC71BM cells are marked with gray–up triangles.

The efficiency of a solar cell is always accompanied by an effective absorption of the incident light in the active layer material of the cell. Optimizing the absorption is therefore

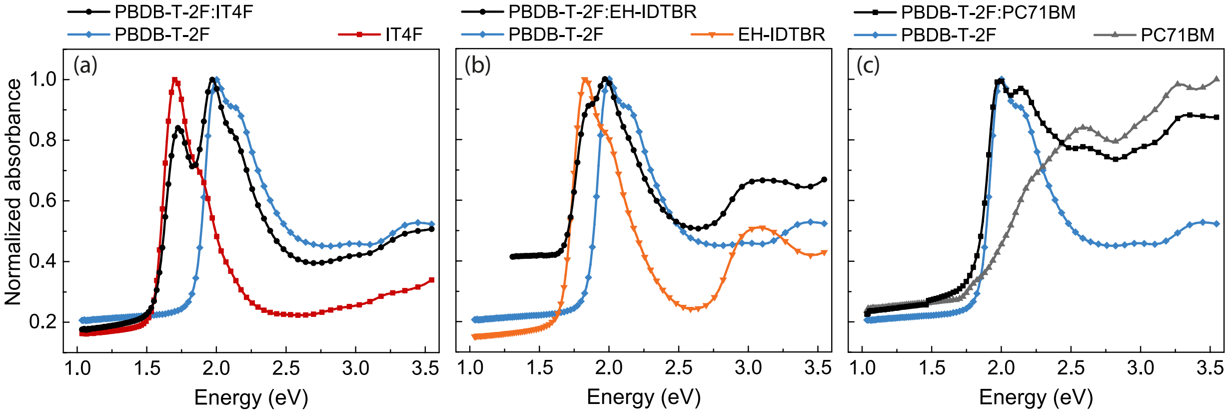

Figure 5.2: Normalized UV–Vis absorbance spectra of the PBDB–T–2F:acceptor thin films and the neat donor and acceptors. (a) PBDB–T–2F:IT4F 1:1 (w/w) (b) PBDB–T–2F:EH–IDTBR 1:2.5 (w/w) (c) PBDB–T–2F:PC71BM 1:1 (w/w).

important towards efficient solar cells. The ultraviolet–visible (UV–Vis) normalized absorption measurements of the PBDB–T–2F:acceptor blend and the neat blend components were performed with a *PerkinElmer* spectrometer as described in the method section (see 4.1.1). The normalized absorption spectra for the PBDB–T–2F:IT4F 1:1 (w/w) OSC materials are shown in Fig. 5.2(a). The figure shows two distinct peaks of the individual components and the spectrum of the blend film (black–circles) as a function of photon energy. The PBDB–T–2F polymer (blue–diamonds) has an absorption band from $\sim$ 1.75 eV to $\sim$ 2.6 eV with a peak at 2.0 eV and a shoulder at 2.15 eV. In the blend absorbance this peak slightly shifts towards lower energies. The IT4F acceptor (red–squares) absorption band ranges from $\sim$ 1.5 eV to $\sim$ 2.4 eV, and has a peak at 1.7 eV and a shoulder at 1.9 eV. By comparing the donor and acceptor's onset energies, it can be seen that the onset of the IT4F acceptor (red squares) is of lower energy than for the PBDB–T–2F donor making IT4F the so–called narrow–gap absorber of the blend.

Fig. 5.2(b) presents the results for the PBDB–T–2F:EH–IDTBR 1:2.5 (w/w) non–fullerne blend (black–circles). Compared to the IT4F acceptor in Fig. 5.2(a), the EH–IDTBR acceptor (orange down–triangles) has a slightly higher energetic absorption band from $\sim$ 1.6 eV to $\sim$ 2.6 eV with a peak at 1.83 eV and a shoulder at 2.0 eV. Again, in this blend the accpetor is the narrow–gap absorber.

The PBDB–T–2F:PC71BM 1:1 (w/w) blend (black–circles) film and neat components are shown in Fig. 5.2(c). The polymer–fullerene blend shows good complementary absorption properties covering the whole UV–Vis region. The PC71BM absorption band (gray–up–triangles) is mainly located in the high energy regime which onsets at $\sim$ 1.7 eV. The blend absorption sums up to a broad absorption band from $\sim$ 1.7 eV till the UV–spectral region.

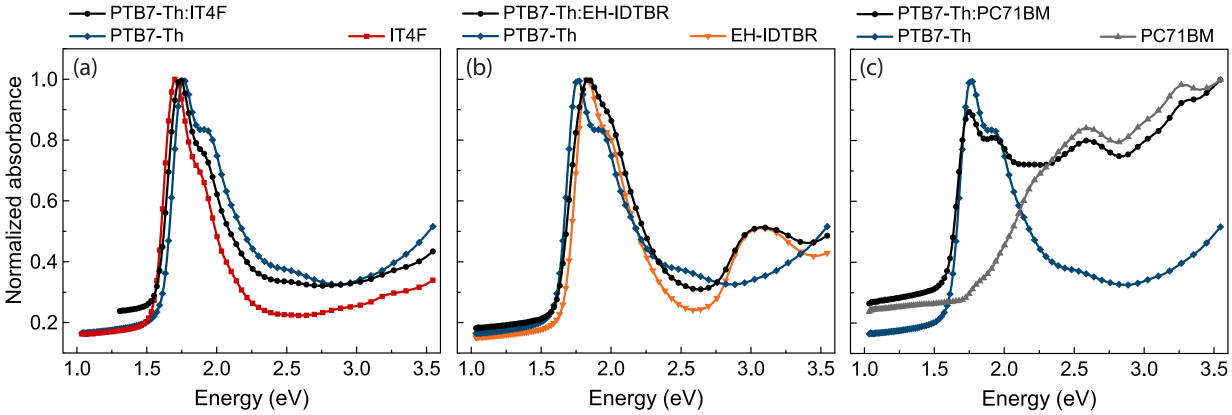

Figure 5.3: Normalized UV–Vis absorbance spectra of the PTB7–Th:acceptor thin films and the neat donor and acceptors. (a) PTB7-Th:IT4F 1:1 (w/w) (b) PTB7–Th:EH–IDTBR 1:2.5 (w/w) (c) PTB7-Th:PC71BM 1:1 (w/w).

The normalized absorption spectra as a function of photon energy of the PTB7-Th:acceptor based solar cells are depicted in Fig. 5.3. The PTB7–Th polymer was investigated with the IT4F acceptor in a 1:1 (w/w) blend configuration. The corresponding normalized absorbance spectra are shown in Fig. 5.3(a). The main absorption band of the PTB7-Th polymer (dark blue–diamonds) ranges from ~ 1.55 eV to ~ 2.5 eV and has a peak at 1.76 eV with a shoulder at ~ 1.93 eV. With the IT4F acceptor (red–squares) the blend absorption band (black–circles) ranges from ~ 1.55 eV to ~ 2.3 eV with a peak and a shoulder similar to the neat components.

The PTB7–Th:EH–IDTBR 1:2.5 (w/w) blend (black–circles) and the components are shown in Fig. 5.3(b). The absorption band of the EH–IDTBR acceptor (orange down–triangles) is spectrally compareable to the polymer band and shows a peak at 1.83 eV with a small shoulder at ~ 2.0 eV. The onset energy of the acceptor is higher than for the donor making the polymer the narrow–gap absorber of the blend.

Fig. 5.3(c) shows the absorption measurements for the fullerene reference PTB7-Th:PC71BM 1:1 (w/w) (black–circles). The blend film mainly covers the UV–Vis spectral region which is essential for high photocurrent generation.

5.2 Device characterization

5.2.1 Current–density $j(V)$ measurements

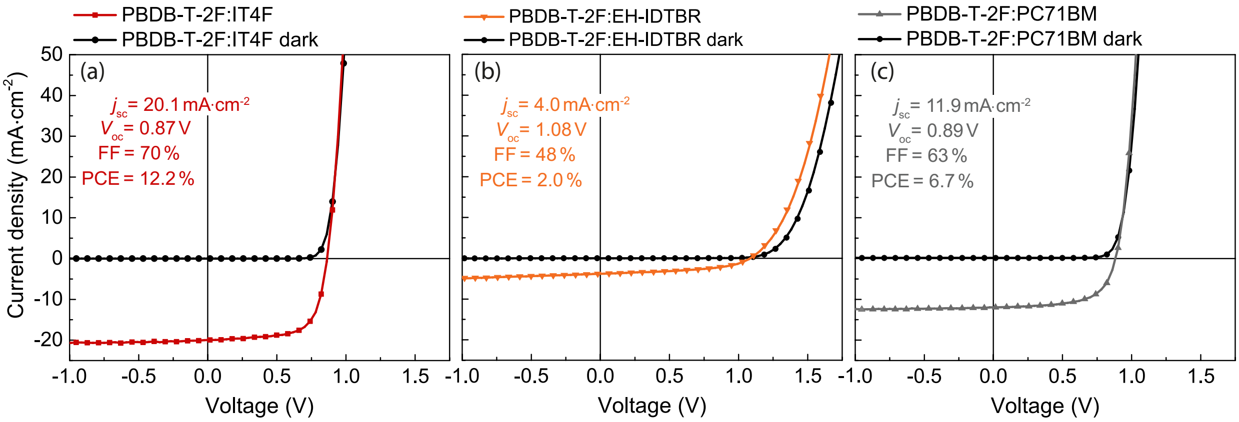

Figure 5.4: $j(V)$–curves for PBDB-T-2F:acceptor OSCs under simulated $100\,\mathrm{mW}\cdot\mathrm{cm}^{-2}$ AM1.5 solar illumination and under dark conditions for (a) PBDB–T–2F:IT4F, (b) PBDB–T–2F:EH–IDTBR, and (c) PBDB–T–2F:PC71BM.

To investigate the perfomance differences that arise due to different acceptor materials in the active layer of the OSC, current density versus voltage $j(V)$–curves were measured for all types of material combinations. The solar cell device fabrication is discussed in section 4.3. All $j(V)$–curves within this work were measured with a solar–simulator (see section 4.1.2) along with an 1 Sun AM1.5 spectrum, as well as under dark conditions. The intensity of the solar spectrum was calibrated with a certified standard silicon solar cell at $100\,\mathrm{mW}\cdot\mathrm{cm}^{-2}$.

The $j(V)$–curves for the OSCs based on the PBDB-T-2F:acceptor blends are shown in Fig. 5.4, and the corresponding solar–cell parameters are written in the plots and collected in Tab. 1. The number of plotted points has been reduced to simplify the diagram. The PBDB–T–2F:IT4F device, shown in Fig. 5.4(a) and represented by the red–squares curve, has an open–circuit voltage $V_{\mathrm{oc}} = 0.86\,\mathrm{V}$, a short–circuit current $j_{\mathrm{sc}} = 20.1\,\mathrm{mA}\cdot\mathrm{cm}^{-2}$, and a fill factor $\mathrm{FF} = 70\,\%$, which results in a power conversion efficiency $\mathrm{PCE} = 12.2\,\%$. The obtained cell parameters are compareable to the literature values [71]. The black (circles) curves depicts the $j(V)$–curve under dark conditions.

The $j(V)$–curve for the solar cell devive based on the PBDB–T–2F donor polymer in combination with the EH–IDTBR non–fullerene acceptor is plotted in Fig. 5.4(b) and marked by orange down–triangles. The solar cell exhibits a lower short–circuit current $j_{\mathrm{sc}} = 4.0\,\mathrm{mA}\cdot\mathrm{cm}^{-2}$ compared to the IT4F acceptor. The lowered j_{sc} can be attributed to the zero IP offset of the blend materials. An IP $< 0.1\,\mathrm{eV}$ leads to a lower driving force for exciton dissociation and consequently, a lower photocurrent generation. Conversely, due to the minimized IP offset, the open–circuit voltage is comparatively higher $V_{\mathrm{oc}} = 1.08\,\mathrm{V}$. Due to parasitic resistances, the fill factor of the solar cell results in a low value FF= 48 %, which can be seen at the slope of the curve at V_{oc} and j_{sc} (compare Fig. 2.6). The resulting solar cell shows the lowest power conversion efficency PCE= 2.0 % as compared to the other donor–acceptor blends.

Fig. 5.4(c) shows the $j(V)$–curve of the PBDB–T–2F:PC71BM fullerene reference device. The $V_{\mathrm{oc}} = 0.89\,\mathrm{V}$ and FF= 63 %a are comparable to the IT4F non–fullerene device depicted in (a). However, the short–circuit current $j_{\mathrm{sc}} = 11.9\,\mathrm{mA \cdot cm^{-2}}$ is substantially lower than with IT4F. The resulting PCE= 6.7 %.

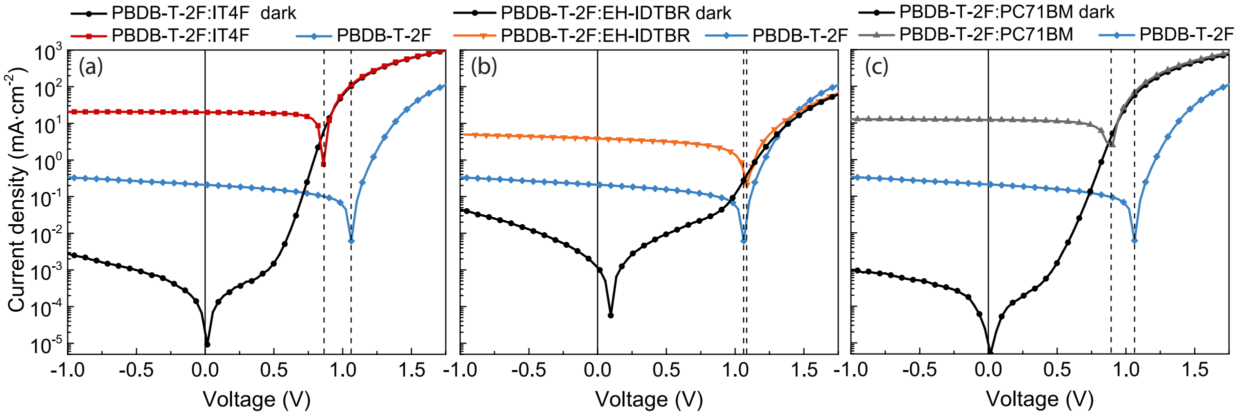

Figure 5.5: Semilogarithmic $j(V)$–curves for PBDB-T-2F:acceptor OSCs under simulated $100\,\mathrm{mW \cdot cm^{-2}}$ AM1.5 solar illumination and under dark conditions (a) PBDB–T–2F:IT4F, (b) PBDB–T–2F:EH–IDTBR, and (c) PBDB–T–2F:PC71BM. The blue (diamonds) curve shows the $j(V)$–curve for the donor–only PBDB–T–2F solar cell.

Semilogarithmic $j(V)$–curves for the same PBDB–T–2F:acceptor solar cells are plotted in Fig. 5.5. In addition to the donor–acceptor blend dark (black–circles) and simulated $100\,\mathrm{mW \cdot cm^{-2}}$ AM1.5 solar illumination $j(V)$–curves, the donor–only PBDB–T–2F device (blue–diamonds) is shown. It can be clearly seen, that photocurrent generation is significantly enhanced in donor–acceptor systems, compared to the donor–only device. In striking contrast to the PBDB–T–2F:EH–IDTBR blend shown in (b), where the V_{oc} is almost identical to those of the respective single–component devices (blue–diamonds), after the formation of the BHJ, the V_{oc} decreases of about 0.2 V for the other material combinations. The V_{oc} difference is indicated by the vertical dashed lines. By comparing the dark $j(V)$–curves it can be seen that the leakage current–density of the EH–IDTBR based device is an order of magnitude higher than for the IT4F and PC71BM blend. This can be attributed to a lower R_{p} (compare section 2.6) of the EH—IDTBR based device, and to some remaining background light during dark condition measurements.

Current density versus voltage $j(V)$–curves for the OSCs based on the PTB7-Th:acceptor

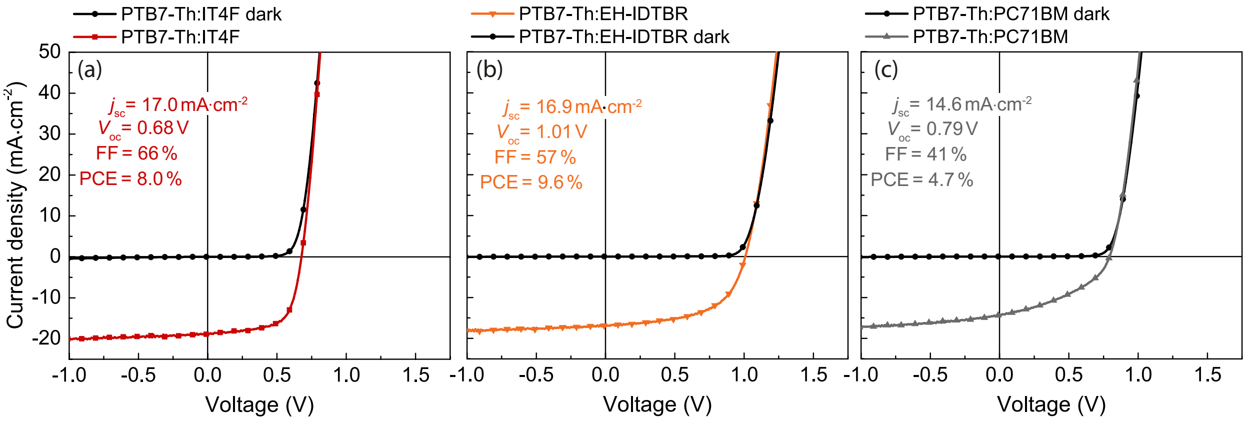

Figure 5.6: $j(V)$–curves for PTB7-Th:acceptor OSCs under simulated $100\,\mathrm{mW}\cdot\mathrm{cm}^{-2}$ AM1.5 solar illumination and under dark conditions for (a) PTB7–Th:IT4F, (b) PTB7–Th:EH–IDTBR, and (c) PTB7–Th:PC71BM.

blends are shown in Fig. 5.6, and the corresponding solar–cell parameters are written in the plots and collected in Tab. 1.
The dark and standard AM1.5 solar illumination $j(V)$–curves for the PTB7–Th:IT4F material combination are shown in Fig. 5.6(a). The cell exhibited a high $j_{\mathrm{sc}} = 17.0\,\mathrm{mA}\cdot\mathrm{cm}^{-2}$ and FF= 66 %. However, compared to all other cells, the V_{oc} loss due to the formation of the BHJ (compare Fig. 5.7) was highest for this material combination. The open–circuit voltage for this blend was $V_{\mathrm{oc}} = 1.01\,\mathrm{V}$, and the cell performance resulted in PCE= 8.0 %.

The results for the PTB7-Th:EH–IDTBR donor–acceptor combination are plotted in Fig. 5.6(b). The V_{oc} of 1.01 V is compareable to the V_{oc} measured for the PBDB-T–2F:EH–IDTBR cells (1.04 V). In contrast to the zero IP offset in the PBDB-T–2F:EH–IDTBR cells, the IP offset for the PTB7-Th:EH–IDTBR cell is 0.2 eV, which results in a suitable driving force for exciton dissociation and photocurrent generation. This yields a high $j_{\mathrm{sc}} = 16.9\,\mathrm{mA}\cdot\mathrm{cm}^{-2}$, which is compareable to the PTB7–Th:IT4F cell. The FF of 57 % is compareble to the values presented in literature [79].

The respective $j(V)$–curves for the PTB7-Th:PC71BM fullerene reference are plotted in Fig. 5.6(c). The cell yields a $j_{\mathrm{sc}} = 14.6\,\mathrm{mA}\cdot\mathrm{cm}^{-2}$, a FF= 41 % and a $V_{\mathrm{oc}} = 0.79\,\mathrm{V}$, which results in a PCE= 4.7 %. Although the j_{sc} is higher than for the PBDB-T–2F:PC71BM device, the FF and V_{oc}, and therefore, the PCE, are lower.

Fig. 5.7 shows the semilogarithmic $j(V)$–curves of the PTB7–Th:acceptor solar cells. Again, it can be seen that the photocurrent generation is significantly enhanced for donor–acceptor systems, compared to the donor–only device represented by blue–diamonds. Comparing PTB7–Th:acceptor solar cells plotted in Fig. 5.7 to the $j(V)$–curves shown in Fig. 5.5, reveals that the V_{oc} loss due to the formation of the BHJ is higher for all PTB7–Th combinations than

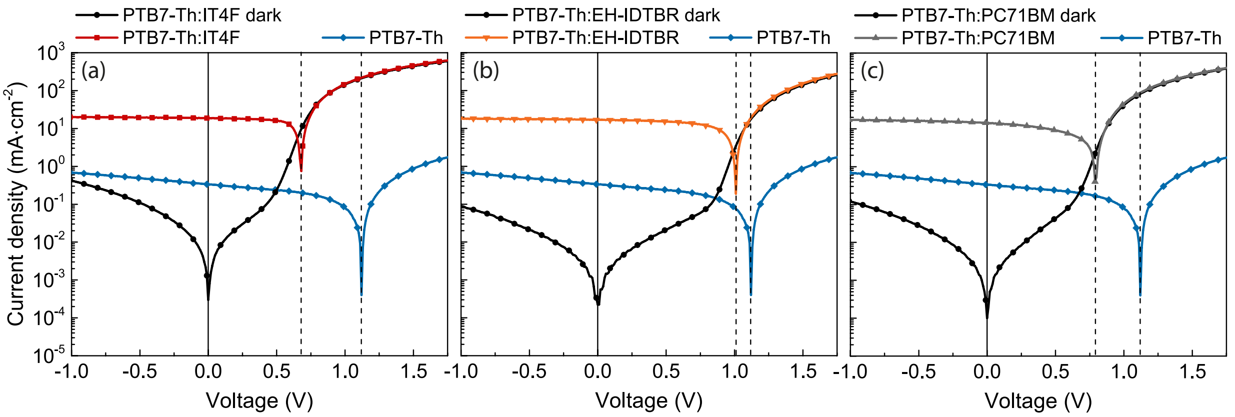

Figure 5.7: Semilogarithmic $j(V)$–curves for PBDB-T-2F:acceptor OSCs under simulated $100\,\mathrm{mW}\cdot\mathrm{cm}^{-2}$ AM1.5 solar illumination and under dark conditions (a) PTB7–Th:IT4F, (b) PTB7–Th:EH–IDTBR, and (c) PTB7–Th:PC71BM. The blue (diamonds) curve shows the $j(V)$–curve for the donor–only PTB7–Th solar cell.

for PBDB–T–2F. The V_{oc} loss of the PTB7–Th:IT4F cells was 0.43 V, the PTB7–Th:EH–IDTBR cells revealed a low loss of 0.11 V and the formation of the PTB7–Th:PC71BM blend led to a voltage loss of 0.32 V. The dark leakage current–density is comparable for all three cell configurations.

Active layer	$V_{\mathrm{oc}}(V)$ ($\pm$ 0.01)	$j_{\mathrm{sc}}(mA/cm^{-1})$ (from EQE)	FF(%) ($\pm$ 0.1)	PCE(%)(max.)
PBDB-T-2F:IT4F	0.87	20.1 (19.1) $\pm$ 0.2	70	12.2 (12.7)
PBDB-T-2F:EH-IDTBR	1.08	4.0 (3.9) $\pm$ 0.4	48	2.0 (2.1)
PBDB-T-2F:PC71BM	0.89	11.9 (11.0) $\pm$ 0.3	63	6.7 (6.9)
PTB7-Th:IT4F	0.68	17.0 (16.3) $\pm$ 0.2	66	8.0 (8.1)
PTB7-Th:EH-IDTBR	1.01	16.9 (16.4) $\pm$ 0.4	57	9.6 (9.8)
PTB7-Th:PC71BM	0.79	14.6 (14.3) $\pm$ 0.3	41	4.7 (4.8)

Table 1: Solar–cell parameters for the PBDB-T-2F:acceptor OSCs under $100\,\mathrm{mW/cm}^{-2}$ AM1.5 light intensity illumination. j_{sc} values written in parentheses were derived from EQE measurements using Eq. 2.25. PCE values written in parentheses are the highest obtained numbers across several pixels.

As can be seen from table 1, non–fullerene acceptor based devices show significantly higher j_{sc} than their fullerene based counterparts. This can be ascribed to the overlapping and complementary absorption bands in the visible spectral range shown in Fig. 5.2 and Fig. 5.3. The direct light absorption in the acceptor can effectively contribute to the photocurrent generation.

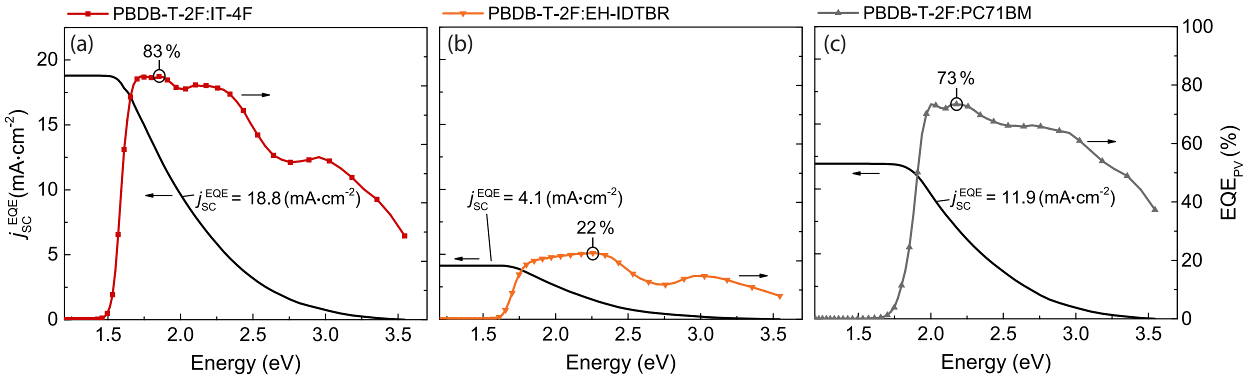

Figure 5.8: EQE$_{PV}$ spectra for the PBDB-T-2F:acceptor OSCs and the integrated values for the j_{sc}^{EQE} according to Eq. 2.25 (a) PBDB–T–2F:IT4F, (b) PBDB–T–2F:EH–IDTBR, and (c) PBDB–T–2F:PC71BM.

5.2.2 External quantum efficiency measurements

In order to investigate the photon energy–dependent efficiency of photocurrent generation, the external quantum efficiency (EQE$_{PV}$) was measured for all studied material combinations by using the solar cell spectral–response setup (see section 4.1.4). EQE$_{PV}$ measurements were also performed to confirm the j_{sc} of the solar cells.

Fig. 5.8 shows the EQE$_{PV}$ measurements for the PBDB–T–2F:acceptor OSCs. EQE$_{PV}$ values correspond to the right axis and the calculated j_{sc} values using Eq. 2.25 correspond to the left axis. As presented in Fig. 5.8(a) the PBDB–T–2F:IT4F based device shows a broad EQE$_{PV}$ response (red–squares) from ~ 1.5 eV till the UV–spectral region, and a maximum of 83 % at 1.85 eV. EQE$_{PV}$ values were measured till 3.5 eV as for higher photon–energies the light absorption of the glass substrate is no longer negligible and the reduced photon flux in the solar spectrum is less relevant for photocurrent generation. The low energy onset of the EQE$_{PV}$ coincides well with absorption onset of the IT4F acceptor thin film shown in Fig. 5.2(a). This shows that the direct photon absorption in the acceptor material is capable for efficient photocurrent generation. The broad blend absorption from ~ 1.5 eV till ~ 2.5 eV leads to a high EQE$_{PV}$ response in the same spectral region. The integrated j_{sc}^{EQE} value, represented by the black–solid line was 18.8 $\mathrm{mA \cdot cm^{-2}}$, which agrees well with the $j(V)$–measurements shown in Fig. 5.4(a).

The low cell performance of the PBDB–T–2F:EH–IDTBR due to the zero IP offset, manifests itself again in the EQE$_{PV}$ of the cell. Fig. 5.8(b) shows the EQE$_{PV}$ spectrum for the PBDB–T–2F:EH–IDTBR blend device. The EQE$_{PV}$ response is shallow over the whole measured spectrum with a maximum of 22 % at 2.25 eV. The onset of the EH–IDTBR absorption at ~ 1.6 eV as well as the he high energy peak at ~ 3.1 eV shown in Fig. 5.4(b) can also be found in the $\mathrm{EQE_{PV}}$ spectra. The low $\mathrm{EQE_{PV}}$ response can be attributed to the lack of driving force for excition dissociation caused by the zero IP offset of the blend materials. The low $\mathrm{EQE_{PV}}$ response also led to a low short–circuit current integration of $j_{\mathrm{sc}}^{\mathrm{EQE}} = 4.1\,\mathrm{mA \cdot cm^{-2}}$, which agrees well with $j(V)$–measurements shown in Fig. 5.4(b).

The $\mathrm{EQE_{PV}}$ values for the fullerene reference cell PBDB–T–2F:PC71BM are shown in Fig. 5.8(c). The spectra shows a broad response from $\sim 1.75\,\mathrm{eV}$ till the UV–spectral region with a maximum of 73 % at 2.0 eV. The $\mathrm{EQE_{PV}}$ onset and peak coincides with the PBDB–T–2F absorption shown in Fig. 5.4(c). The integrated $j_{\mathrm{sc}}^{\mathrm{EQE}} = 11.9\,\mathrm{mA \cdot cm^{-2}}$ matches the value obtained by $j(V)$–measurements.

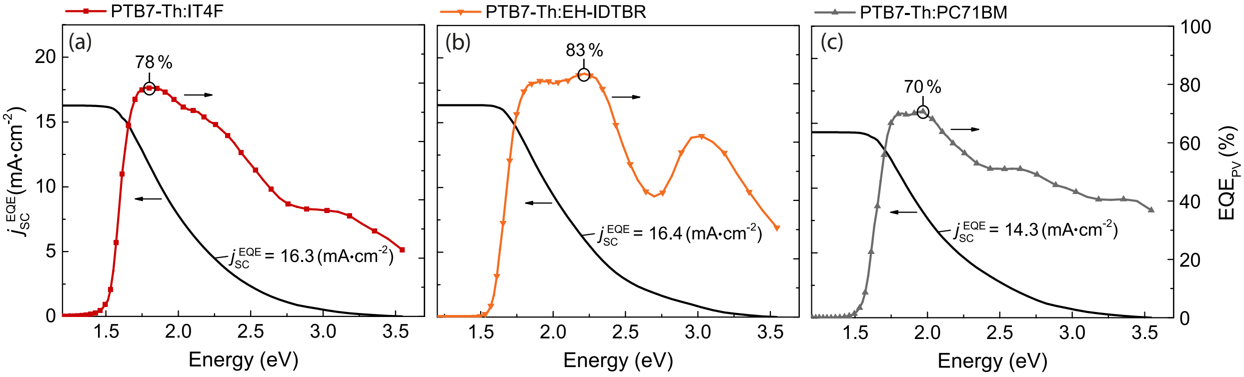

Figure 5.9: $\mathrm{EQE_{PV}}$ spectra for the PTB7–Th:acceptor OSCs and the integrated values for the $j_{\mathrm{sc}}^{\mathrm{EQE}}$ according to Eq. 2.25 (a) PTB7–Th:IT4F, (b) PTB7–Th:EH–IDTBR, and (c) PTB7–Th:PC71BM.

External quantum efficiency measurements were also performed for the PTB7–Th:acceptor OSCs. The obtained results for $\mathrm{EQE_{PV}}$ and integrated $j_{\mathrm{sc}}^{\mathrm{EQE}}$ are shown in Fig. 5.9. PTB7–Th:IT4F cells exhibited an $\mathrm{EQE_{PV}}$ spectrum shown in Fig. 5.9(a). The $\mathrm{EQE_{PV}}$ has an onset at $\sim 1.5\,\mathrm{eV}$ coinciding with the IT4F aborption onset and a maximum of 78 % at the PTB7-Th absorption maximum at 1.76 eV. The $j_{\mathrm{sc}}^{\mathrm{EQE}} = 16.3\,\mathrm{mA \cdot cm^{-2}}$ agrees well with the j_{sc} obtained from $j(V)$–measurements.

The $\mathrm{EQE_{PV}}$ spectrum for the PTB7–Th:EH–IDTBR OSC is shown in Fig. 5.9(b). The solar cell achieves its maximum $\mathrm{EQE_{PV}}$ of 83 % at 2.2 eV by combining the absorption of donor and acceptor in the same photon energy region between 1.55 eV and 2.5 eV. The high energy peak at $\sim 3.1\,\mathrm{eV}$ can be attributed to the EH–IDTBR absorption. The $j_{\mathrm{sc}}^{\mathrm{EQE}} = 16.4\,\mathrm{mA \cdot cm^{-2}}$ agrees well with the $j(V)$–measurements shown in Fig. 5.6(b).

The fullerene reference cell PTB7–Th:PC71BM reveals an $\mathrm{EQE_{PV}}$ spectrum shown in Fig. 5.9(c). The onset of the $\mathrm{EQE_{PV}}$ spectrum agrees well with the absortion onset of the donor polymer. The highest $\mathrm{EQE_{PV}}$ at $\sim 2.2\,\mathrm{eV}$ value was 73 %. The broad $\mathrm{EQE_{PV}}$ response led to a $j_{\mathrm{sc}}^{\mathrm{EQE}} = 14.3\,\mathrm{mA \cdot cm^{-2}}$, which was also obtained from $j(V)$–measurements.

5.2.3 Electroluminescence measurements

In order to investigate the effects occuring after the CT–state formation in the BHJ of an OSC, the electroluminescence (EL) spectra of the neat donor and acceptor components were measured and compared to the blend configurations. EL spectra were obtained by applying a forward voltage to the contacts of the cells and analyzing the emitted photons using the electroluminescence–setup (see section 4.1.6). The injection currents were kept low to ensure quasi–equilibrium [60].

Fig. 5.10(a) shows the measured normalized EL spectra for the PBDB–T–2F:IT4F blend and pristine components. By comparing the peak EL energies of the neat PBDB–T–2F (blue–diamonds) and the pristine IT4F (red–squares) cell to the EL peak energy of the blend cell (black–circles), it can be clearly seen that the formation of the BHJ leads to a significant red shift of the EL. The EL spectrum shows a peak in the IR–spectral region and a shoulder at ∼ 1.6 eV at the IT4F peak emission.

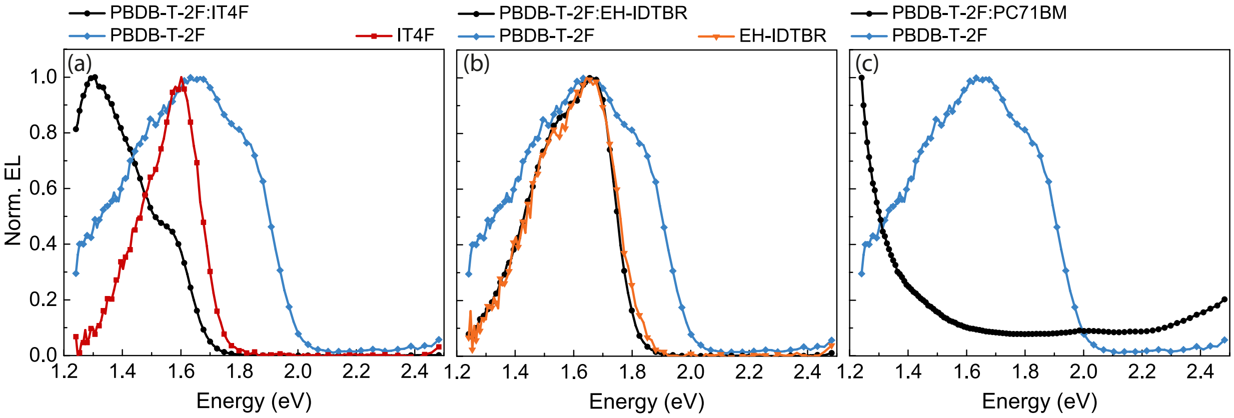

Figure 5.10: Normalized EL spectra for the PBDB-T-2F:acceptor OSCs (a) PBDB–T–2F:IT4F, (b) PBDB–T–2F:EH–IDTBR, and (c) PBDB–T–2F:PC71BM.

The normalized EL spectra for the solar cell with the zero IP offset PBDB–T–2F:EH–IDTBR are shown in Fig. 5.10(b). In contrast to the PBDB–T–2F:IT4F cell, the EL spectrum of the PBDB–T–2F:EH–IDTBR cell and the EH–IDTBR emission largely overlap and have a peak at 1.65 eV. The CT–state emission shows no spectral shift. Such behavior may arise from two different reasons. First, the CT–states could be degenerate or be hybridized with the singlet excitons and therefore absorb and emit in the same region. Second, if the electronic coupling between the GS and CT–states is very weak, the CT–state could have a lower energy peak, which, however, could not be detected by optical measurements [86].

Normalized EL spectra for the fullerene reference cell PBDB–T–2F:PC71BM are shown in Fig. 5.10(c). Within this work it was not possible to produce a stand–alone PC71BM solar cell, therefore, no EL spectrum is shown for neat PC71BM. The blend emission represented by the black–circles, shows the strongly redshifted peak, which is typical for polymer:fullerene CT–state formation [58].

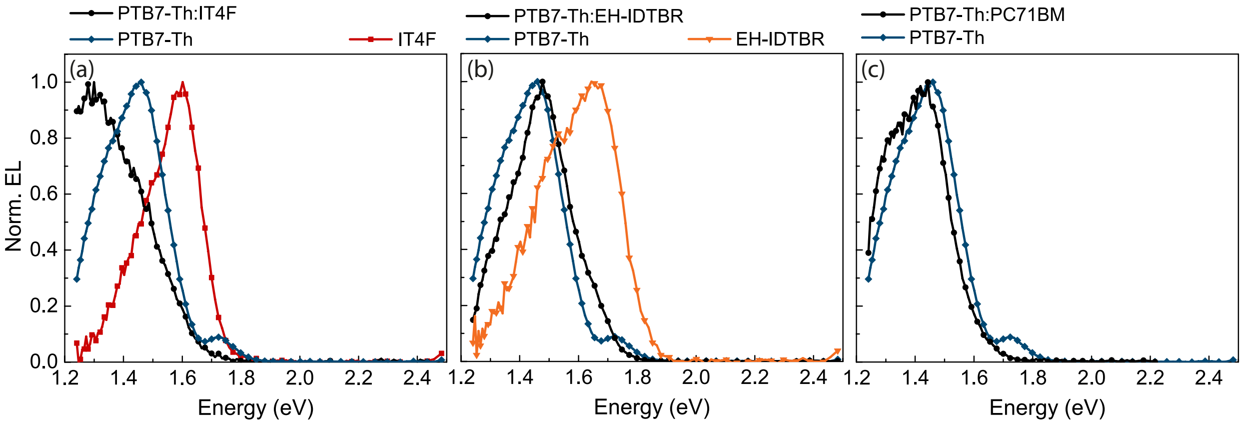

Figure 5.11: Normalized EL spectra for the PTB7–Th:acceptor OSCs (a) PTB7–Th:IT4F, (b) PTB7–Th:EH–IDTBR, and (c) PTB7–Th:PC71BM.

CT–state emission spectra were also measured for the PTB7–Th:acceptor solar cells. The corresponding normalized EL spectra are shown in Fig. 5.11.

The EL spectra for the PTB7–Th:IT4F based device are shown in Fig. 5.11(a) and revealed a similar behavior than for the PBDB–T–2F:IT4F cell (Fig. 5.10(a)). The CT state formation led to a redshifted blend emission with two shoulders at the spectral position of the corresponding neat donor and acceptor emission peaks.

Normalized emssion spectra for the PTB7–Th:EH–IDTBR cell are shown in Fig. 5.11(b). The CT–state emission is dominated by the polymer emission and, therfore, only shows a peak at 1.47 eV and a shoulder at the EH–IDTBR emission peak 1.65 eV.

The normalized EL measurement of the fullerene reference cell PTB7–Th:PC71BM is depicted in Fig. 5.11(c). It can be assumed that the spectrum would feature a not detected redshifted peak in the IR–spectral region compareable to the PBDB–T–2F:PC71BM emission.

5.2.4 Intensity dependence of the open–circuit voltage

The measurement of the open–circuit voltage versus the illuminance can provide important insights into the recombination mechanisms in OSCs. It can reveal differences between cells that may not be noticeable by just comparing parameters at 1 sun illumination intensity. Intensity dependent V_{oc} measurements were performed with the ModuLab XM PhotoEchem optical and electrical measurement system (see chapter 4.1.7). The intensity of the monochromatic 575 nm LED was altered from 1 to 100% of the LED power with 5 steps per decade.

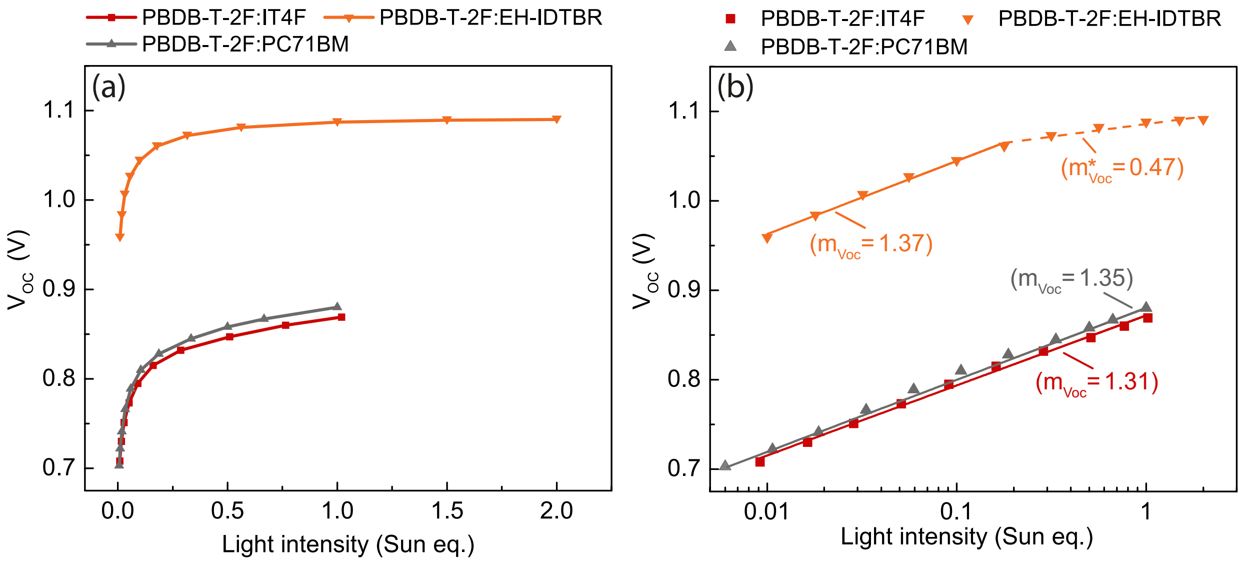

Figure 5.12: (a) Intensity dependence of the V_{oc} for the PBDB-T-2F:acceptor solar cells. (b) Semi–logarithmic plot of the V_{oc} against the light intensity the extracted ideality factors m. The solid lines, in the corresponding colors, indicate the linear fits to the V_{oc} data.

Fig. 5.12(a) shows the resulting V_{oc} against the light intensity with so–called sun–equivalent units for the PBDB–T–2F:acceptor based solar cells. As a reminder, sun–equivalent is defined as the monochromatic light intensity that would arise the same open–circuit voltage as an equivalent AM1.5 spectrum at a solar–simulator (see chapter 4.1.2 and 4.1.7). The V_{oc} drops off rapidly as the light intensity is reduced. This is in close agreement with the predicted curve shape discussed in section 2.4. With the decreasing V_{oc} also the PCE drops and, therefore, it is noteworthy to mention that in real–world use, it is essential that the cells maintain a reasonable performance over a wide range of intensities. The PBDB–T–2F:IT4F (red–squares) and the fullerene reference PBDB–T–2F:PC71BM (grey–up triangles) reached their respective 1 Sun V_{oc} value at ∼ 100 % of the maximum LED intensity. In contrast, the PBDB–T–2F:EH–IDTBR cells were able to reach the 1 Sun eq. V_{oc} already at ∼ 50 % of the maximum LED intensity, which explaines the values shown up to 2 Sun eq..

Fig. 5.12(b) shows the same V_{oc} versus light intensity data in a semi–logarithmic plot. The V_{oc} values for each device were linearly fitted to calculate the ideality factor m_{Voc} with Eq. 2.10. The resulting ideality factors are shown in the figure and collected in Tab. 2. The PBDB–T–2F:IT4F solar cell exhibited an ideality factor of $m_{\mathrm{Voc}} = 1.31 \pm 0.03$. The fullerene reference based on the PBDB–T–2F:PC71BM blend material, revealed a similar value of $m_{\mathrm{Voc}} = 1.35 \pm 0.05$. This was consistent across several pixels on the devices. The errors were calculated using the fitting parameters. As explained in section 2.4, an ideality factor between one and two indicates that trap states are involved during charge carrier recombination [29]. Both carrier recombination in the depletion zone of the bulk–heterojunction, and diffusion current processes are present [28].

The PBDB–T–2F:EH–IDTBR solar cell shows two different phases. First, for light intensities < 0.2 Sun eq., an ideality factor of $m_{\mathrm{Voc}} = 1.37 \pm 0.05$ was calculated, which indicates the same behavior as for the other two acceptors. Secondly, for higher intensities, the factor dropped to $m^{*}_{\mathrm{Voc}} = 0.47 \pm 0.05$, implying that a different recombination process is present, which could not be addressed during the framework of this thesis.

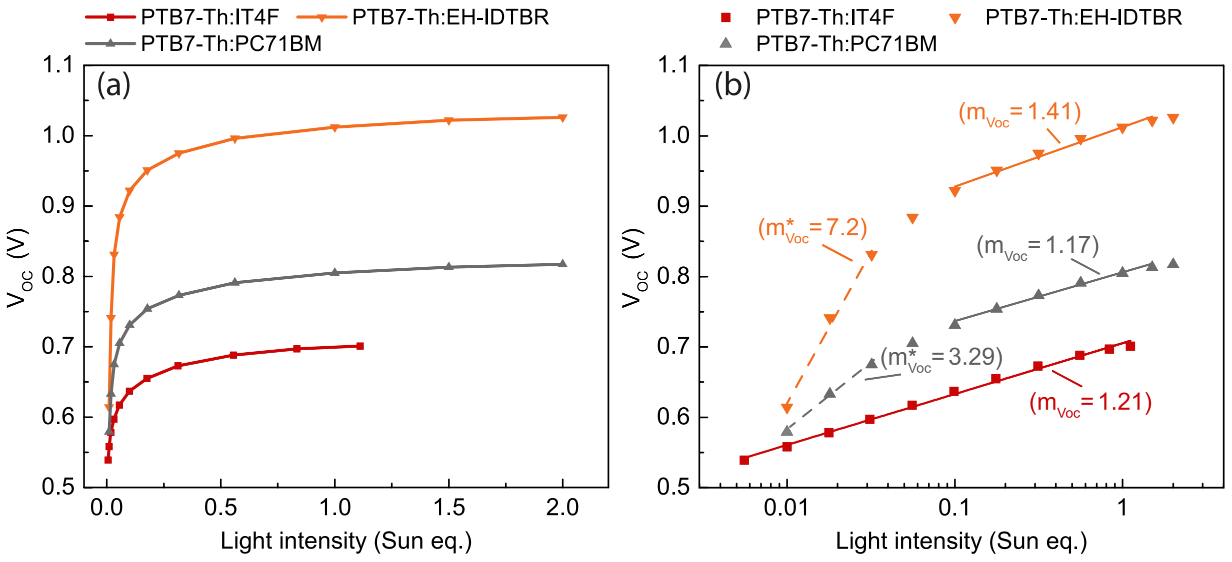

Figure 5.13: (a) Intensity dependence of the V_{oc} for the PTB7–Th:acceptor solar cells. (b) Semi–logarithmic plot of the V_{oc} against the light intensity the extracted ideality factors m. The solid lines, in the corresponding colors, indicate the linear fits to the V_{oc} data.

The same measurement procedure, as discussed above, was done for PTB7–Th:acceptor based solar cells. The obtained results for the intensity dependent open–circuit voltage measurements are shown in Fig. 5.13. Again, the cells exhibit the predicted curve form discussed in section 2.4. The PTB7–Th:EH–IDTBR and the fullerene reference PTB7–Th:PC71BM solar cell, were able to reach the 1 Sun eq. V_{oc} already at $\sim 50\,\%$ of the maximum LED intensity, which explains the values shown up to 2 Sun eq..

For light intensities > 0.1 Sun eq. all three devices show m_{voc} factors between one and two (see chapter 2.4), implying that both carrier recombination in the depletion zone of the bulk–heterojunction, and diffusion current processes are present. The values were consistent accros several pixels on the device.

Active layer	d (nm)	τ (μs)	m_{Voc}	m_{Hrec}
PBDB-T-2F:IT4F	102 ± 6	1.3	1.31 ± 0.03	1.14 ± 0.03
PBDB-T-2F:EH-IDTBR	99 ± 5	2.1	1.37 ± 0.05	–
PBDB-T-2F:PC71BM	98 ± 3	0.8	1.35 ± 0.05	1.17 ± 0.02
PTB7-Th:IT4F	95 ± 3	1.4	1.21 ± 0.02	1.16 ± 0.01
PTB7-Th:EH-IDTBR	103 ± 5	0.6	1.41 ± 0.08	1.18 ± 0.04
PTB7-Th:PC71BM	110 ± 4	0.9	1.17 ± 0.05	1.02 ± 0.03

Table 2: Solar–cell parameters from IMVS response of the PBDB-T-2F:acceptor OSCs. τ effective electron lifetime, m_{Voc} ideality factor taken from the light intensity dependence of V_{oc}, m_{rec} ideality factor calculated from the recombination impedence H_{rec} against V_{oc}.

5.3 IMVS–Measurements

IMVS measurements at varying DC light intensities were performed, to get further insights into the charge recombination processes within the solar cell. All measurements were carried out with the ModuLab XM PhotoEchem optical and electrical measurement system (see section 4.1.7) over the same range of light intensities as in chapter 5.2.4, and therefore V_{oc} range. During the IMVS measurements, no charge was extracted as the OSCs were held at open–circuit.

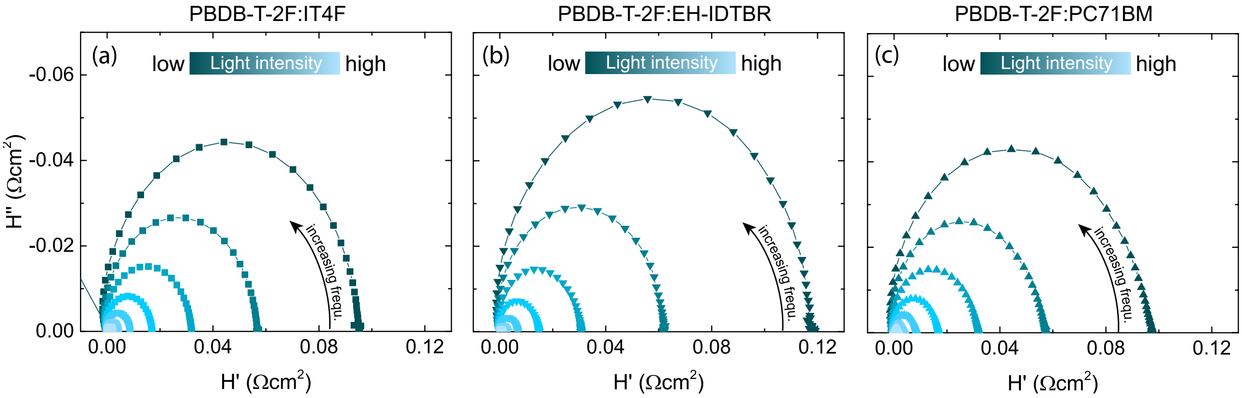

Figure 5.14: Intensity dependence of IMVS spectra measured at open circuit conditions for the PBDB-T-2F:acceptor solar cells represented as a Nyquist complex plane plot. The frequency range is between 1 Hz and 1 MHz. (a) PBDB–T–2F:IT4F 1:1 (w/w) (b) PBDB–T–2F:EH–IDTBR 1:2.5 (w/w) (c) PBDB–T–2F:PC71BM 1:1.5 (w/w).

The measured IMVS Nyquist plots for the three PBDB-T-2F:acceptor based solar cells are shown in Fig. 5.14(a,b,c). Spectra are shown from low intensities (dark blue curves) to higher intensities (light blue curves). The IMVS responses, measured from 1 Hz to 1 MHz, exhibited a semicircular curve form, which is typical for such impedance measurements and agrees well with Eq. 2.34, and Fig. 2.13, shown in the theory section. One can see that the real part H', as well as the imaginary part H'' of the transfer function H, decreases with increasing light intensity. Such behavior can be attributed to the intensity dependence of the open–circuit voltage V_{oc} and, thus, the recombination resistance R_{rec} and the recombination impedance H_{rec}. The recombination impedance, which corresponds to H', varies with changing light intensity, following Eq. 2.37. Respective measurements for PTB7–Th:acceptor cells are shown in the appendix.

In order to compare between the three PBDB–T–2F:acceptor solar cell types, Fig. 5.15 shows the obtained IMVS values in a Nyquist complex plane plot at 1 Sun eq. light intensity. All three types of acceptors, in combination with the PBDB–T–2F donor polymer, revealed different semicircular shapes. The PBDB–T–2F:IT4F solar cell shown in Fig. 5.15(a) ex-

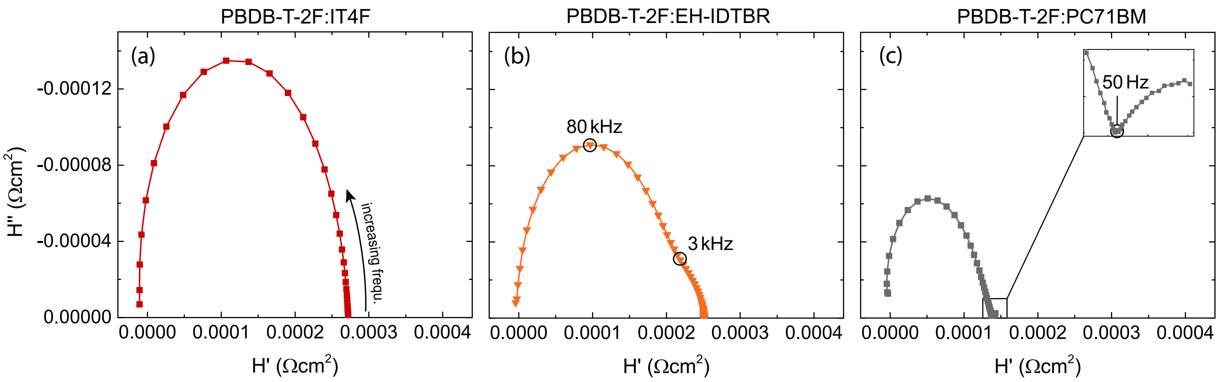

Figure 5.15: Nyquist complex plane plots for the PBDB-T-2F:acceptor solar cells at 1 Sun eq. light intensity. The frequency range is between 1 Hz and 1 MHz. (a) PBDB–T–2F:IT4F 1:1 (w/w) (b) PBDB–T–2F:EH–IDTBR 1:2.5 (w/w) (c) PBDB–T–2F:PC71BM 1:1.5 (w/w). The inset shows a detailed picture of the low–frequency arc in (c).

hibits a single semicircle. In contrast, the PBDB–T–2F:EH–IDTBR cell (b) shows e second semicircle in the low–frequency regime ($\sim$ 3 kHz) embedded into the high frequency arc peaking at ($\sim$ 80 kHz). The bottom axis, which belongs to the real part H' of the transfer function H, shows that the recombination impedance H_{rec} is lowest for the EH–IDTBR blende, compared to the IT4F (a) and PC71BM (c) cells. The lowest H_{rec} values, among the PBDB–T–2F:acceptor cells, were found for the PBDB–T–2F:PC71BM device shown in (c). The inset for the PBDB–T–2F:PC71BM cell, emphasizes the arise of a low–frequency arc ending at (50 Hz). This might be attributed to the grid frequency of the power supply.

The influence between different acceptor materials, in combination with the PBDB–T–2F donor polymer, is emphasized when plotting the recombination impedance H_{rec} against the light intensity in a log–log plot. The obtained results are presented in Fig. 5.16(a).

As mentioned in chapter 2.7.4, a linear dependence of H_{rec} to the light intensity (as shown by the black dashed line with a slope of -1 on the log–log plot) indicates that H_{rec} is indeed a recombination resistance [40]. Both the PBDB–T–2F:IT4F (red–squares) and the PBDB–T–2F:PC71BM (gray–up triangles) solar cell show a very similar dependence of the recombination impedance on the light intensity. The PBDB–T–2F:EH–IDTBR blend reveals a different behavior. In contrast to higher radiation power ($>$ 0.5 Suneq.) the slope of the H_{rec} slightly deviates from -1 at lower intensities ($<$ 0.5 Suneq.).

The differences between the recombination resistances of the three sample devices become even more evident in a semi–logarithmic plot against the open–circuit voltage V_{oc}. Fig. 5.16(b) shows $\log H_{\text{rec}}$ against V_{oc}. The data of each solar cell was linearly fitted to calculate the ideality factor m_{rec} with Eq. 2.38. The PBDB–T–2F:IT4F solar cell revealed an ideality

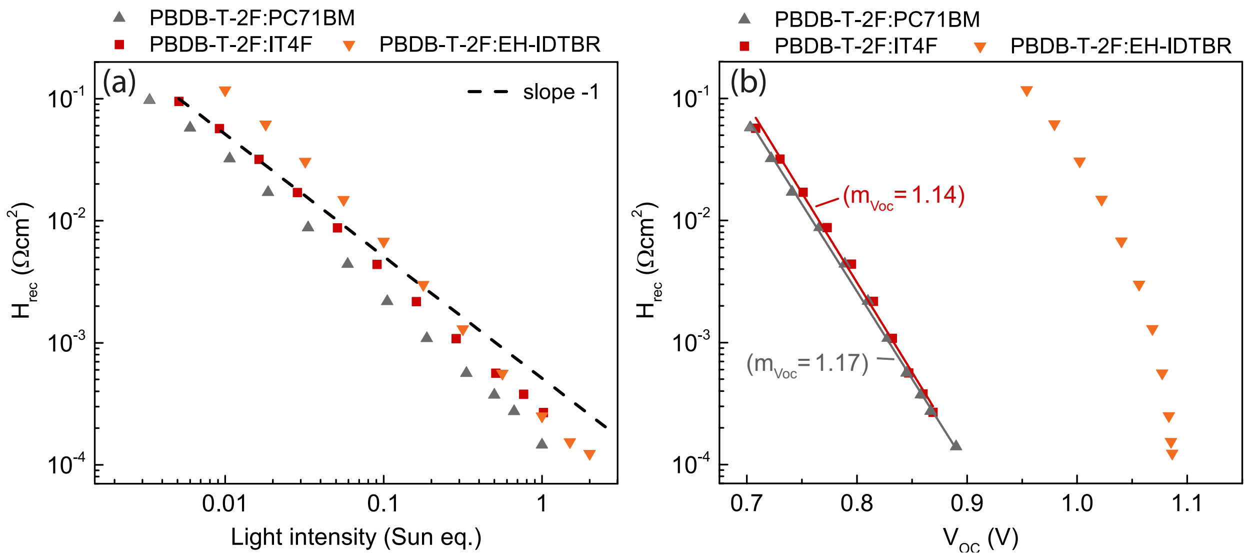

Figure 5.16: (a) Recombination impedance H_{rec} for the PBDB-T-2F:acceptor solar cells, as a function of light intensity on a log–log scale. The dashed–line with a slope $= -1$ corresponds to a linear dependence and indicates that H_{rec} is a recombination resistance [40]. (b) H_{rec} as a function of open–circuit voltage V_{oc} with the linear fits (solid colored lines) to the experimental data.

factor of $m_{\mathrm{rec}} = 1.17 \pm 0.02$ and the fullerene reference cell PBDB–T–2F:PC71BM a factor of $m_{\mathrm{rec}} = 1.14$. Both solar cell types show a linear trend over a wide voltage range. The determination of the ideality factor for the PBDB–T–2F:EH–IDTBR solar cell was not precise, and therefore, no value was exctracted. The obtained ideality factors were consistent across several pixels on the same solar cell. The ideality factors are similar to the coefficients obtained from the intensity dependence of the open-circuit voltage (see chapter 5.2.4). The summarized values obtained from Fig. 5.12, and Fig. 5.16 are shown in Tab. 2.

The same measurement procedure was also performed for PTB7–Th based solar cells. Fig. 5.17 shows the obtained IMVS values for the three PTB7–Th:acceptor based solar cells, in a Nyquist complex plane plot at 1 Sun eq. light intensity. Both non–fullerene acceptors (a) and (b) show comparable values for the real H' and the imaginary part H'' of the transfer function H. The fullerene reference shown in (c) reveals a slightly higher response for both the real and the imaginary part, implying that the charge recombination resistance at open–circuit conditions is higher for the fullerene than for non–fullerene blends.

The extraction of the H_{rec} values from the intensity dependent IMVS measurements, shown in Fig. 7.1 in the appendix, leads to the intensity dependent H_{rec} representation presented in Fig. 5.18)(a). The slope of the PTB7–Th:IT4F non–fullerene cell (red–squares) closely resembles the slope of the black dashed line, which indicates that H_{rec} is indeed a recombination resistance over a wide light intensity range. The PTB7–Th:EH–IDTBR (orange–down

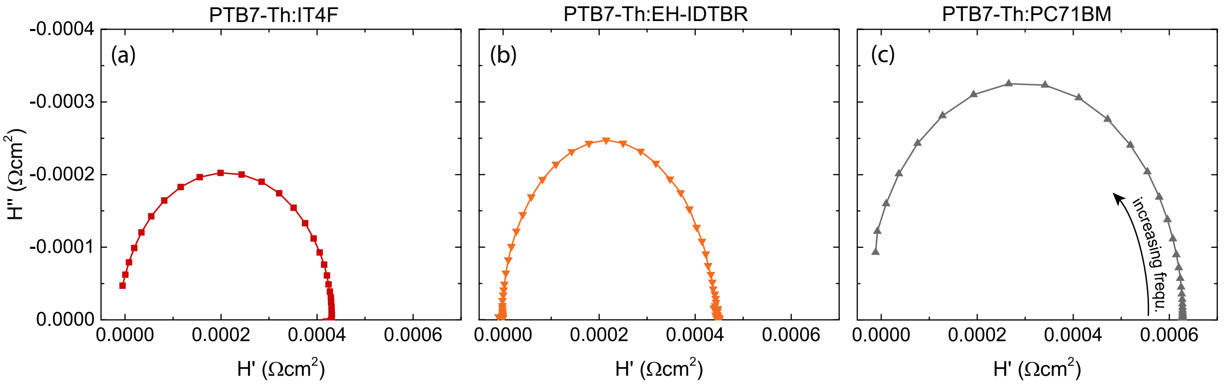

Figure 5.17: Nyquist complex plane plots for the PBDB-T-2F:acceptor solar cells at 1 Sun eq. light intensity. The frequency range is between 1 Hz and 1 MHz. (a) PTB7–Th:IT4F 1:1 (w/w) (b) PTB7–Th:EH–IDTBR 1:2.5 (w/w) (c) PTB7–Th:PC71BM 1:1.5 (w/w).

triangles) and the fullerene reference PTB7–Th:PC71BM (grey–squares) show an excellent fit to the black dashed line, for intensities > 0.2 Suneq..

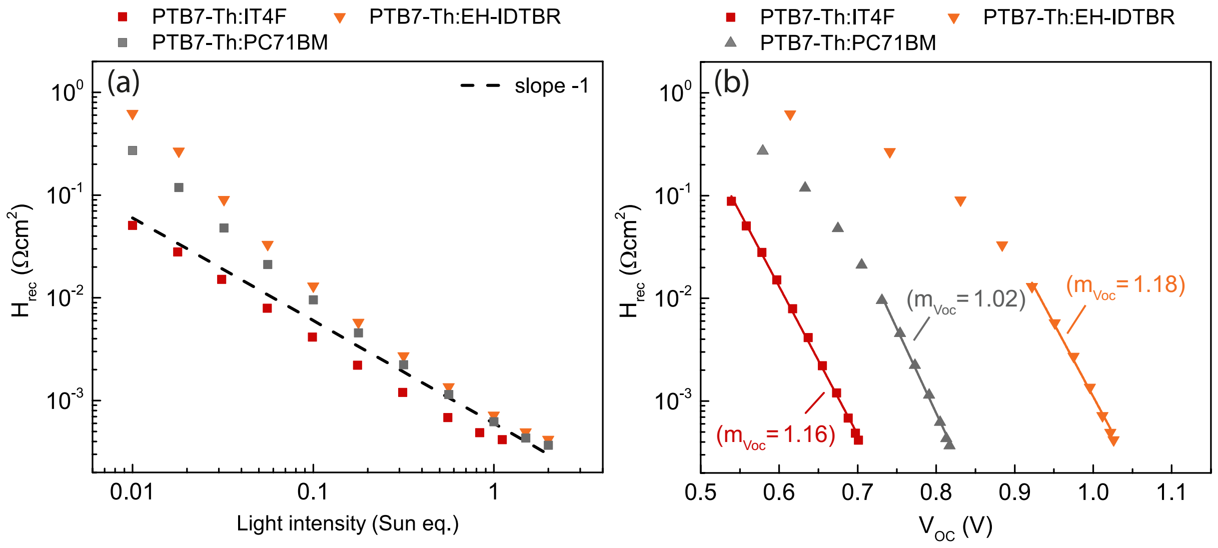

Figure 5.18: (a) Recombination impedance H_{rec} for the PTB7–Th:acceptor solar cells, as a function of light intensity on a log–log scale. The dashed–line with a slope $= -1$ corresponds to a linear dependence and indicates that H_{rec} is a recombination resistance [40]. (b) H_{rec} as a function of open–circuit voltage V_{oc} with the linear fits (solid colored lines) to the experimental data.

Recombination impedance plots as a function of the open–circuit voltage are presented in Fig. 5.18(b). The H_{rec} values for the PTB7–Th:IT4F solar cell, were linearly fitted to obtain the ideality factor $m_{\text{rec}} = 1.16 \pm 0.01$. For the PTB7–Th:EH–IDTBR and the PTB7–Th:PC71BM cells, only the H_{rec} values for intensities > 0.2 Suneq. were fitted. The calculated ideality factors were $m_{\text{rec}} = 1.18 \pm 0.04$ for the EH–IDTBR cell and $m_{\text{rec}} = 1.02 \pm 0.03$

for the PC71BM cell. As all calculated ideality factors were close to one, it signifies that the diffusion current processes are dominant in those devices.

5.3.1 Extracting charge carrier recombination lifetimes

In addition to the shown results above, IMVS measurements can be used to determine the recombination lifetimes in OSCs. A detailed description is given in section 2.5, and 2.7.3. To extract the characteristic recombination lifetimes, the imaginary part H' of the transfer function H is plotted as a function of excitation frequency.

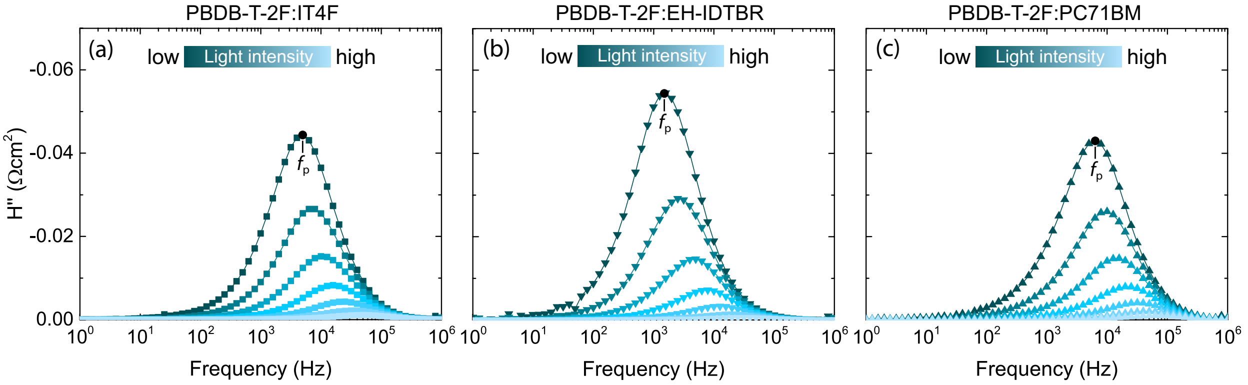

Figure 5.19: Intensity dependence of IMVS spectra measured at open circuit conditions for the three devices (a) PBDB–T–2F:IT4F 1:1 (w/w), (b) PBDB–T–2F:EH–IDTBR 1:2.5 (w/w), and (c) PBDB–T–2F:PC71BM 1:1.5 (w/w), represented as Bode–plots of the imaginary components of the transfer function vs. the modulation frequency. The frequency range is between 1 Hz and 1 MHz.

Fig. 5.19 shows the evolution of the IMVS Bode–plots with increasing excitation light intensity for the three sample devices (a) PBDB–T–2F:IT4F 1:1 (w/w), (b) PBDB–T–2F:EH–IDTBR 1:2.5 (w/w), and (c) PBDB–T–2F:PC71BM 1:1.5 (w/w), respectively. Spectra are again shown from low intensities (dark blue curves) to higher intensities (light blue curves). The line shape of the shown data follows the theoretically predicted trend shown in Fig. 2.13(b). The time constant τ can be expressed in terms of frequency with $\tau = 1/(2\pi f_\mathrm{p})$. In IMVS measurements it is connected to the effective electron lifetime. The effective electron lifetimes τ, for the PBDB–T–2F based solar cells were extracted, by taking the inverse of the peak frequency f_p at the maximum of the imaginary transfer function H''. The effective electron lifetime depends on the number of electrons in the excited state of the organic semiconductor. A pronounced increase in the frequency f_p at the maxima of the IMVS Bode plots in Fig. 5.19(a,b,c) indicates that increasing the DC light intensity increases the number of electrons in the excited state and consequently decrease the effective electron lifetime. Respective measurements were also performed for PTB7–Th based solar cells. The corresponding plots are shown in the appendix.

In order to compare between the three PBDB–T–2F:acceptor solar cell types, Fig. 5.20 shows the obtained IMVS values in a Bode–plot type at 1 Sun eq. light intensity. The Bode–plots for the PBDB–T–2F:IT4F (a) and the PBDB–T–2F:PC71BM (c) solar cell exhibit a single high frequency process with one time constant. The time constants for each cell are marked in the plots and collected in Tab. 2. The IT4F based cell shows a peak at 140 kHz, which corresponds to a time constant $\tau = 1.1\,\mu$s. The fullerene reference cell containing PC71BM revealed a single peak at 190 kHz, which gives a $\tau = 0.8\,\mu$s. Again, like in the Nyquist complex plane plot shown in Fig. 5.15(b), the PBDB–T–2F:EH–IDTBR cell reveals a second low–frequency process ~ 3 kHz with a time constant $\tau_L \approx 50\,\mu$s. The high frequency process has a peak at 75 kHz, and a respective effective electron lifetime of $\tau_H 2.1\,\mu$s.

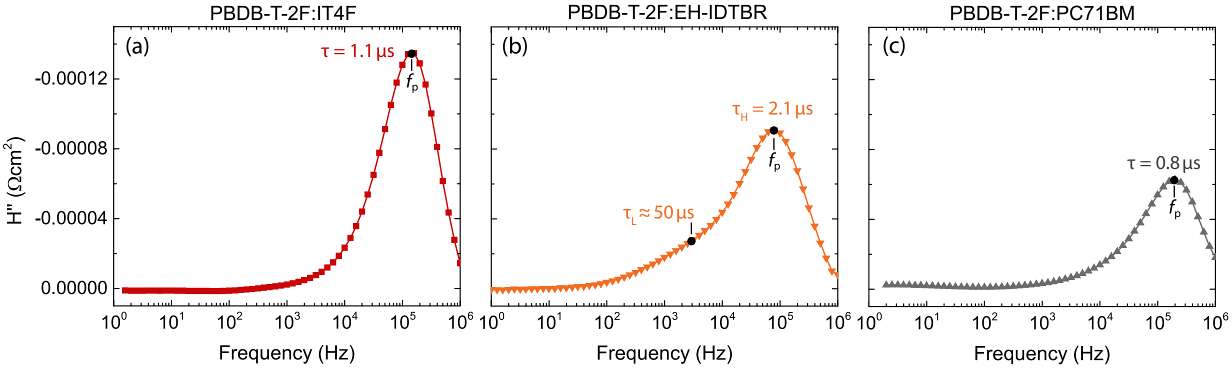

Figure 5.20: IMVS spectra measured at open circuit conditions for the three devices (a) PBDB–T–2F:IT4F 1:1 (w/w), (b) PBDB–T–2F:EH–IDTBR 1:2.5 (w/w), and (c) PBDB–T–2F:PC71BM 1:1.5 (w/w), at 1 Sun eq. light intensity, represented as Bode–plots of the imaginary components of the transfer function vs. the modulation frequency. The frequency range is between 1 Hz and 1 MHz.

Same measurements were done for PTB7–TH:acceptor based solar cells. Fig. 5.21 shows the Bode–plots of the imaginary components of the transfer function as a function of the modulation frequency for the PTB7–Th based solar cells. All three cell configurations show a single high frequency process with one time constant. The PTB7–Th:IT4F cell in (a) has a peak at 118 kHz, which results in an effective electron lifetime of $\tau_H 1.3\,\mu$s. The value is compareable to the time constant obtained with the PBDB–T–2F donor polymer. The PTB7–Th:EH–IDTBR solar cell shows a single peak at 260 kHz, resulting in the lowest observed effective electron lifetime of $\tau_H = 0.6\,\mu$s among all tested cell configurations. The fullerene reference cell PTB7-Th:PC71BM has a comparable time constant as the PBDB-T-2F:PC71BM cell of $\tau = 0.9\,\mu$s with a single peak at 180 kHz.

The effect of light intensity becomes obvious by plotting the effective electron lifetime τ as

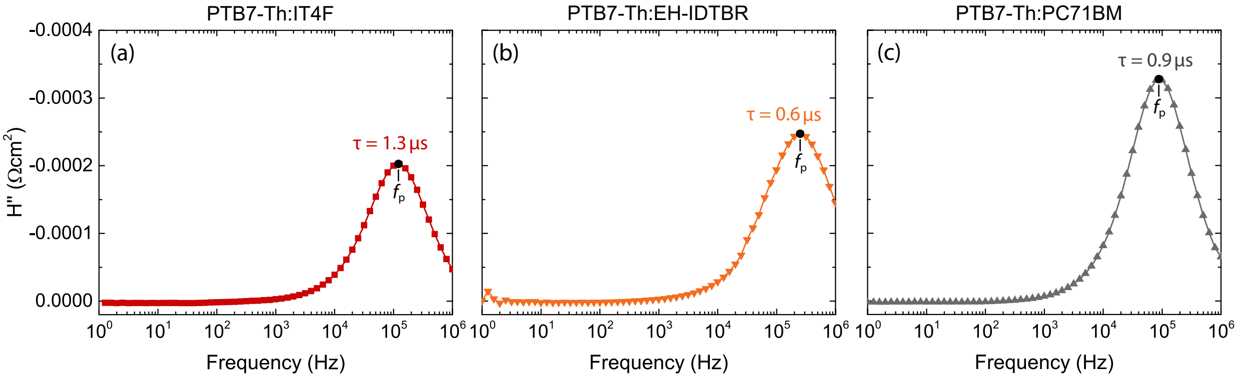

Figure 5.21: IMVS spectra measured at open circuit conditions for the three devices (a) PTB7–Th:IT4F 1:1 (w/w) (b) PTB7–Th:EH–IDTBR 1:2.5 (w/w) (c) PTB7–Th:PC71BM 1:1.5 (w/w) at 1 Sun eq. light intensity, represented as Bode–plots of the imaginary components of the transfer function vs. the modulation frequency. The frequency range is between 1 Hz and 1 MHz.

a function of the light intensity in a log–log plot.

Fig. 5.22(a) shows τ for the three PBDB–T–2F based solar cells, against the light intensities in units of sun–equivalents in a log–log plot. τ decreases with increasing light intensity. A decreased τ is, therefore, in common with the findings in Fig. 5.19(a,b,c).

As the effective electron lifetime depends on the number of electrons in the excited state of the organic semiconductor, it is important to compare lifetimes of different samples, at equal conditions. One way to do so is, plotting τ as a function of the open–circuit voltage (cf. Fig. 5.22(b)). The effective electron lifetime τ decreases with increasing V_{oc}. At 1 sun–equivalents, the PBDB–T–2F:EH–IDTBR device shows the highest electron lifetime of $\tau = 2.1\,\mu$s. The IT4F and PC71BM based solar cell have compareable lifetimes of $\tau = 1.3\,\mu$s and $\tau = 0.9\,\mu$s, respectively. The observed lifetimes are on close agreement with the literature [40].

Similar effective electron lifetimes were found for PTB7–Th based solar cells. Fig. 5.23(a) represents the obtained time constants as a function of light intensity. It can be seen that for low light intensities < 0.1 Sun eq., the EH–IDTBR and PC71BM cell revealed higher electron lifetime as the IT4F based solar cell. The situation is vice versa for higher light intensities. To compare the solar cells at equal conditions, Fig. 5.23(b) shows the obtained values as a function of open–circuit voltage. The lowest time constant of $\tau = 0.6\,\mu$s, among all tested cell configurations, was found for the PTB7–Th:EH–IDTBR solar cell. The PTB7–Th:PC71BM fullerene reference revealed a $\tau = 0.9\,\mu$s and the non–fullerene counterpart PTB7–Th:IT4F showed a time constant of $\tau = 1.4\,\mu$s.

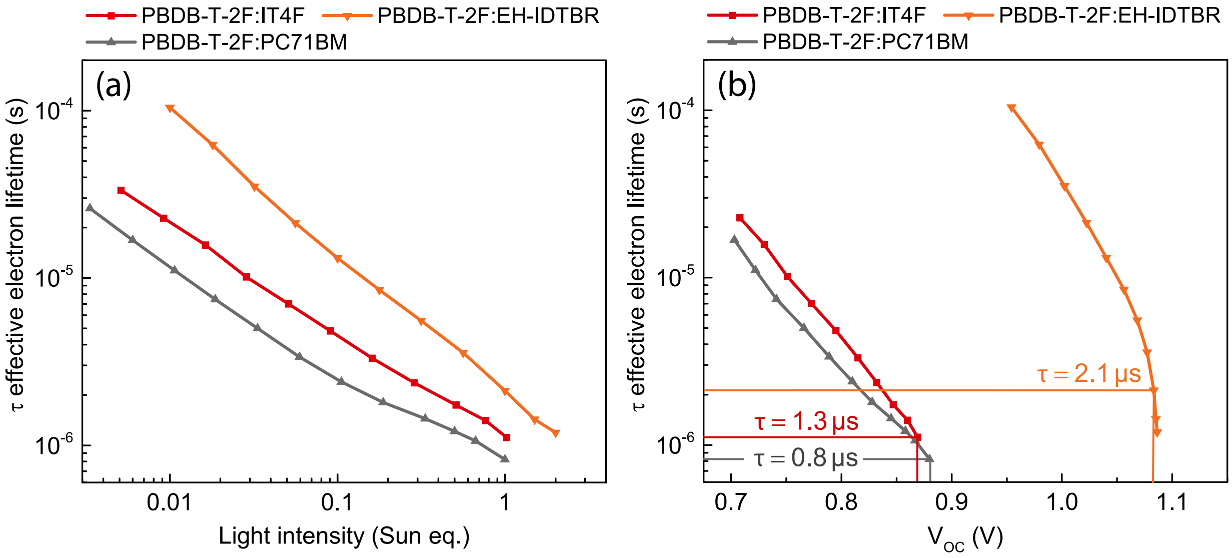

Figure 5.22: (a) Effective electron lifetime τ for the three devices PBDB–T–2F:IT4F 1:1 (w/w), PBDB–T–2F:EH–IDTBR 1:2.5 (w/w), and PBDB–T–2F:PC71BM 1:1.5 (w/w), as a function of light intensity. (b) τ as a function of open–circuit voltage V_{oc}. The three solid lines indicating the effective electron lifetimes at V_{oc} corresponding to 1 Sun on the sun simulator.

5.4 Stability measurements by MPP tracking

The steady–state stability of the OSCs were investigated by maximum power point (MPP) tracking of open and encapsulated cell configurations at ambient air. The MPP tracking was carried out with the experimental setup described in section 4.1.11. The obtained results of the MPP tracking were checked with initial, intermediate– and final–hour $j(V)$–measurements on the solar simulator.

Fig. 5.24(a) shows the obtained results for the PBDB–T–2F:IT4F OSCs with a 1:1 (w/w) ratio. It can be clearly seen that the encapsulated cell (blue diamonds) has a significantly better PCE over time than the open cell configuration (red–squares) exposed to ambient air. In fact, after 24 hours under constant illumination, the PCE of the open PBDB–T–2F:IT4F cell dramatically decreased to 1.1 % compared to 8.2 % of the encapsulated configuration. The inset shows the first two hours under illumination in more detail.

The same measurements were performed for the open and encapsulated configuration of the PTB7–Th:EH–IDTBR active layer materials. The obtained results are shown in Fig. 5.24(b). By comparing the results from (a) and (b) one can clearly see that the PTB7–Th:EH–IDTBR solar cells are less susceptible to ambient air than the PBDB–T–2F:IT4F cells. The PCE of the open cell configuration dropped from $\sim$ 10 % to $\sim$ 7 % after the first 24 hours of illumination. The inset depicts the first two hours in more detail.

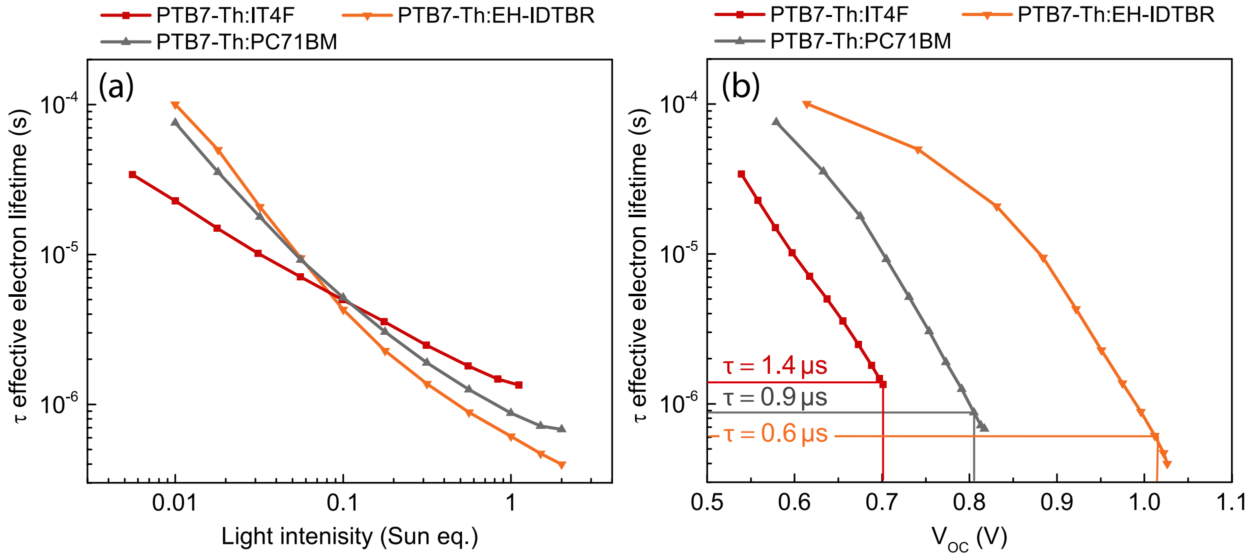

Figure 5.23: (a) Effective electron lifetime τ for the three devices PBDB–T–2F:IT4F 1:1 (w/w), PBDB–T–2F:EH–IDTBR 1:2.5 (w/w), and PBDB–T–2F:PC71BM 1:1.5 (w/w), as a function of light intensity. (b) τ as a function of open–circuit voltage V_{oc}. The three solid lines indicating the effective electron lifetimes at V_{oc} corresponding to 1 Sun on the sun simulator.

Both encapsulated active layer materials showed an initial PCE drop of $\sim 10\,\%$ in the first hour of illumination. This initial phase is often called *burn–in* degradation. The active layer material can suffer from photochemical reactions, thermochemical reactions, oxidative degradation through ozone formation on the surface, morphological changes, and impurity inclusions thru metal ion diffusion from the electrodes [87]. The photoactive materials directly exposed to the ambient conditions were bleached due to oxidative ozone degradation during the MPP tracking. The degradation processes of the electrodes can happen via oxidation, de–doping, delamination, and interfacial organometallic chemistry. However, the dominant process responsible for the burn–in phase, could not be addressed within the framework of this thesis.

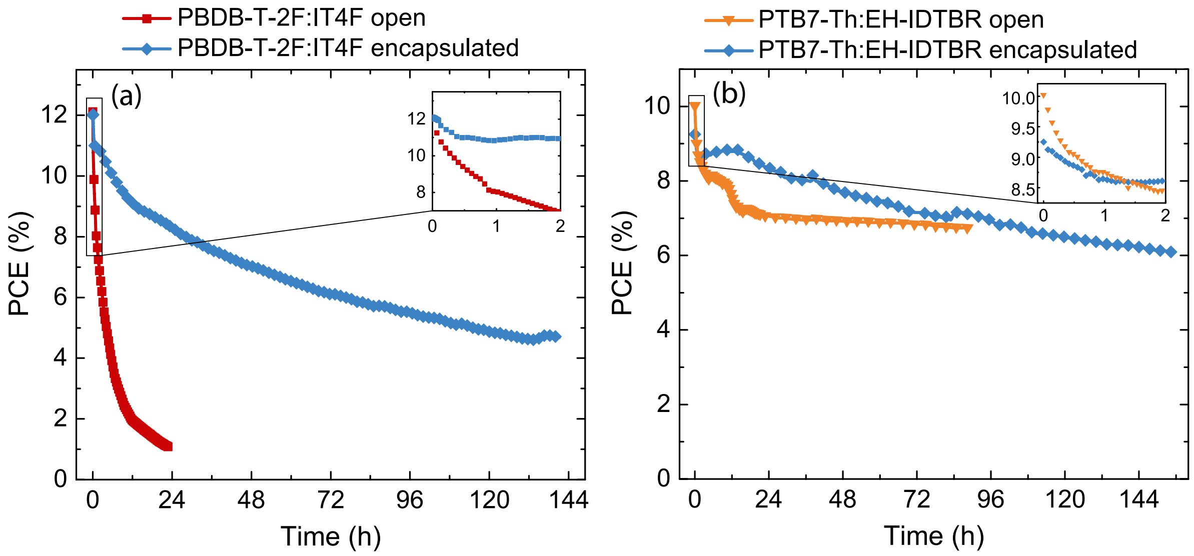

Figure 5.24: MPP tracking of the open and encapsulated (a) PBDB–T–2F:IT4F and (b) PTB7–Th:EH–IDTBR solar cells.

5.5 Sub bandgap external quantum efficiency measurements

In this section the results obtained from sub bandgap external quantum efficiency measurements are presented. The underlying theoretical background is discussed in section 2.9.

5.5.1 Determination of the optical band gap energies

Fig. 5.25 shows the determination of the optical gap energy E_{opt} for the (a) neat PBDB–T–2F and (b) neat PTB7–Th donor–only solar cells in the normalized reduced spectra as a function of energy. The EL spectra were carried out with the electroluminescence setup (see section 4.1.6) at low injection currents, and a voltage just slightly higher than the V_{oc}, to keep the system in quasi–equilibrium [60].The EQE_{PV} spectra of the neat polymers were measured using the amplified spectral response setup (see section 4.1.5). For the reduced representation the EL spectra were devided by E^3 and normalized and the EQE_{PV} spectra devided by E and normalized to the corresponding low energy peak/shoulder. For the donor–only PBDB–T–2F solar cell, the crossing point between the normalized reduced EL and reduced EQE_{PV} spectra yields an optical gap around $E_{\text{opt}} = 1.87\,\text{eV}$.

The neat PTB7–Th solar cell exhibited a lower optical gap energy of $E_{\text{opt}} = 1.63\,\text{eV}$. The presented results coincide with the values derived from cyclic–voltammetry ($E_{\text{opt,CV}}$) shown in Fig. 5.1.

Fig. 5.26 shows the determination of the optical gap energy E_{opt} for the acceptor–only solar

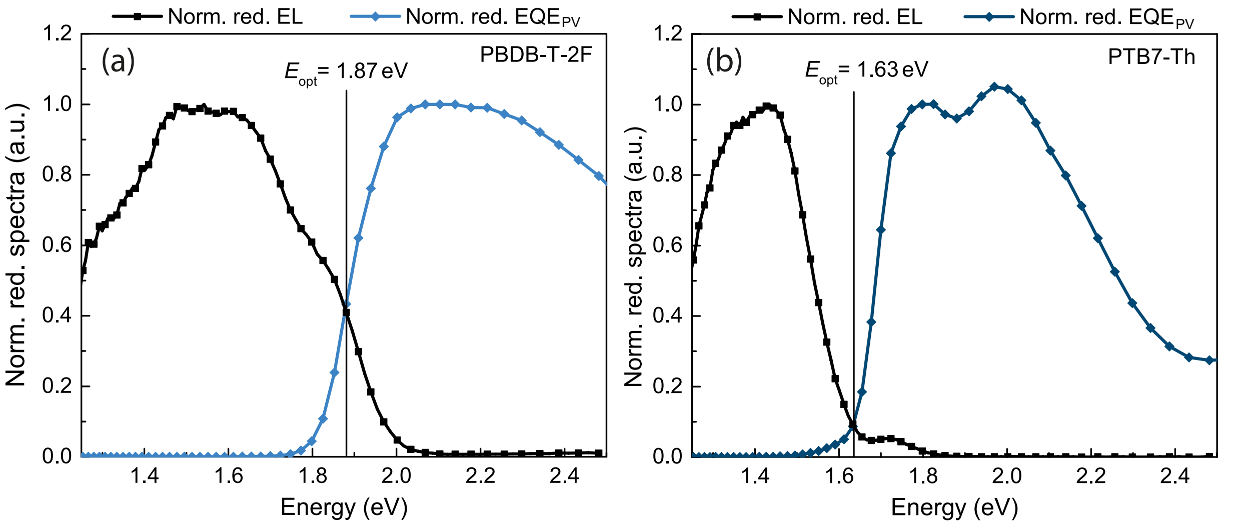

Figure 5.25: Determination of the optical gap energy E_{opt} for the donor–only solar cells (a) neat PBDB–T–2F and (b) neat PTB7–Th. The vertical black line indicates the crossing point (E_{opt}) between normalized reduced EL and EQE_{PV}, respecticely.

cells. The data were reduced and normalized as for the donor–only devices. The vertical black line in (a) and (b) indicates an optical gap energy for the IT4F device of $E_{opt} = 1.64$ eV and for the EH–IDTBR device of $E_{opt} = 1.71$ eV. Both obtained gap energy values are ~ 0.1 eV higher than the values measured with cyclic–voltammetry.

The summarized optical gap values are collected in Tab. 3.

Active layer	E_{opt} (eV)	$E_{opt,CV}$ (eV)
PBDB-T-2F	1.87	1.8
PTB7-Th	1.63	1.6
IT4F	1.64	1.5
EH-IDTBR	1.71	1.6
PC71BM	–	2.2

Table 3: Obtained optical band gap energies; E_{opt} from EL and EQE_{PV} measurements and $E_{opt,CV}$ from cyclic–coltammetry measurements.

By applying the same measurement procedure to the donor:acceptor OSCs, one can determine the CT–state energy of the blend. The reduced and normalized spectra are plotted on a logarithmic scale to visualize additional bands in the EQE_{PV} spectra better.

The CT–state determination for the PBDB–T–2F based solar cells are shown in Fig. 5.27. Again, the EL spectra were measured at low injection currents to keep the system in quasi–equilibrium [60]. At low injection currents, the EL spectrum of the BHJ solar cells is dominated by the direct emission of the CT–states [59]. Fits of the reduced and normalized EL

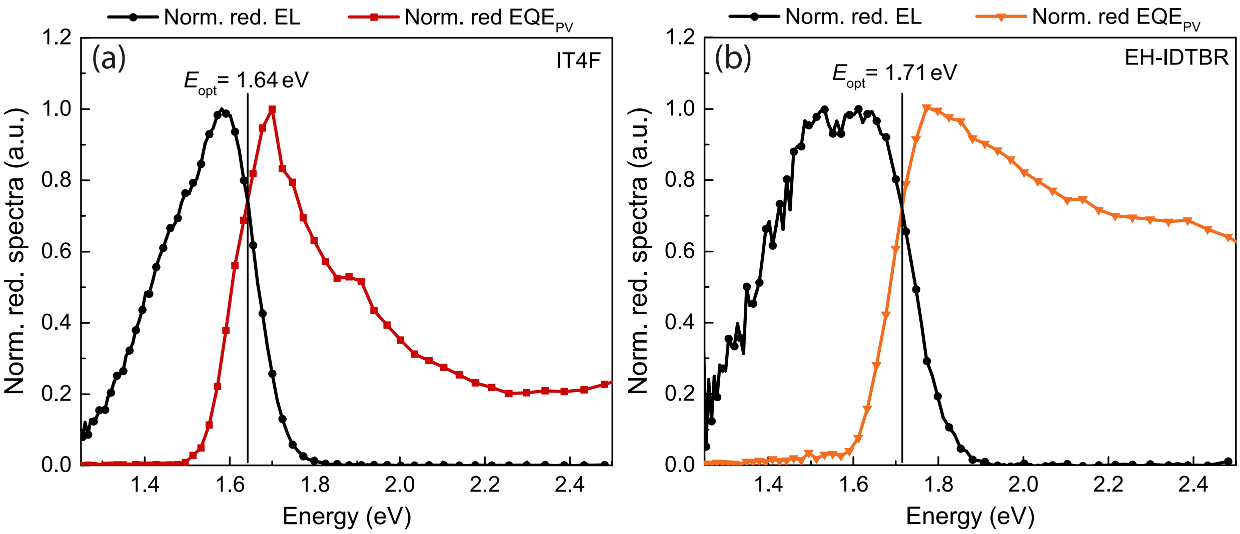

Figure 5.26: Determination of the optical gap energy E_{opt} for the acceptor–only solar cells (a) neat IT4F and (b) neat EH–IDTBR. The vertical black line indicates the crossing point (E_{opt}) between normalized reduced EL and EQE$_{\mathrm{PV}}$, respecticely.

and the EQE$_{\mathrm{PV}}$ spectra were done with Eq. 2.48 and Eq. 2.47, respectively. The resulting fits are shown as a dash–dotted line for the EL and dashed line for the EQE$_{\mathrm{PV}}$ spectra. The measured spectra for the PBDB–T–2F:IT4F solar cell, shown in Fig. 5.27(a), yields a CT–state energy of $E_{\mathrm{CT}} = 1.45\,\mathrm{eV}$ and a corresponding reorganization energy of $\lambda_{\mathrm{CT}} = 0.09\,\mathrm{eV}$. The obtained value coincides well with the actual crossing point of the two spectra. With the known $V_{\mathrm{oc}} = 0.87\,\mathrm{V}$ of the device and Eq. 2.50 and the optical band gap energy of the narrow–gap absorber, one can calculate the total voltage loss for the PBDB–T–2F:IT4F cell to be $V_{\mathrm{loss}} = 0.77\,\mathrm{V}$. The energetic loss accompanied by the CT state is calculated with Eq. 2.51 and yields $\Delta E_{\mathrm{CT}} = 0.19\,\mathrm{eV}$. The recombination losses were calculated with Eq. 2.52 and resulted in $\Delta V_{\mathrm{rec}} = 0.58\,\mathrm{V}$. ΔV_{rec} can be split into radiative ΔV_{r} and non–radiative ΔV_{nr} losses. ΔV_{r} was calculated with Eq. 2.57 and ΔV_{nr} with Eq. 2.58, respectively. The upper limit of the open–circuit voltage V_{r} can be determined with Eq. 2.53 and the obtained values from sub–bandgap EQE$_{\mathrm{PV}}$ measurements, by following the routine described in the corresponding theoretical section in 2.9. The upper limit of the open–circuit voltage for the PBDB–T–2F:IT4F cell results in $V_{\mathrm{r}} = 1.18\,\mathrm{V}$, which leads to a $\Delta V_{\mathrm{r}} = 0.27\,\mathrm{V}$ and a $\Delta V_{\mathrm{nr}} = 0.31\,\mathrm{V}$, respectively. Using Eq. 2.59 and ΔV_{nr}, this results in an $\mathrm{EQE}_{\mathrm{EL}} = 6.2 \cdot 10^{-6}$.

Blending the PBDB–T–2F polymer with another acceptor molecule also results in a different CT–state energy. The PBDB–T–2F:EH–IDTBR cell (Fig. 5.27(b)) revealed a CT–state energy of $E_{\mathrm{CT}} = 1.68\,\mathrm{eV}$, and a $\lambda_{\mathrm{CT}} = 0.11\,\mathrm{eV}$. With the measured $V_{\mathrm{oc}} = 1.08\,\mathrm{V}$ of the PBDB–T–2F:EH–IDTBR cell, the total voltage loss results in $V_{\mathrm{loss}} = 0.63\,\mathrm{V}$. The difference between the narrow–gap absorber, in this case the acceptor, and the CT–state energy is $\Delta E_{\mathrm{CT}} = 0.03\,\mathrm{eV}$. The voltage loss, due to different recombination channels, is

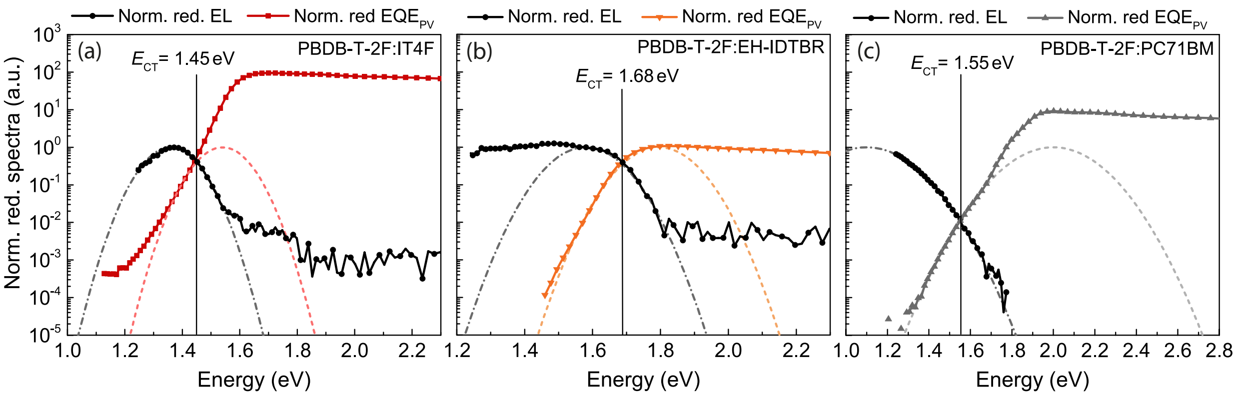

Figure 5.27: Semilogarithmic plots of the normalized and reduced EL and EQE$_{\mathrm{PV}}$ spectra. Dashed and dashed–dotted curves show Gaussian fits to either the reduced EL or the reduced EQE$_{\mathrm{PV}}$ spectra, using Eq. 2.48 and Eq. 2.47, respectively. Spectra are shown for (a) PBDB–T–2F:IT4F (b) PBDB–T–2F:EH–IDTBR and (c) PBDB–T–2F:PC71BM.

$\Delta V_{\mathrm{rec}} = 0.60\,\mathrm{V}$. Analysis of the sub–bandgap measurements revealed an upper limit for the open–circuit voltage of $V_{\mathrm{r}} = 1.35\,\mathrm{V}$, which leads to a $\Delta V_{\mathrm{r}} = 0.33\,\mathrm{V}$ and a $\Delta V_{\mathrm{nr}} = 0.27\,\mathrm{V}$, respectively. This solar cell showed the highest $\mathrm{EQE}_{\mathrm{EL}} = 2.9 \cdot 10^{-5}$ among all tested cell configurations within this study.

The fullerene reference cell PBDB–T–2F:PC71BM, shown in Fig. 5.27(c), yields a CT–state energy of $E_{\mathrm{CT}} = 1.55\,\mathrm{eV}$ and a high reorganization energy of $\lambda_{\mathrm{CT}} = 0.45\,\mathrm{eV}$. As the $V_{\mathrm{oc}} = 0.89\,\mathrm{V}$ the total voltage losses sum up to $V_{\mathrm{loss}} = 0.98\,\mathrm{V}$. The energetic losses acompanied with the CT–state are $\Delta E_{\mathrm{CT}} = 0.32\,\mathrm{eV}$, and the recombination losses are $\Delta V_{\mathrm{rec}} = 0.66\,\mathrm{V}$. These losses can be split into a $\Delta V_{\mathrm{r}} = 0.29\,\mathrm{V}$ and a $\Delta V_{\mathrm{nr}} = 0.37\,\mathrm{V}$. The radiative upper limit of the open–circuit voltage is $V_{\mathrm{r}} = 1.26\,\mathrm{V}$. The corresponding $\mathrm{EQE}_{\mathrm{EL}}$ equals $6.1 \cdot 10^{-7}$.

The same measurements were carried out for the PTB7–Th based solar cells. The obtained spectra and values are presented in Fig. 5.28. The PTB7–Th:IT4F solar cell (a) revealed a pronounced additional band at the low–energy tail of the EQE$_{\mathrm{PV}}$ spectrum, which could be perfectly fitted with Eq. 2.47. It can be assumed, that do to the so–called mirror–image–spectra (see section 2.9), both fits have to be symmetrical, and therefore, the shown fit is the only possible fit to match the EQE$_{\mathrm{PV}}$ tail and EL spectrum at the same time. The bluish solid line indicates the EL$_{\mathrm{CALC}}$ spectrum calculated with Eq. 2.60. This confirms the position of the measured EL spectrum. The crossing point of both fits and the spectra yields a CT–state energy of $E_{\mathrm{CT}} = 1.25\,\mathrm{eV}$, with a reorganization energy of $\lambda_{\mathrm{CT}} = 0.3\,\mathrm{eV}$. The PTB7–Th:IT4F solar cell revealed the lowest open–circuit voltage ($V_{\mathrm{oc}} = 0.68\,\mathrm{V}$) among all other tested cell configurations, which leads to a total voltage loss of $V_{\mathrm{loss}} = 0.95\,\mathrm{V}$. The energetic loss accompanied by the CT–state is $\Delta E_{\mathrm{CT}} = 0.38\,\mathrm{eV}$. The voltage losses due to the

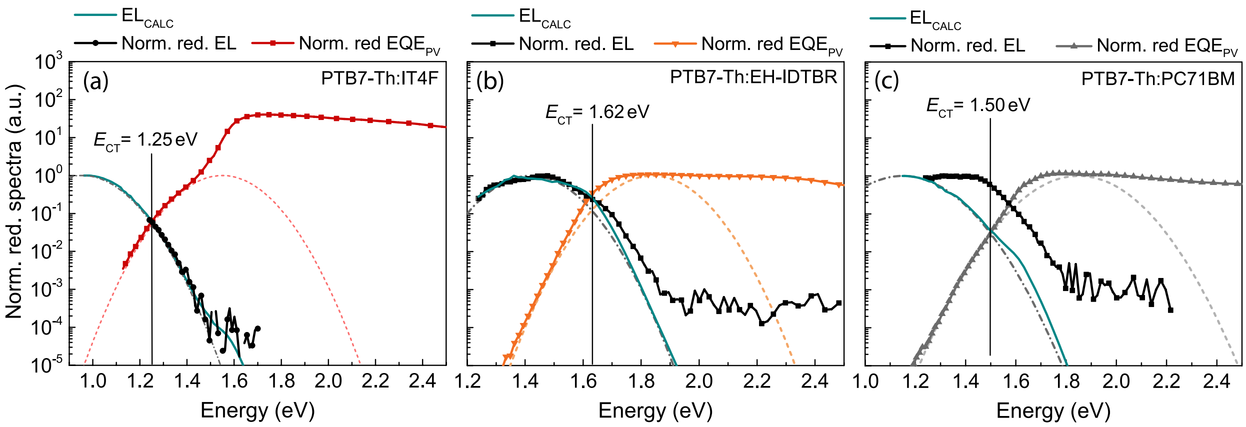

Figure 5.28: Semilogarithmic plots of the normalized and reduced EL and EQE_{PV} spectra. Dashed and dashed–dotted curves show Gaussian fits to either the reduced EL or the reduced EQE_{PV} spectra, using Eq. 2.48 and Eq. 2.47, respectively. Spectra are shown for (a) PTB7–Th:IT4F (b) PTB7–Th:EH–IDTBR and (c) PTB7–Th:PC71BM.

charge carrier recombination $\Delta V_{\text{rec}} = 0.57\,\text{V}$ is comparable to all other cell configurations. A radiative upper limit of the open–circuit voltage of $V_{\text{r}} = 1.08\,\text{V}$, determines the radiative $\Delta V_{\text{r}} = 0.17\,\text{V}$ and non–radiative $\Delta V_{\text{nr}} = 0.40\,\text{V}$ recombination losses. The relatively high ΔV_{nr} losses lead to a low EQE_{EL} of $1.9 \cdot 10^{-7}$.

The CT–state energy for the PTB7–Th:EH–IDTBR cell was found to be at $E_{\text{CT}} = 1.62\,\text{eV}$, with a $\lambda_{\text{CT}} = 0.21\,\text{eV}$. The slightly deviations of the gauss fit to the high–energy EL tail, can be attributed to the direct emission of the PTB7–Th polymer. Again, the calculated EL spectrum (bluish solid line) was used to confirm the right position of the Gauss fits. A $V_{\text{oc}} = 1.01\,\text{V}$ and an optical gap energy $\Delta E_{\text{opt,D}} = 1.63\,\text{eV}$ of the PTB7–Th polymer leads to a total voltage loss of $V_{\text{loss}} = 0.62\,\text{V}$. A low EA and IP energetic offset of the blend components (cf. Fig. 5.1), leads to a vanishing energetic CT–state difference of $\Delta E_{\text{CT}} = 0.01\,\text{eV}$. The voltage loss due to charge carrier recombination was calculated to be $\Delta V_{\text{rec}} = 0.61\,\text{V}$. This implies that nearly all of the voltage loss V_{loss} is due to charge carrier recombination. The radiative upper limit of the PTB7–Th:EH–IDTBR cell was $V_{\text{r}} = 1.29\,\text{V}$. The radiative and non–radiative recombination losses were nearly balanced and were calculated to be $\Delta V_{\text{r}} = 0.33\,\text{V}$, and $\Delta V_{\text{nr}} = 0.28\,\text{V}$, respectively. The PTB7–Th:EH–IDTBR cell revealed an EQE_{EL} of $2.0 \cdot 10^{-5}$.

The determination of the CT–state energy for the fullerene reference cell PTB7–Th:PC71BM, could also be executed using the mirror–image–theory as the EL spectra is dominated by the direct PTB7–Th polymer emission. However, the calculated EL spectrum (bluish solid line) fits well to Eq. 2.48. The crossing point was found at $E_{\text{CT}} = 1.50\,\text{eV}$ for the CT–state energy. The reorganization energy for both fits was $\lambda_{\text{CT}} = 0.35\,\text{eV}$. A total voltage loss of $V_{\mathrm{loss}} = 0.84\,\mathrm{V}$, was calculated for the PTB7–Th:PC71BM cell. The energetic CT–state difference was $\Delta E_{\mathrm{CT}} = 0.13\,\mathrm{eV}$. The voltage recombination losses were calculated as $\Delta V_{\mathrm{rec}} = 0.71\,\mathrm{V}$. With the radiative upper limit of the open–circuit voltage of $V_{\mathrm{r}} = 1.18\,\mathrm{V}$, the radiative and non–radiative recombination losses calculate to $\Delta V_{\mathrm{r}} = 0.27\,\mathrm{V}$, and $\Delta V_{\mathrm{nr}} = 0.39\,\mathrm{V}$, respectively. Again the fullerene reference PTB7–Th:PC71BM revealed a low $\mathrm{EQE}_{\mathrm{EL}}$ of $2.8 \cdot 10^{-7}$, compared to the non–fullerene cells.

The obtained values from Fig. 5.27 and Fig. 5.28 are collected in Tab. 4.

Active layer	V_{oc} (V)	E_{CT} (eV)	ΔE_{CT} (eV)	ΔV_{loss} (V)	ΔV_{rec} (V)	V_{r} (V)	ΔV_{r} (V)	ΔV_{nr} (V)	$\mathrm{EQE}_{\mathrm{EL}}$ ($\cdot 10^{-6}$)
PBDB-T-2F:IT4F	0.87	1.45	0.19	0.77	0.58	1.18	0.27	0.31	6.20
PBDB-T-2F:EH-IDTBR	1.08	1.68	0.03	0.63	0.60	1.35	0.33	0.27	29.1
PBDB-T-2F:PC71BM	0.89	1.55	0.32	0.98	0.66	1.26	0.29	0.37	0.61
PTB7-Th:IT4F	0.68	1.25	0.38	0.95	0.57	1.08	0.17	0.40	0.19
PTB7-Th:EH-IDTBR	1.01	1.62	0.01	0.62	0.61	1.29	0.33	0.28	19.8
PTB7-Th:PC71BM	0.79	1.50	0.13	0.84	0.71	1.18	0.32	0.39	0.28

Table 4: Determined CT–state energies and calculated values.

5.5.2 Discussion

Section 5.5.1 showed the determination of the voltage losses occuring within an OSC. Minimizing energy losses is a crucial task while designing BHJ solar cells. However, it is important to mention that a low total voltage loss V_{loss} does not necessarily lead to a highly efficient solar cell. High PCE requires also efficient photocurrent generation and a high FF.

While the electron transfer process for most of the cell configurations is accompanied by a ΔE_{CT} of a few hundred meV, the loss for the PTB7–Th:EH–IDTBR non–fullerene solar cell was only 10 meV. In addition, the total voltage losses were the lowest values found among all tested cell configurations. The lower loss ΔV_{loss} is largely due to the reduced energy loss ΔE_{CT} accompanied with the CT–state. ΔV_{loss} for this cell was almost fully due to charge carrier recombination.

For all tested cell configurations, the recombination losses ΔV_{rec} were around 0.6 V, which is in general, an often found value for OSCs [59]. ΔV_{rec} can be split into the radiative and non–radiative recombination channels. Except for the PTB7–Th:IT4F cell, the ΔV_{r} and ΔV_{nr} were nearly balanced.

The highest EQE_{EL} values were found for the EH–IDTBR based solar cells. During electroluminescence measurements EH–IDTBR based devices also showed the highest counts on the photodetector.

5.6 Low–temperature magneto–optical experiments

In this section, the results obtained from low temperature magneto–optical measurements are presented.

Low–temperature magneto–optical experiments were carried out using the experimental setup described in section 4.1.8. All measurements were performed at a temperature of 5 K. At this temperature, the cryostat was able to maintain a steady–state. Prior to every magnetic field measurement, a photoluminescence (PL) spectra of the excited material was measured to find the peak positions of the emission spectrum. The MFE analysis was carried out for the respective peaks in the emission spectrum.

As proof of the theoretical MFE principle discussed in section 2.8.1, an orange fluorescent acryl glass (cf. Fig. 3.4(a)), was used as a state–of–the–art reference singlet emitter. An organometallic Pt–TSPP porphyrin molecule (cf. Fig. 3.4(b)) was used as the state–of–the–art reference triplet emitter. The excitation wavelength for the Pt–TSPP porphyrin molecule was set to directly excite the Soret–band of the molecule at 405 nm, which corresponds to a photon energy of 3.06 eV. For all other materials, a 532 nm (2.33 eV) laser diode was used. The laser power at the sample was set at 5 mW. The magnetic field scan ranged from −9000 mT to +9000 mT. The measurement procedure included three scans; a so–called forward (FW) scan (from negative to positive fields), a backward (BW) scan (from positive to negative fields), and finally, again a forward scan. The presented values are the mean values of the three scans.

Fig. 5.29(a) shows the normalized PL spectrum for the orange fluorescent acryl glass singlet emitter. The PL spectrum yields 3 single peaks (P1, P2, and P3). The spectrometer was set at 1.79 eV for the first peak, at 1.95 eV for the second, and at 2.12 eV for the third peak. The resulting magnetic field effect (MFE) was calculated with Eq. 2.41. The obtained results are shown in Fig. 5.29(b). Despite a slightly noise in the signal, no clear MFE lineshape was measured for the three peaks, which can be seen in the inset. This is in close agreement with the predicted magnetic field–independence of pure singlet emitters.

In contrast, Fig. 5.30 shows the obtained results for the magnetic field–dependent triplet emitter.

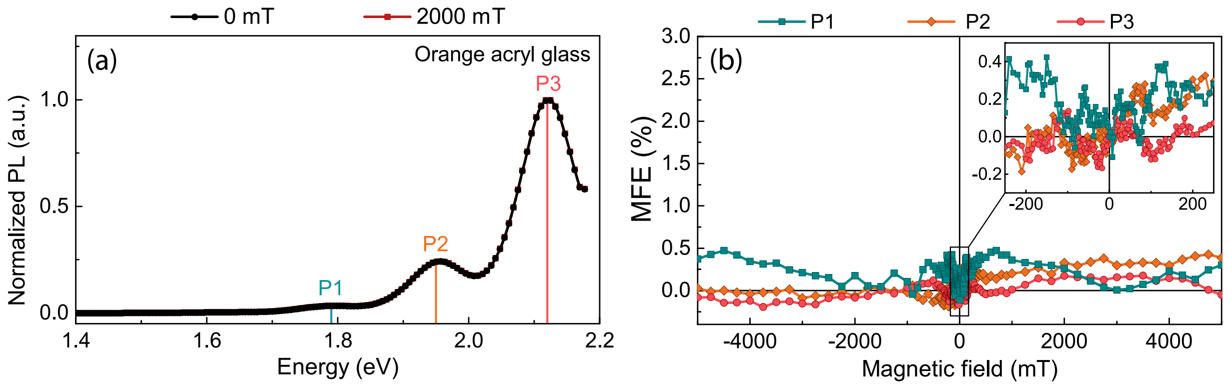

Figure 5.29: (a) Normalized PL spectra for the orange fluorescent acryl glass singlet emitter reference, at zero magnetic field and 2000 mT. (b) MFE analysis for the two respective peaks P1, P2, and P3. The inset shows a more detailed portion of the values around zero magnetic field.

The PL spectrum in Fig. 5.30(a) shows two distinct peaks at 1.64 eV (P1) , and at 1.79 eV (P2). The MFE analysis of the two peaks is shown in Fig. 5.30(b). A pronounced magnetic field–dependence of MFE= 2.25 % can be seen from zero to ±2000 mT. The heavy metal atom in the coordination center of the porphyrin molecule can induce a low magnetic field $\Delta g-$mechanism and due to the spin–orbit coupling the ISC is preferred. Therefore, the $S - T_0$ mixing is more favourable, which leads to a positive MFE. The positive MFE is even supported by the $hf-$mechanism and the short interradical distances on the molecule, leading to enhanced TTA and thus increasing the singlet ratio (see section 2.8.1). As already mentioned in the theoretical section, for organometallic complexes such as, Pt–porphyrines, the zero–field splitting is, by a factor of $10 - 100$, higher than for pure organic semiconductors [13]. Therefore, the point of inflection in Fig. 5.30(b), is shifted towards higher magnetic fields compared to the organic semiconductors used in solar cells. During the FW and BW scan, no hysteresis was detected, which can be seen at the MFE minimum at zero magnetic field strength.

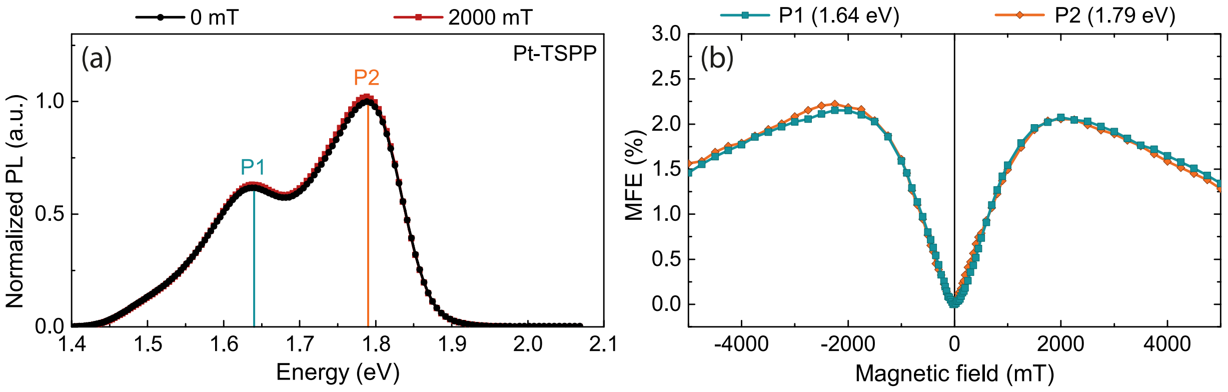

Figure 5.30: (a) Normalized PL spectra for the Pt–TSPP porphyrin triplet emitter, at zero magnetic field and 2 T. (b) MFE analysis for the two respective peaks P1 and P2.

MFE analysis for the neat organic semiconductors

The magneto–optical experiments for the organic semiconductors studied within this work, were carried out with the same measurement procedure as presented above.

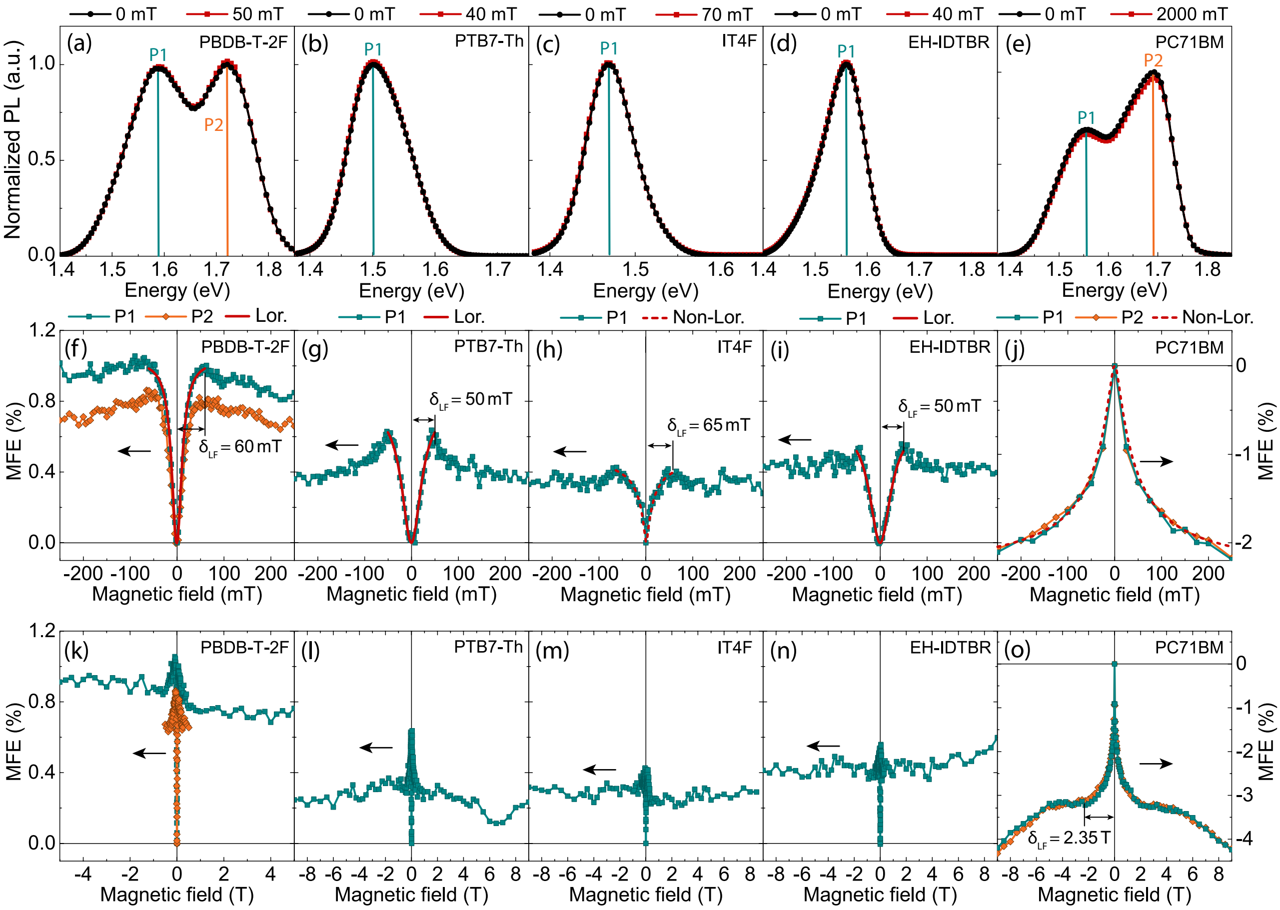

Figure 5.31: (a-e) Photoluminescence (PL) measurements for the neat organic semiconductor materials. PL plots are shown at zero external magnetic field and the magnetic field at the corresponding point of inflection of the MFE–analysis, below the PL plots. (f-j) MFE analysis of the neat organic semiconductor materials. The colors correspond to the respective PL peak. (k-o) MFE–analysis for the same values as in (f-j) on a wide external magnetic field scale.

Fig. 5.31(a-e) show the PL measurements for the neat organic semiconductor materials. In every independent plot, the peaks are indicated with vertical straight lines, and labeled with P1 and P2, respectively. The amount of shown points was reduced by a factor of three. The PBDB–T–2F donor polymer (a) and the PC71BM fullerene acceptor (e) show two distinct peaks. The PTB7–Th polymer (b), and the IT4F (c) and EH–IDTBR (d) small molecule acceptor exhibited a single peak over the shown spectral range. PL plots are shown for zero external magnetic field (black–circles) and for the magnetic field (red–squares) corresponding to the point of inflection in the MFE analysis below (f-j). No spectral shift of the individual PL peaks was observed, during the magnetic field scan.

A detailed MFE–analysis from ±250 mT is shown in Fig. 5.31(f-g). It shall be noted that the presented values in (f-i) and (k-n) belong to the left vertical axis, whereas the PC71BM (j) and (o) values correspond to the right vertical axis. The presented MFE lineshapes closely resamble the predicted shape shown in Fig. 2.17(c). The MFE of the materials PBDB–T–2F (f), PTB7–Th (g), and EH–IDTBR (i) can be fitted with Eq. 2.42, which resambles a lorentzian lineshape (red solid line). The IT4F small molecule acceptor (h), as well as the PC71BM fullerene acceptor (j) revealed a non–lorentzian line shape (red dashed line) which can be fitted with Eq. 2.43). For the materials shown in (f-i), a low external magnetic field leads to a positive MFE. The PC71BM fullerene acceptor material, shown in (j), exhibits a negative MFE over a wide magnetic field range. The points of inflection are indicated with δ_{LF}, where LF abbreciates low–field. All materials shown in (f-i) revealed a point of inflection in the range of 50 to 65 mT. The PC71BM material shown in (j), exhibits a first MFE saturation at $\delta_{\mathrm{LF}} = 2.35\,\mathrm{T}$. During the magnetic field scans, no hysteresis was detected. The MFE curves for external magnetic fields $> 250\,\mathrm{mT}$ are shown in Fig. 5.31(k-o). For all materials except PC71BM, the MFE saturates and remained constant for magnetic fields $> \pm 250\,\mathrm{mT}$. It can be clearly seen that the PC71BM fullerene exhibits the highest value for δ_{LF} and a second negative MFE feature at high magnetic fields, starting at ±5 T.

MFE analysis for the donor:acceptor blends

The magneto–optical experiments were also carried out for the same donor:acceptor blend configurations studied in the previous sections. The w/w ratios of the individual blends were chosen exactly as for the configuration with the best PCE.

Fig. 5.32 shows the MFE analysis for the PBDB–T–2F based OSCs. The PL measurements of the different blends are shown in (a-c). The PBDB–T–2F:IT4F (a) with a 1:1 (w/w) ratio exhibited three PL peaks P1, P2, and P3, respectively. The curves are indicated with D:A blend for the donor:acceptor blended film, and neat D and A for the neat donor and acceptor films, respectively. In addition to the blend PL spectrum, the neat PL curves of the PBDB–T–2F and the IT4F are shown. Upon blending the polymer with the acceptor, the low–energy peak of the polymer shifts towards lower energies, and the IT4F peak shifts towards higher energies. These shifts are indicated by the small colored arrows and are believed to stem from the change in the refractive index during the formation of the BHJ.

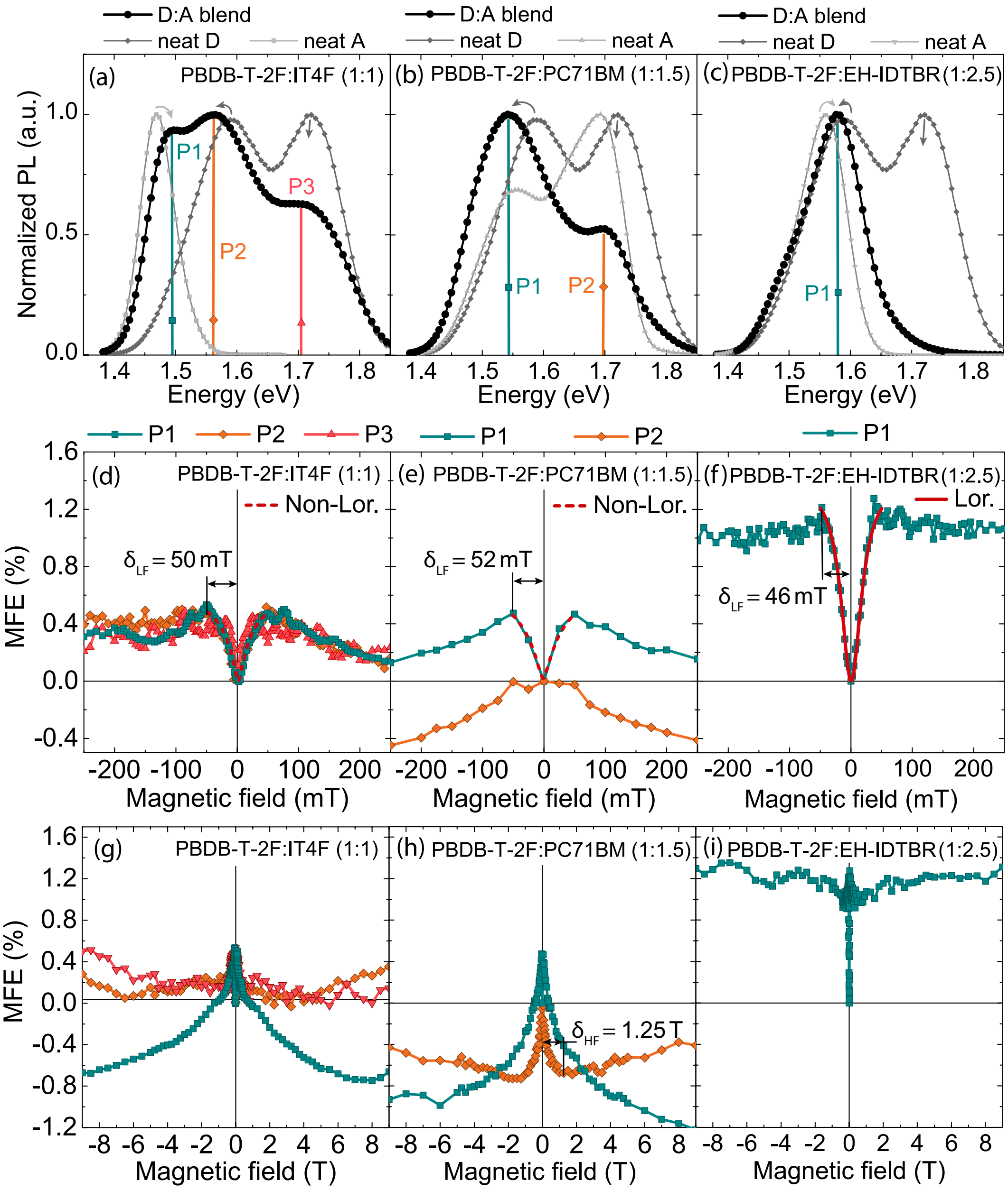

Figure 5.32: (a-c) Photoluminescence (PL) measurements for the PBDB–T–2F:acceptor blends. PL plots are shown at zero external magnetic field. The curves are indicated with D:A blend for the donor:acceptor blended film, and neat D and A for the neat donor and acceptor films, respectively. (d-f) MFE analysis of the PBDB–T–2F based blends. The colors correspond to the respective PL peak. (g-i) MFE–analysis for the same values as in (d–f) on a wide external magnetic field scale.

The corresponding MFE analysis of the individual peaks is shown below in (d). The lineshape of the low–field process can be fitted with a non–lorentzian curve (Eq. 2.43). The MFE curves revealed a point of inflection at $\delta_{\text{LF}} = 50\,\text{mT}$ with a maximum MFE of 0.5 %. The same MFE values as shown in (d) are presented in (g) on a wide magnetic field range. As can be seen, peak P2 and P3 are saturated for magnetic fields $> 250\,\text{mT}$. The high–field analysis of the peak P1, which can be attributed to the IT4F PL emission, exhibited a negative MFE that starts to saturate at around ±9 T. No hysteresis of the MFE was observed during the measurement.

The PL measurements for the PBDB–T–2F:PC71BM 1:1.5 (w/w) ratio fullerene reference blend configuration is shown in Fig. 5.32(b). Upon blending the polymer with the fullerene acceptor (black–circles) the PL emssions of the neat materials mix and result in two peaks P1 and P2, respectively. The MFE analysis of the respective two emissive transitions is shown below in (e). The MFE curve for peak P1 revealed a point of inflection at $\delta_{\mathrm{LF}} = 52\,\mathrm{mT}$ and with a maximum MFE of 0.5 %. A non–Lorentzian line shape (Eq. 2.43) could be fitted to the low–field MFE values. The positive MFE may stem from the neat PBDB–T–2F emission and the corresponding positive MFE (cf. Fig. 5.31(f)). A constant low–field (±50 mT) MFE was found for the PL peak P2. Here, it is assumed that positive and negative MFE processes compete and are balanced. Fig. 5.32(h) shows the same values as in (e) on a larger magnetic field scale. As shown in Fig. 5.31(j), the MFE effect for the neat PC71BM is purely negative. Similar behavior was found for the D:A blend. The blend MFE shows a suppressed saturated maximum of −0.8 % at a magnetic field of 9 T, which is in contrast to the maximum saturated MFE for the neat PC71BM of −4 % at 9 T. The MFE analysis of the PL peak P2 revealed a high–field point of inflection at $\delta_{\mathrm{HF}} = 1.25\,\mathrm{T}$, with a maximum MFE of −0.75 %. Again no magnetic hysteresis was detected.

The PBDB–T–2F polymer was also blended with the EH–IDTBR non–fullerene acceptor with a 1:2.5 (w/w) ratio. The observed PL measurements are shown in Fig. 5.32(c). The measurement reveals a single PL peak P1. The formation of the BHJ seems to either quench or cover the high–energy peak of the PBDB–T–2F polymer. The corresponding MFE analysis is shown below in (f). A point of inflection was observed at $\delta_{\mathrm{LF}} = 46\,\mathrm{mT}$ with a maximum MFE of 1.2 %. The low–field lineshape could be fitted with a Lorentzian equation (Eq. 2.42). Fig. 5.32(i) presents the observed MFE values on a large magnetic field scale. The MFE showed only positive values over the full measured magnetic spectrum, and it was saturated and remained constant for magnetic fields $> 2\,\mathrm{T}$. The observed MFE lineshapes were symmetrical along the vertical axis.

The magneto–optical measurements were also carried out for the three different acceptors in combination with the PTB7–Th polymer. Blend ratios were chosen as the cell configurtaion with the best PCE presented in section 5.2.1.

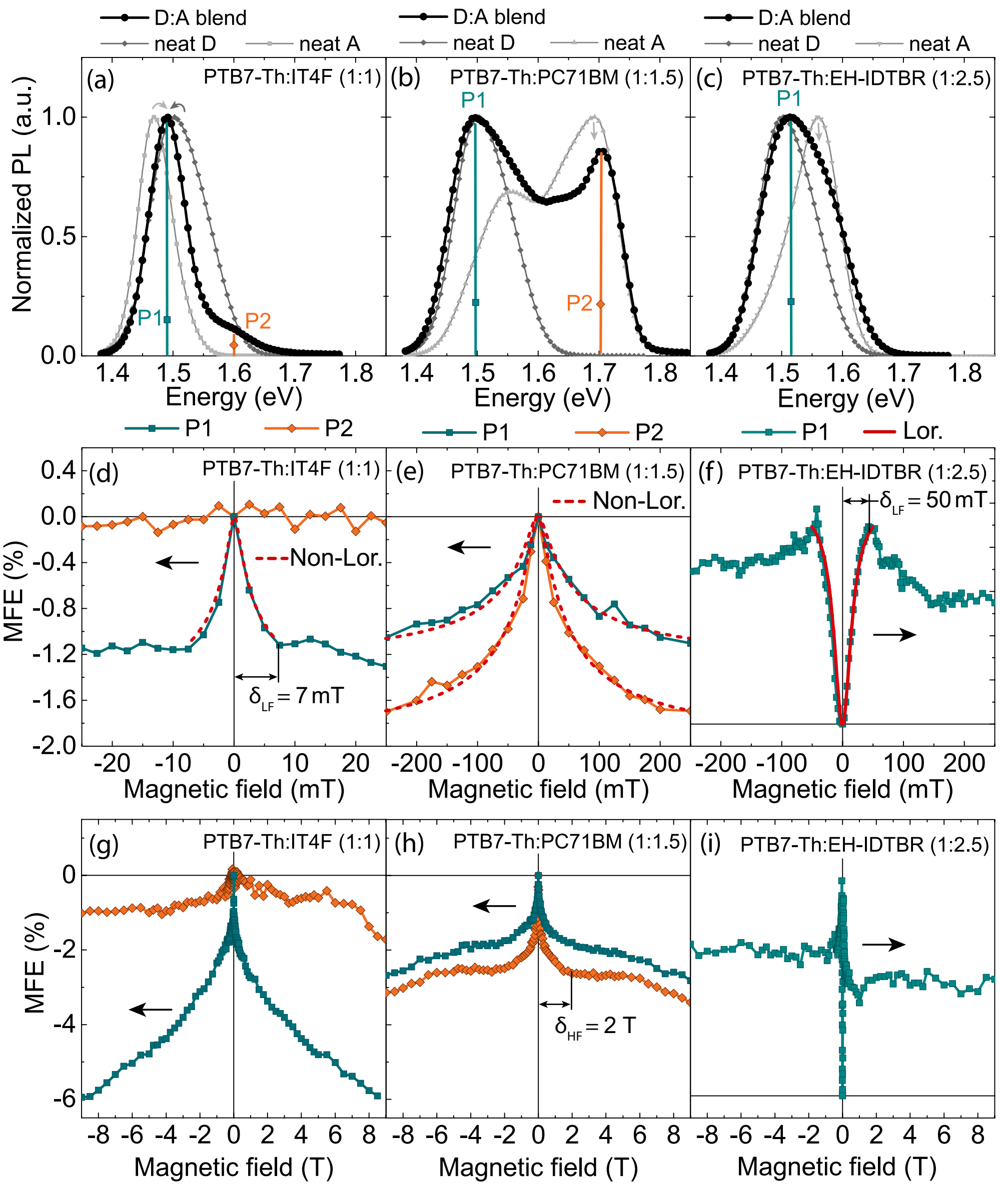

Figure 5.33: (a-c) Photoluminescence (PL) measurements for the PTB7–Th:acceptor blends. PL plots are shown at zero external magnetic field and the magnetic field. The curves are indicated with D:A blend for the donor:acceptor blended film, and neat D and A for the neat donor and acceptor films, respectively. (d-f) MFE analysis of the PTB7–Th based blends. The colors correspond to the respective PL peak. (g-i) MFE–analysis for the same values as in (d–f) on a wide external magnetic field scale. Note, values shown in (f) and (i) belong to the right vertical axis.

Fig. 5.33(a) shows the observed photoluminescence for the PTB7–Th:IT4F 1:1 (w/w) ratio solar cell (black–circles) and the neat donor (grey–diamonds) and acceptor (light grey–squares) PL spectra. The formation of the BHJ leads to a peak P1 and a smaller second peak P2 at higher energies. The peaks are marked with vertical lines. The MFE analysis of both peaks are shown below in (d). The MFE curve shows a very small low–field non–lorentzian lineshape with a point of inflection at $\delta_{\mathrm{LF}} = 7\,\mathrm{mT}$. It is noteworthy to mention that no neat component shows a negative MFE (see Fig. 5.31(g,h)). The wide magnetic field scan shown in (g), revealed a very strong MFE for peak P1 of $-6\,\%$ at $\pm 9\,\mathrm{T}$. The MFE analysis of PL peak P2 shows also a negative feature that saturates at around $\pm 3\,\mathrm{T}$ with a maximum MFE of $-1\,\%$ at $\pm 9\,\mathrm{T}$.

The PL measurement for the fullerener reference sample PTB7–Th:PC71BM 1:1.5 (w/w) ratio is shown in Fig. 5.33(b). The neat donor and acceptor PL spectra sum up to a PL spectrum with two main peaks P1 and P2, respectively. The corresponding low–field MFE analysis is shown in (e). Both peaks revealed a purely negative non–Lorentzian MFE lineshape. The MFE analysis on a wide magnetic field scale is presented in (h). Both MFE curves exhibit a high–field point of inflection at around $\delta_{\mathrm{HF}} = \pm 2\,\mathrm{T}$, where the MFE starts to saturate. A second negative high–field MFE could be observed for magnetic fields $> \pm 6\,\mathrm{T}$.

The PL measurement for the PTB7-Th based solar cell with the EH–IDTBR small molecule acceptor in a 1:2.5 (w/w) ratio, is presented in Fig. 5.33(c). The plot shows the D:A blend PL spectrum as well as the neat donor and acceptor spectra. The formation of the BHJ leads to the summation of both neat donor and acceptor PL spectra. No energetic shifts of the individual peaks were observed. The MFE analysis of the PL peak P1 is shown below in (f). The low–field MFE lineshape could be fitted with a Lorentzian equation and has a point of inflection at $\delta_{\mathrm{LF}} = 50\,\mathrm{mT}$ with a maximum MFE of $1.8\,\%$. After an external magnetic field of around $\pm 1\,\mathrm{T}$, the MFE started to saturate.

The organic semiconductors were also investigated with donor:accpetor blend ratios of 1:0.01 (w/w). Here, the interpenetrating structure (cf. Fig. 2.3(a)) is not fully evolved as the mixtures ratios are below the percolation limit. Fig. 5.34(a-c) shows photoluminescence measurement of the blends. In most of the shown PL measurements, the spectra are mainly determined by the polymer emission. Except, for the PBDB–T–2F:PC71BM a 1:0.1 (w/w) ratio led to a compareable spectrum as for the 1:1.5 (w/w) ratio (Fig. 5.32(b)).

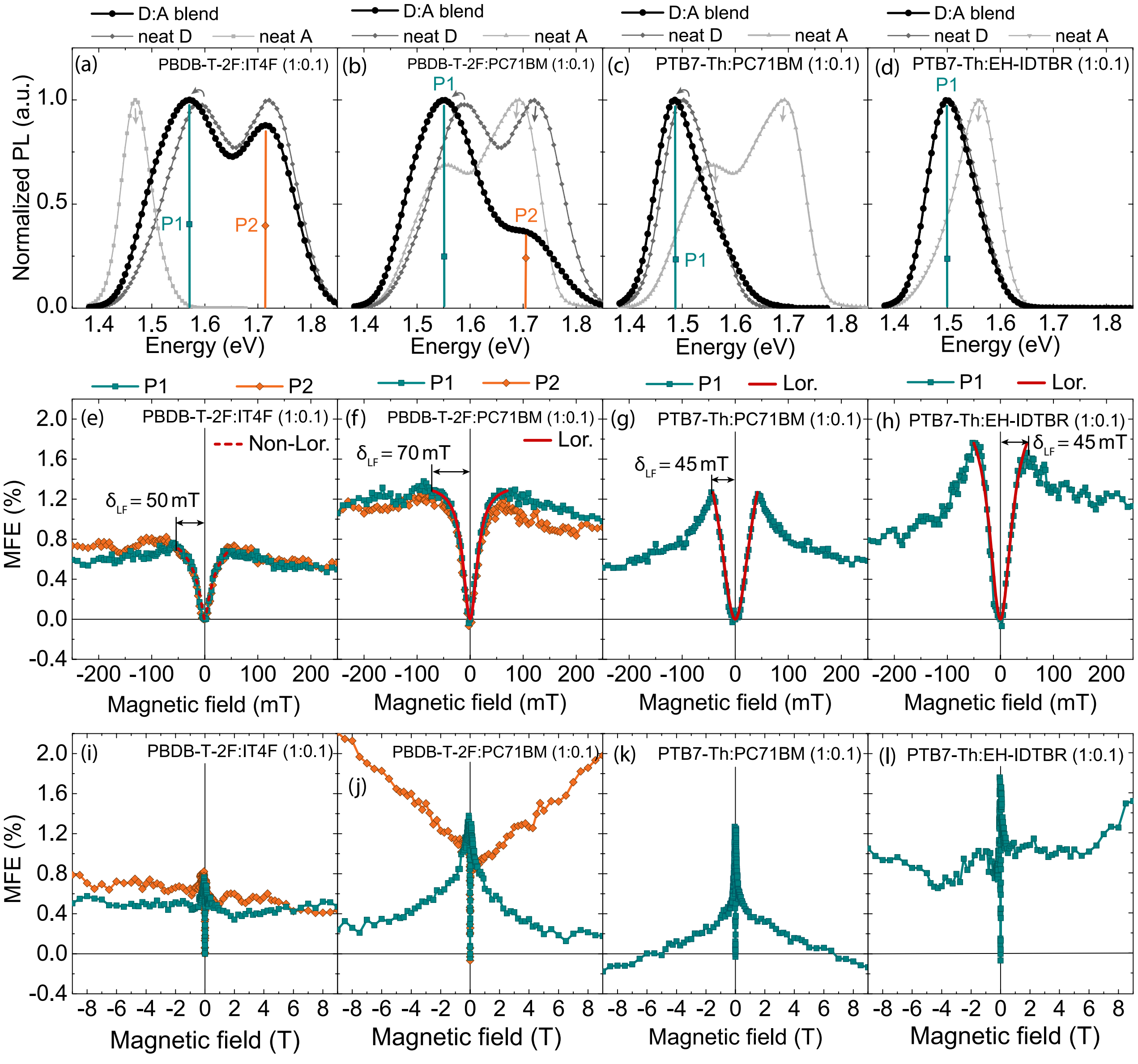

Figure 5.34: (a-d) Photoluminescence (PL) measurements for the PBDB–T–2F:acceptor 1:0.1 (w/w), and PTB7–Th:acceptor 1:0.1 (w/w) ratio blends. PL plots are shown at zero external magnetic field and the magnetic field at the corresponding point of inflection of the MFE–analysis, below the PL plots. (e-h) MFE analysis of the respective blends. The colors correspond to the PL peaks. (i,l) MFE–analysis for the same values as in (e-h) on a wide external magnetic field scale.

5.6.1 Discussion

The MFE measurements for the studied neat organic semiconductors and blend configurations showed that a small external magnetic field ($\sim 50\,\mathrm{mT}$) can effectively change the photoluminescence of the material. This a clear sign for a magnetic response from non-magnetic organic materials. The observed lineshapes of the MFE were in close aggreement with the predicted Lorentzian and non–Lorentzian shapes discussed in the theoretical section 2.8.1. All neat materials, except the fullerene reference PC71BM, revealed a positive low–field MFE. Interestingly, it was found that blending the IT4F non–fullerene acceptor with a donor polymer leads to a sign change of the MFE. The most striking difference between the fullerene and non–fullerene blends is the magnetic field strength position of the point of inflection. Whereas, a low–field δ_{LF} of $\sim 50\,\mathrm{mT}$ was found for the non–fullerene blends a high–field point of inflection δ_{HF} of $\sim 1.25\,\mathrm{T}$ was found for fullerene blends. As discussed in the theoretical section 2.8.1, a point of inflection in the MFE lineshape can be attributed to a low spin–exchange energy ΔE_{ST} which strongly depends on the interradical distance. Therefore, it can be expected that in polymer:fullerene blends the interradical distances are shorter, and thus the ΔE_{ST} is higher compared to non–fullerene blends.

5.7 Flexible organic solar cells with non–fullerene acceptors

In this section the results obtained for the flexible OSCs are presented. The device fabrication of the individual samples is discussed in section 4.4.

5.7.1 Optical characterization of the transparent electrodes

The optical characterization of the flexible substrates was carried out with the experimental setup discussed in section 4.1.1. All flexible substrates were measured with the transparent electrode and on the solid support.

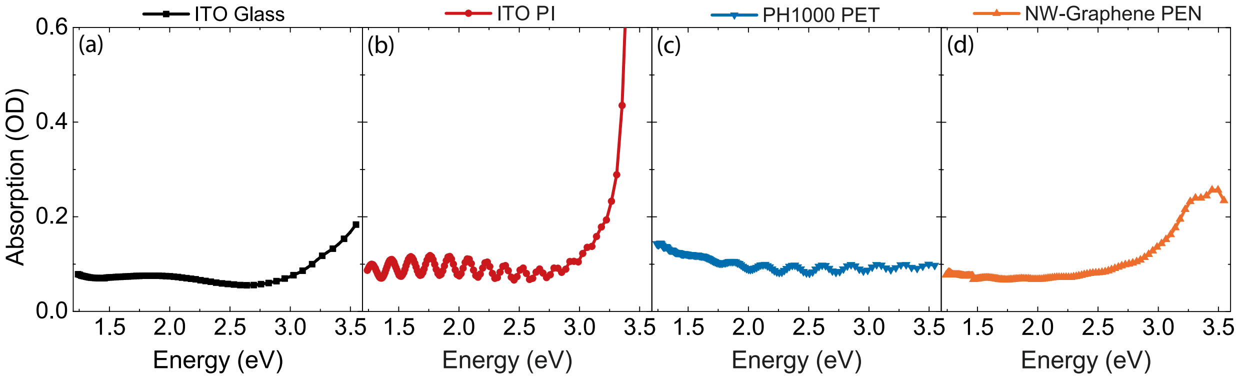

Figure 5.35: Absorption spectra of flexible substrates with the respective transparent electrodes compared to an ITO electrode on glass. (a) ITO–Glass substrate, (b) ITO–PI substrate (section 4.4.2), (c) PEDOT:PSS PH1000–PET substrate (section 4.4.1), (d) NW graphene–PEN substrate (section 4.4.3).

Fig. 5.35 shows the absorption measurements of the solid ITO–Glass substrate (a) compared to the different flexible substrated (b-d). The optical density in the NIR–Vis spectral region is nearly equal for all the substrates. The ITO PI substrate (b) shows a significant increase of the optical density for high energies. The sinusoidal shape of the curve is mainly due to interference effects of the transmitted light due to the additional substrate layers as compared to the bare ITO samples. The PH1000–PET substrate (c) exhibited flat absorption over a wide spectral region. As the thickness of the PET substrate is comparable to the PI foil the absorption spectrum also shows an interference pattern. The NW–graphene PEN substrate (d) shows an increase of the optical density for higher energies.

5.7.2 Sheet resistance of the transparent electrodes

The electrical conductivity of the transparent electrode is as important as the ability to allow light to pass through it. The conductivity of the electrodes was determined in terms of the sheet–resistance with the four–wire probe method (see section 4.1.9).

First, the ITO–Glass reference showed a sheet–resistance of 15 Ω□. The ITO transparent electrode on the PI substrate showed a sheet–resistance of 35 Ω□, which can be mainly attributed to the lower thickness (100 nm) of the sputtered ITO layer compared to the ITO on glass (150 nm). The PH1000–PET transparent electrode showed a considerably higher sheet–resistance of 105 Ω□. The NW graphene electrode on the PEN flexible substrate revealed a sheet–resistance of 125 Ω□.

5.7.3 Surface profile characterization

Atomic force microscopy (AFM) was used to investigate the surface profile and the structural influences of the transparent electrodes on the active layer film formation for the different flexible substrates. An ITO transparent electrode on glass was used as a solid reference substrate.

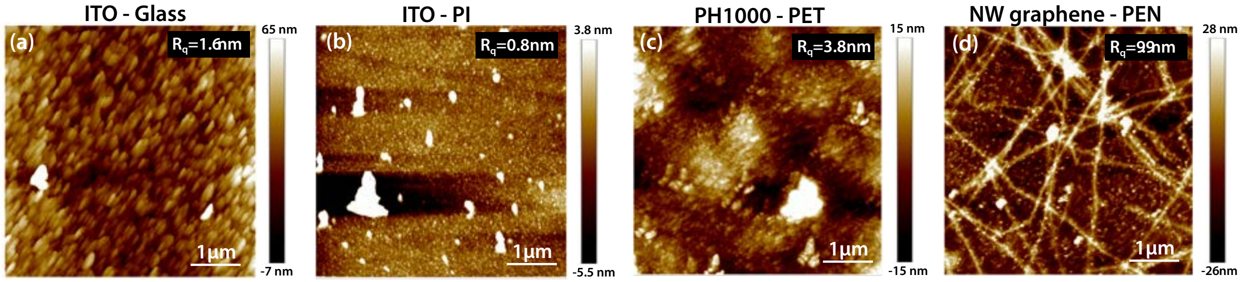

Figure 5.36: AFM pictures of the (a) ITO–Glass substrate, (b) ITO–PI substrate (section 4.4.2), (c) PEDOT:PSS PH1000 PET substrate (section 4.4.1), (d) NW graphene–PEN substrate (section 4.4.3).

The resulting AFM pictures are shown in Fig. 5.36. A $5 \times 5\,\mu$m AFM picture of an ITO transparent electrode on a glass substrate is depicted in (a). The bare ITO showed a small–vertical–grain morphology with a surface roughness of $R_\mathrm{q} = 1.6$ nm.

Fig. 5.36(b) shows the ITO surface profile on the PI flexible substrate described in section 4.4.2. The surface shows an even smaller vertical–grain morphology than the solid counterpart in (a). The surface roughness is $R_\mathrm{q} = 0.8$ nm. Since the flexible substrate cannot be cleaned as well as the rigid one, they typically show more dirt particles (white fragments in the AFM picture) on the surface, which can negatively affect the formation of solar cell films, during device fabrication. The surface roughness was determined for areas without dirt particles.

Fig. 5.36(c) shows the surface profile of the PEDOT:PSS PH1000 electrode on the ultrathin PET foil described in section 4.4.1. A R_q value of 3.8 nm was measured for the surface.

Fig. 5.36(d) depicts the surface profile of the NW graphene–PEN flexible substrate. The Ag NW–network with diameters ranging from 50 to 80 nm, can be clearly identified on the surface. A relatively high R_q value of 9.9 nm was measured.

5.7.4 Current–density $j(V)-$ measurements

The photovoltaic performance of the flexible OSCs with non–fullerene acceptors was investigated using standardized current–density measurements in a solar–simulatior (see section 4.1.2). Flexible solar cells were are presented with the PBDB–T–2F:IT4F active layer blend, as they exhibited the highest efficiencies on the rigid substrates (compare section 5.2.1). The solar cells were measured under simulated 100 mW $\cdot$ cm^{-2} AM1.5 solar illumination, and under dark conditions. The solar cell pixel area was determined with a digital microscope.

ITO–PI flexible solar cells

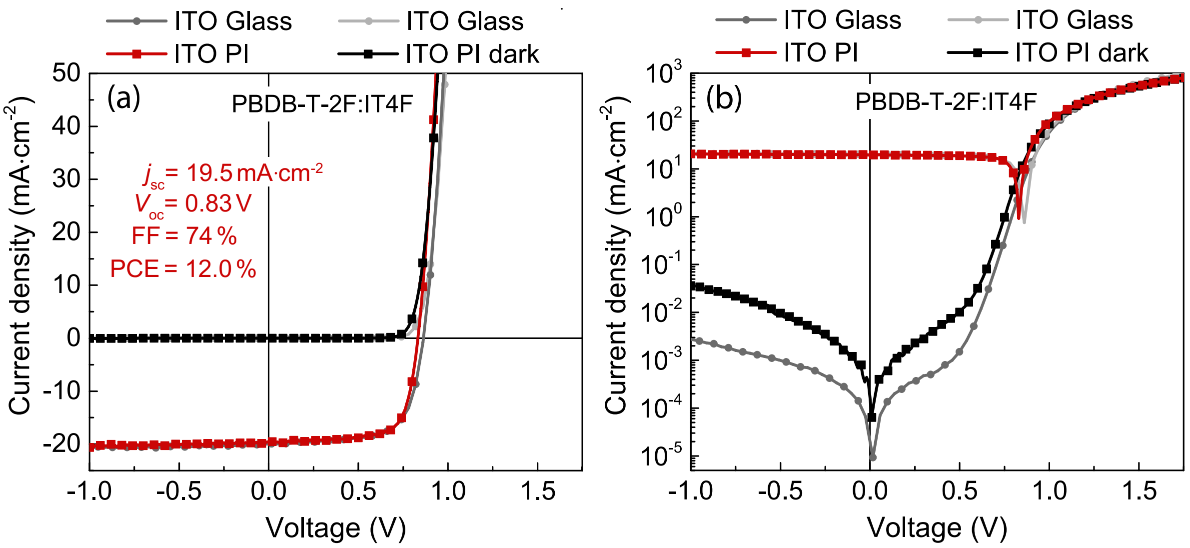

Figure 5.37: $j(V)$–curves for the ITO–PI flexible OSCs under simulated 100 mW $\cdot$ cm^{-2} AM1.5 solar illumination and under dark conditions for (a) PBDB–T–2F:IT4F 1:1 (w/w) linear $j(V)$–curves, and (b) semilogarithmic $j(V)$–curves. (c) PTB7–Th:EH–IDTBR 1:2.5 (w/w) linear $j(V)$–curves, and (d) semilogarithmic $j(V)$–curves.

Flexible OSCs were fabricated on ultrathin ITO–PI substrates. The solar cell fabrication is discussed in section 4.4.2.

Fig. 5.37(a) shows the $j(V)-$ measurements for the PBDB–T–2F:IT4F based devices on the ITO–PI flexible substrates. The correpsonding solar cell parameters are written in the plot and summarized in Tab.5. The $j(V)-$ curves were compared to the reference ITO–Glass (compare Fig. 5.4(a)) samples (grey–circles). The rigid ITO–Glass solar cell showed an average PCE of 12.2 %. The flexible solar cell exhibited an average PCE of 12.0 % with a $V_{\mathrm{oc}} = 0.83\,\mathrm{V}$ and a $j_{\mathrm{sc}} = 19.5\,\mathrm{mA} \cdot \mathrm{cm}^{-2}$. The measured FF of 74 % was the highest measured value among all tested cell types. It can be assumed that the smoother ITO surface of the PI substrate leads to better active layer film formation, which explains a higher FF.

The semilogarithmic representations of the $j(V)$–curves are shown in Fig. 5.37(b). The solar cell on the ITO–PI flexible substrate exhibited a higher dark leakage current–density and a lower shunt–resistance R_{p} than for the ITO–Glass substrate.

PH1000–PET flexible solar cells

The photovoltaic properties of the PEDOT:PSS PH1000–PET based ultrathin flexible solar cells were investigated with the PBDB–T–2F:IT4F active layer material. The device fabrication is discussed in section 4.4.1.

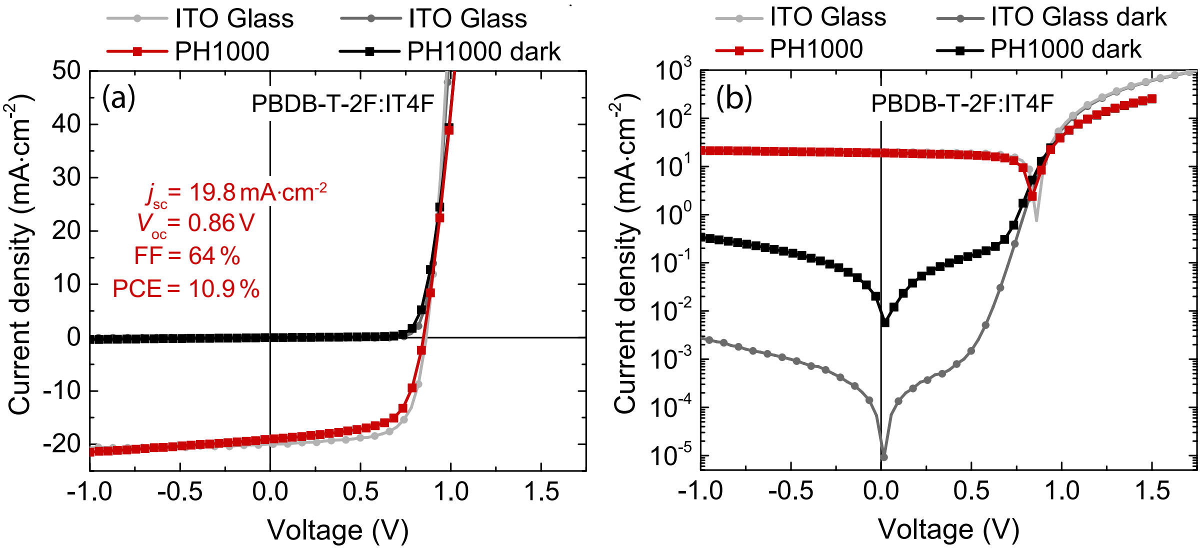

Figure 5.38: $j(V)$–curves for the PH1000–PET flexible OSCs under simulated $100\,\mathrm{mW} \cdot \mathrm{cm}^{-2}$ AM1.5 solar illumination and under dark conditions for (a) PBDB–T–2F:IT4F linear $j(V)$–curves, and (b) semilogarithmic $j(V)$–curves.

Fig. 5.38 shows the observed $j(V)$–curves of the flexible cells (red–squares) compared to the ITO on glass reference devices (grey–circles). The PH1000–PET PBDB–T–2F:IT4F solar cells shown in (a) exhibited a PCE of 10.9 % with a V_{oc} of 0.86 V, a j_{sc} of $19.8\,\mathrm{mA} \cdot \mathrm{cm}^{-2}$, and a FF of 64 %. The lower FF can be mainly attributed to the influence of the parasitic resistances and the higher surface roughness of the transparent electrode (Fig. 5.36). The series resistor R_{s} of the PH1000–PET cell is higher than for the rigid reference as can be seen at the slightly lower slope of the $j(V)$–curve around V_{oc} (compare section 2.6). The PH1000–PET shows a comparable shunt–resistance R_{p} to the rigid ITO–Glass device. It can be seen at the parallelity of the dark $j(V)$–curves in the negative bias region of the semilogarithmic representation shown in Fig. 5.38(b). The dark leakage current–density of the PH1000 device is three orders of magnitude higher than for the rigid ITO cell.

NW Graphene–PEN flexible solar cells

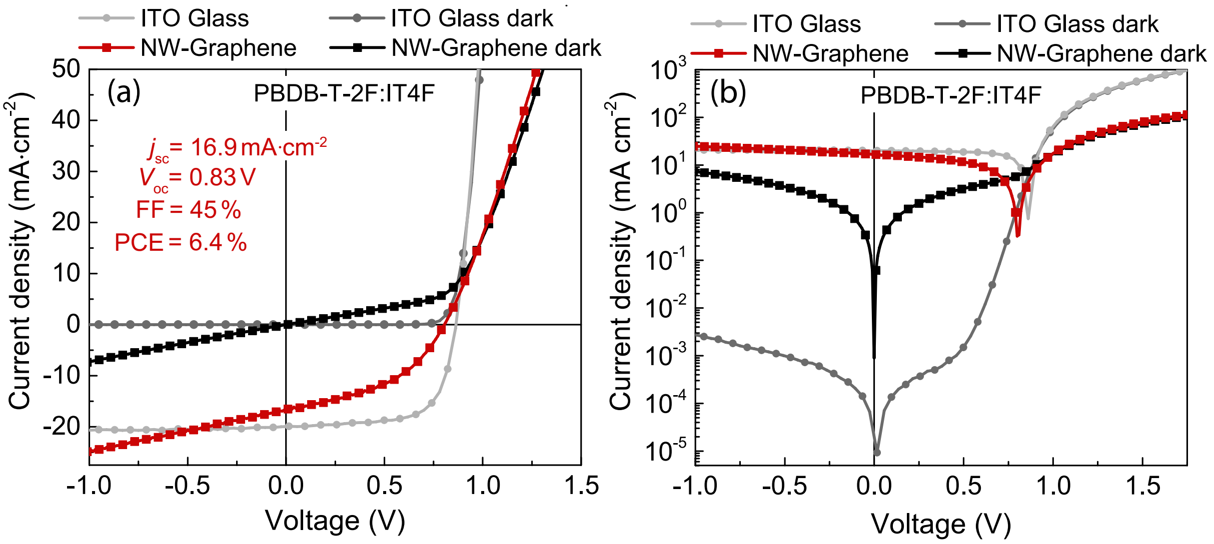

Figure 5.39: $j(V)$–curves for the NW Graphene–PEN flexible OSCs under simulated $100\,\mathrm{mW} \cdot \mathrm{cm}^{-2}$ AM1.5 solar illumination and under dark conditions for (a) PBDB–T–2F:IT4F 1:1 (w/w) linear $j(V)$–curves, and (b) semilogarithmic $j(V)$–curves.

The photovoltaic performance of the Ag NW Graphene–PEN flexible substrate was tested with the PBDB–T–2F:IT4F active layer blend. The obtained $j(V)$–curves from the sun–simulator are shown in Fig. 5.39. The device showed PCE of 6.4 % with a V_{oc} of 0.83 V, a j_{sc} of $16.9\,\mathrm{mA} \cdot \mathrm{cm}^{-2}$, and a FF of 45 %. The low device parameters of the NW graphene–PEN substrate can be attributed to the high sheet–resistance and surface–roughness of the transparent electrode. The influence of the parasitic resistances can be clearly seen at the slope of the $j(V)$–curve (red–squares) at V_{oc} and j_{sc} (compare section 2.6). In the semilogarithmic representation shown in (b) one can see that the dark leakage–current density of the NW graphene–PEN based solar cell is orders of magnitude higher than for the ITO–Glass reference.

The presented device parameters in Tab. 5 showed that flexible solar cells based on ITO–free transparent electrodes achieve comparable photovoltaic performances to their rigid counterparts. The most promising ITO–free device was demonstrated based on the ultrathin PH1000–PET substrate. It may be likely that the lower PCE of the NW–Graphene substrates is mainly due to the used inverted cell configuration. It is assumed that the ZnO ETL layer does not cover the electrode uniformly, which could be one reason for the high dark

Active layer	$V_{\text{oc}}(V)$ (± 0.01)	$j_{\text{sc}}(mA \cdot cm^{-2})$ (± 0.2)	FF(%) (± 0.1)	PCE(%)(max.)
PBDB-T-2F:IT4F				
ITO Glass	0.87	20.1	70	12.2 (12.7)
ITO PI	0.83	19.5	74	12.0 (12.2)
PH1000 PET	0.86	19.8	64	10.9 (11.1)
NW–Graphene PEN	0.83	16.9	45	6.4 (6.4)

Table 5: Solar–cell parameters for the different flexible substrates. PCE values written in parentheses are the highest obtained numbers across several pixels.

leakage current. Further investigations will concentrate on the device fabrication with the standard device configuration and the incorporation of a thicker PEDOT:PSS HTL interlayer to overcome these deficiencies.

6 Conclusion and outlook

A range of complimentary steady state and frequency domain techniques have been used to study non–fullerene and fullerene based OSCs. Two different polymers PBDB–T–2F and PTB7–Th were blended with the non–fullerene small molecule acceptors IT4F and EH–IDTBR. The fullerene molecule PC71BM was used as a state–of–the–art reference to study the differences between the two acceptor types.

The fabricated PBDB–T–2F:IT4F OSCs on ITO–Glass showed a PCE of up to 12.7 % with an EQE of 83 %. The respective PBDB–T–2F:PC71BM fullerene reference exhibited a peak PCE of 6.9 % with an EQE of 73 %. The solar cells based on the PTB7–Th:EH–IDTBR showed PCE of up to 9.8 % with again 83 % EQE. The PTB7–Th:PC71BM fullerene reference revealed a peak PCE of 4.8 % with an EQE of 70 %. The obtained efficiencies and device parameters are comparable to the literature [71, 79]. Solar cells based on non–fullerene acceptors showed significantly larger j_{sc} and FF compared to their fullerene counterparts. It has also been shown that active layer combinations with zero to vanishing ionization potential, such as PBDB–T–2F:EH–IDTBR, lead to an overall bad photovoltaic performance. The EQE measurements also backed the findings from the $j(V)$–curve measurements. The calculated j_{sc} from the EQE response showed that the device area of the cells was not underestimated during the solar–simulator device characterization.

The ideality factors m_{voc} were derived from the intensity dependence of the open–circuit voltage V_{oc}. In addition, the ideality factors m_{Hrec} were determined from the open–circuit voltage dependent recombination impedance H_{rec}. All solar cells revealed ideality factors between 1 and 1.5, This leads to the assumption, that both carrier recombination in the depletion zone of the bulk–heterojunction, and diffusion current processes are present. IMVS measurements at varying DC light intensities were performed, to get further insights into the charge recombination dynamics within the solar cell. All device configurations exhibited effective electron lifetimes in the range of 0.6 to 2.1 μs. The presented measurement method has the potential to easily determine the open circuit recombination dynamics in OSCs. Additional work is in progress to increase the donor:acceptor database in a standardized measurement procedure.

Steady–state stability measurements by MPP tracking were performed to test the photovoltaic performance of the non–fullerne based solar cells under ambient conditions. The presented study showed that PBDB–T–2F:IT4F based solar cells are highly susceptible to ambient air. Improving the stability of the devices under real ambient conditions is therefore a central topic for future studies.

Section 5.5.1 provides a straight forward method and analysis to determine voltage losses in organic semiconductors. The shown evaluation procedure can determine the bandgap energy of neat organic semiconductors and donor–acceptor blends directly from the measurements of the complete device. In all devices, the total open–circuit voltage loss due to recombination processes (ΔV_{rec}) is very similar ($\sim 0.6\,\mathrm{eV}$). However, the highest V_{rec}–values were obtained for fullerene based devices. It turned out that a high driving force for charge–separation (ΔE_{CT}) does not necessarily lead to high j_{sc} or V_{oc} values, as demonstrated by the PTB7–Th:IT4F active layer blend. However, more tests with different donor:acceptor combinations would be necessary to develope particular solar cell design rules based on the presented findings.

In section 5.6, the magnetic field dependence of the photoluminescence from the organic semiconductors was studied at low–temperature conditions. It has been shown that a small external magnetic field ($\sim 50\,\mathrm{mT}$) can effectively change the photoluminescence of a nonmagnetic organic material. The observed MFE lineshape could be addressed to the underlying magnetic field dependent physical processes. The measurements revealed that the spin–mixing processes, such as ISC and TTA are enhanced or suppressed by an external magnetic field. Taken together, the findings suggest that in polymer:fullerene blends the interradical distances are shorter, and thus the spin–exchange energy is higher compared to non–fullerene blends.

Flexible OSCs were fabricated to demonstrate the tremendous applicability and processibility of organic semiconductors. The device fabrication technique developed in this thesis offers an ideal platform for the production of flexible solar cells with any desired organic absorber material. The steady–state photovoltaic performance of three different flexible substrates were compared to a rigid ITO–Glass reference substrate. The obtained results showed that OSCs can be succesfully fabricated on ITO and ITO–free ultrathin flexible substrates. The best photovoltaic performance was shown by the ultrathin ITO–PI based flexible cell. The demonstrated ITO–PI flexible substrates showed a peak PCE of up to 12.2 %, which is comparable to the rigid ITO–Glass reference. Devices based on ultrathin PH1000–PET foils showed nearly equal PCE (11.2 %) as the ITO–PI flexible cells, and are, therefore, promising candidates towards ITO–free flexible solar cells. Devices with a NW–Graphene transparent electrode exhibited a PCE of up to 6.4 %. Further experimental investigations on different device configurations are needed in order to improve the photovoltaic performance of the NW–Graphene substrates.

7 Appendix

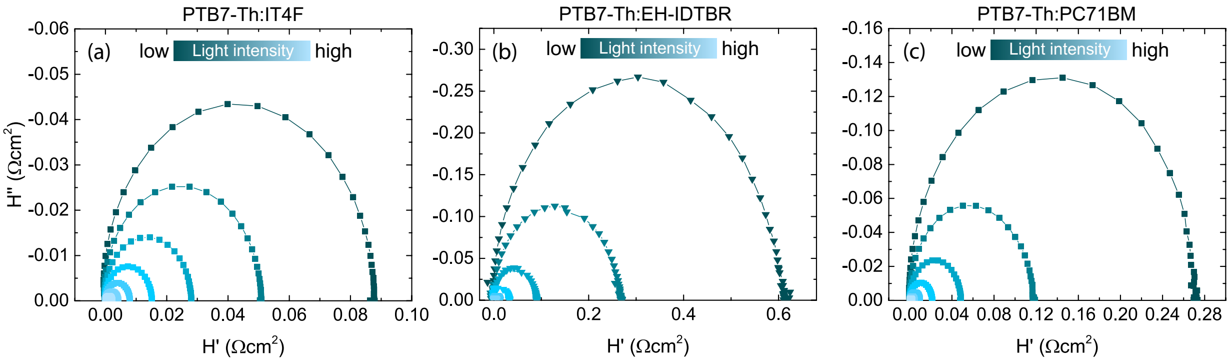

Figure 7.1: Intensity dependence of IMVS spectra measured at open circuit conditions for the PBDB-T-2F:acceptor solar cells represented as a Nyquist complex plane plot. The frequency range is between 1 Hz and 1 MHz. (a) PTB7–Th:IT4F 1:1 (w/w) (b) PTB7–Th:EH–IDTBR 1:2.5 (w/w) (c) PTB7–Th:PC71BM 1:1.5 (w/w).

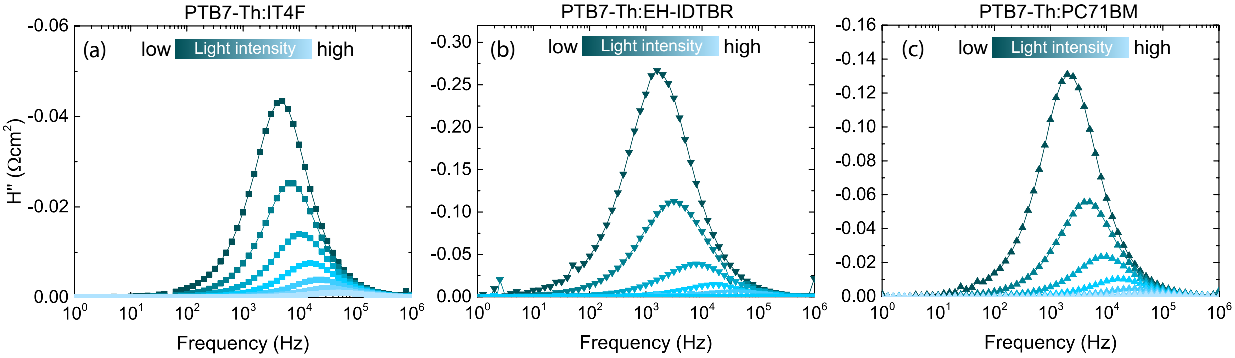

Figure 7.2: Intensity dependence of IMVS spectra measured at open circuit conditions for the three devices (a) PTB7–Th:IT4F 1:1 (w/w) (b) PTB7–Th:EH–IDTBR 1:2.5 (w/w) (c) PTB7–Th:PC71BM 1:1.5 (w/w), represented as Bode–plots of the imaginary components of the transfer function vs. the modulation frequency. The frequency range is between 1 Hz and 1 MHz.

References

[1] H. Akamatu and H. Inokuchi. "Electrical conductivity of the perylene bromine complex." In: (173 1954), pp. 168–169.

[2] C. W. Tang. "Two layer organic photovoltaic cell." In: (48 1986), p. 183.

[3] Martin a. Green. *Third generation photovoltaics: advanced solar energy conversion.* 2006. ISBN: 9783540265627. DOI: `10.1021/la100123q`.

[4] National Renewable Energy Laboratory. *Solar cell efficiency chart.* URL: `https://www.nrel.gov/pv/cell-efficiency.html` (visited on 10/01/2020).

[5] Sean E. Shaheen, David S. Ginley, and Ghassan E. Jabbour. "Organic-Based Photovoltaics: Toward Low-Cost Power Generation." In: *MRS Bulletin* (2005). ISSN: 0883-7694. DOI: `10.1557/mrs2005.2`.

[6] Nicole Bauer et al. "Comparing non-fullerene acceptors with fullerene in polymer solar cells: a case study with FTAZ and PyCNTAZ." In: *Journal of Materials Chemistry A* 5.10 (2017), pp. 4886–4893. ISSN: 20507496. DOI: `10.1039/c6ta10450a`. URL: `http://dx.doi.org/10.1039/C6TA10450A`.

[7] Qishi Liu et al. "18% Efficiency organic solar cells." In: *Science Bulletin* (2020). ISSN: 20959281. DOI: `10.1016/j.scib.2020.01.001`.

[8] Nieves Espinosa et al. "Solar cells with one-day energy payback for the factories of the future." In: *Energy and Environmental Science* 5.1 (2012), pp. 5117–5132. ISSN: 17545692. DOI: `10.1039/c1ee02728j`.

[9] M. Välimäki et al. "Custom-Shaped Organic Photovoltaic Modules—Freedom of Design by Printing." In: *Nanoscale Research Letters* 12.1 (2017). ISSN: 1556276X. DOI: `10.1186/s11671-017-1871-9`.

[10] Kenjiro Fukuda, Kilho Yu, and Takao Someya. *The Future of Flexible Organic Solar Cells.* 2020. DOI: `10.1002/aenm.202000765`.

[11] M. Plank. "Ueber das Gesetz der Energieverteilung im Normalspectrum." In: (4 1901), pp. 553–563.

[12] PVlighthouse. *Sun spectrum Caluclator.* URL: `https://www.pvlighthouse.com.au` (visited on 09/18/2018).

[13] Anna Köhler and Heinz Bässler. *Electronic processes in organic semiconductors: An introduction.* April. 2015, pp. 1–405. ISBN: 9783527685172. DOI: `10.1002/9783527685172`. eprint: `arXiv:1011.1669v3`. URL: `http://doi.wiley.com/10.1002/9783527685172`.

[14] Felix Nickel. “Herstellung und Charakterisierung mechanisch flexibler organischer Solarzellen durch Flüssigprozessierung.” 2014. ISBN: 978-3-7315-0399-6. DOI: 10.5445/KSP/1000047609.

[15] Wallace C. H. Choy. *Organic Solar Cells Materials and Device Physics*. London Heidlberg New York Dordrecht: Springer, 2006. ISBN: 978-1-4471-4822-7. DOI: 10.1007/978-1-4471-4823-4.

[16] Charles E. Mortimer and Ulrich Müller. *Basiswissen der Chemie*. Rüdigerstraße 14, 70469 Stuttgart: Georg Thieme Verlag, 2003. ISBN: 3-13-4843080. DOI: 10.1055/b-002-54081.

[17] Hui Huang and Jinsong Huang. *Organic and Hybrid Solar Cells*. London Heidlberg New York Dordrecht: Springer, 2014. ISBN: 978-3-319-10855-1. DOI: 10.1007/978-3-319-10855-1.

[18] Sung Heum Park et al. “Bulk heterojunction solar cells with internal quantum efficiency approaching 100%.” In: *Nature Photonics* 3 (Apr. 2009), p. 297.

[19] Jean Michel Nunzi. “Organic Photovoltaic Materials and Devices.” In: *C. R. Physique* 3 (2002), pp. 523–542.

[20] M. Knupfer. “Exciton binding energies in organic semiconductors.” In: *Applied Physics A* 77.5 (2003), pp. 623–626. ISSN: 1432-0630. DOI: 10.1007/s00339-003-2182-9. URL: https://doi.org/10.1007/s00339-003-2182-9.

[21] Peter Peumans, Aharon Yakimov, and Stephen R. Forrest. *Small molecular weight organic thin-film photodetectors and solar cells*. 2003. DOI: 10.1063/1.1534621.

[22] Attila J. Mozer and Niyazi S. Sariciftci. “Conjugated polymer photovoltaic devices and materials.” In: *C.R. Chimie* 9 (2006), pp. 568–577. DOI: 10.1016/j.crci.2005.03.033.

[23] G. Yu et al. “Polymer photovoltaic cells: Enhanced efficiencies via a network of internal donor-acceptor heterojunctions.” In: *Science* 270.5243 (1995), p. 1789. ISSN: 00368075. DOI: 10.1126/science.270.5243.1789.

[24] Jean Luc Brédas et al. “Charge-transfer and energy-transfer processes in π-conjugated oligomers and polymers: A molecular picture.” In: *Chemical Reviews* 104.11 (2004), pp. 4971–5003. ISSN: 00092665. DOI: 10.1021/cr040084k.

[25] Charles L. Braun. “Electric field assisted dissociation of charge transfer states as a mechanism of photocarrier production.” In: *The Journal of Chemical Physics* 80.9 (1984), pp. 4157–4161. DOI: 10.1063/1.447243. URL: https://doi.org/10.1063/1.447243.

[26] M. Schwoerer and H.C. Wolf. *Organische Molekulare Festkörper*. Berlin: Wiley-VCH, 2005.

[27] M.C. Scharber and N.S. Sariciftci. "Efficiency of bulk-heterojunction organic solar cells." In: *Progress in Polymer Science* 38.12 (2013). Topical issue on Conductive Polymers, pp. 1929–1940. ISSN: 0079-6700. URL: `http://www.sciencedirect.com/science/article/pii/S0079670013000427`.

[28] Naveen Kumar Elumalai and Ashraf Uddin. "Open circuit voltage of organic solar cells: An in-depth review." In: *Energy and Environmental Science* 9.2 (2016), pp. 391–410. ISSN: 17545706. DOI: `10.1039/c5ee02871j`. URL: `http://dx.doi.org/10.1039/c5ee02871j`.

[29] Thomas Kirchartz et al. "On the differences between dark and light ideality factor in polymer:Fullerene solar cells." In: *Journal of Physical Chemistry Letters* 4.14 (2013), pp. 2371–2376. ISSN: 19487185. DOI: `10.1021/jz4012146`.

[30] Pavel Schilinsky, Christoph Waldauf, and Christoph J. Brabec. "Recombination and loss analysis in polythiophene based bulk heterojunction photodetectors." In: *Applied Physics Letters* 81.20 (2002), pp. 3885–3887. ISSN: 00036951. DOI: `10.1063/1.1521244`.

[31] Juan Bisquert. *The Physics of Solar Cells: Perovskites, Organics, and Photovoltaic Fundamentals*. 2014, p. 226. ISBN: 9781138099968. DOI: `10.1002/9781119033769.ch5`.

[32] Peter Würfel. *Physics of Solar Cells - From Principles to New Concepts*. Weinheim: WILEY-VCH Verlag, 2005. ISBN: 3-527-40428-7.

[33] C. Brabec, V. Dyakonov, and U. Scherf. *Organic Photovoltaics: Materials, Device Physics, and Manufacturing Technologies*. 2nd Edition. Berlin Heidelberg New York: Wiley, 2014. ISBN: 978-3-527-33225-0.

[34] T. J. Coutts. "Thin film solar cells." In: *Thin Solid Films* 50.C (1978), pp. 99–117. ISSN: 00406090. DOI: `10.1016/0040-6090(78)90096-2`.

[35] PV Education. *Effect of Light Intensity*. URL: `https://www.pveducation.org/` (visited on 03/30/2020).

[36] Christopher M. Proctor and Thuc Quyen Nguyen. "Effect of leakage current and shunt resistance on the light intensity dependence of organic solar cells." In: *Applied Physics Letters* 106.8 (2015). ISSN: 00036951. DOI: `10.1063/1.4913589`. URL: `http://dx.doi.org/10.1063/1.4913589`.

[37] Arno Smets et al. *Solar Energy - The physics and engineering of photovoltaic conversion, technologies and systems*. Feb. 2016. ISBN: 9781906860325.

[38] Adam Pockett. "Characterization of Perovskite Solar Cells, Ph.D." PhD thesis. University of Bath, 2016.

[39] Juan Bisquert et al. “Electron Lifetime in Dye-Sensitized Solar Cells: Theory and Interpretation of Measurements.” In: *Journal of Physical Chemistry* 113 (2009), pp. 17278–17290. DOI: `10.1021/jp9037649`. URL: `https://pubs.acs.org/doi/10.1021/jp9037649`.

[40] Germà Garcia-Belmonte et al. “Simultaneous determination of carrier lifetime and electron density-of-states in P3HT:PCBM organic solar cells under illumination by impedance spectroscopy.” In: *Solar Energy Materials and Solar Cells* 94.2 (2010), pp. 366–375. ISSN: 09270248. DOI: `10.1016/j.solmat.2009.10.015`.

[41] V. Ern and R. E. Merrifield. “Magnetic field effect on triplet exciton quenching in organic crystals.” In: *Physical Review Letters* 21.9 (1968), pp. 609–611. ISSN: 00319007. DOI: `10.1103/PhysRevLett.21.609`.

[42] R.C.Johnson et al. “Effects of Magnetic Fields on the Mutual Annihilation of Triplet Excitons in Molecular Crystals.” In: 19.6 (1967), pp. 285–288.

[43] Bin Hu, Liang Yan, and Ming Shao. “Magnetic-field effects in organic semiconducting materials and devices.” In: *Advanced Materials* 21.14-15 (2009), pp. 1500–1516. ISSN: 09359648. DOI: `10.1002/adma.200802386`.

[44] A. S. Dhoot et al. “Triplet formation and decay in conjugated polymer devices.” In: *Chemical Physics Letters* 360.3-4 (2002), pp. 195–201. ISSN: 00092614. DOI: `10.1016/S0009-2614(02)00840-0`.

[45] D. R. McCamey et al. “Hyperfine-field-mediated spin beating in electrostatically bound charge carrier pairs.” In: *Physical Review Letters* 104.1 (2010), pp. 1–4. ISSN: 00319007. DOI: `10.1103/PhysRevLett.104.017601`.

[46] K. M. Salikhov et al. *Spin polarization and magnetic effects in radical reactions.* 1984.

[47] J. R. Lakowicz. *Principles of Fluorescence Spectroscopy.* 3rd edition. Baltimore USA: Springer Verlag, 2002. ISBN: 0-387-31278-1.

[48] Ulrich E. Steiner and Thomas Ulrich. *Magnetic Field Effects in Chemical Kinetics and Related Phenomena.* Vol. 89. 1. 1989, pp. 51–147. ISBN: 0009266518. DOI: `10.1021/cr00091a003`.

[49] R. G. Kepler et al. “Triplet excitons and delayed fluorescence in anthracene crystals.” In: *Physical Review Letters* 10.9 (1963), pp. 400–402. ISSN: 00319007. DOI: `10.1103/PhysRevLett.10.400`.

[50] Anna Köhler and David Beljonne. “The singlet-triplet exchange energy in conjugated polymers.” In: *Advanced Functional Materials* 14.1 (2004), pp. 11–18. ISSN: 1616301X. DOI: `10.1002/adfm.200305032`.

[51] Matthijs Cox. “Magnetism and Molecular Materials: Investigating magnetic field effects in organic semiconductors.” In: 2015 (2015), p. 155. URL: http://alexandria.tue.nl/extra2/785141.pdf.

[52] Zhihua Xu and Bin Hu. “Photovoltaic processes of singlet and triplet excited states in organic solar cells.” In: *Advanced Functional Materials* 18.17 (2008), pp. 2611–2617. ISSN: 1616301X. DOI: 10.1002/adfm.200800331.

[53] J. Frenkel. “On pre-breakdown phenomena in insulators and electronic semi-conductors.” In: *Physical Review* 54.8 (1938), pp. 647–648. ISSN: 0031899X. DOI: 10.1103/PhysRev.54.647.

[54] L. Onsager. “Initial recombination of ions.” In: *Physical Review* (1938). ISSN: 0031899X. DOI: 10.1103/PhysRev.54.554.

[55] Igor V. Khudyakov, Yuri A. Serebrennikov, and Nicholas J. Turro. “Spin-orbit coupling in free-radical reactions on the way to heavy elements.” In: *Chemical Reviews* 93.1 (1993), pp. 537–570. ISSN: 0009-2665. DOI: 10.1021/cr00017a023.

[56] William Shockley and Hans J. Queisser. “Detailed balance limit of efficiency of p-n junction solar cells.” In: *Journal of Applied Physics* (1961). ISSN: 00218979. DOI: 10.1063/1.1736034.

[57] Koen Vandewal et al. “Relating the open-circuit voltage to interface molecular properties of donor:acceptor bulk heterojunction solar cells.” In: *Physical Review B - Condensed Matter and Materials Physics* 81.12 (2010), pp. 1–8. ISSN: 10980121. DOI: 10.1103/PhysRevB.81.125204.

[58] Koen Vandewal et al. “On the origin of the open-circuit voltage of polymer-fullerene solar cells.” In: *Nature Materials* 8.11 (2009), pp. 904–909. ISSN: 14764660. DOI: 10.1038/nmat2548. URL: http://dx.doi.org/10.1038/nmat2548.

[59] K. Vandewal, J. Benduhn, and V. C. Nikolis. “How to determine optical gaps and voltage losses in organic photovoltaic materials.” In: *Sustainable Energy and Fuels* 2.3 (2018), pp. 538–544. ISSN: 23984902. DOI: 10.1039/c7se00601b.

[60] Koen Vandewal et al. “Efficient charge generation by relaxed charge-transfer states at organic interfaces.” In: *Nature Materials* 13.1 (2014), pp. 63–68. ISSN: 14761122. DOI: 10.1038/nmat3807. URL: http://dx.doi.org/10.1038/nmat3807.

[61] Jing Liu et al. “Fast charge separation in a non-fullerene organic solar cell with a small driving force.” In: *Nature Energy* 1.7 (2016), pp. 1–7. ISSN: 20587546. DOI: 10.1038/nenergy.2016.89.

[62] Jizhong Yao et al. “Quantifying losses in open-circuit voltage in solution-processable solar cells.” In: *Physical Review Applied* 4.1 (2015), pp. 1–10. ISSN: 23317019. DOI: 10.1103/PhysRevApplied.4.014020.

[63] Uwe Rau. “Reciprocity relation between photovoltaic quantum efficiency and electroluminescent emission of solar cells.” In: *Physical Review B - Condensed Matter and Materials Physics* 76.8 (2007), pp. 1–8. ISSN: 10980121. DOI: `10.1103/PhysRevB.76.085303`.

[64] Li Yan et al. “Effect of PEI cathode interlayer on work function and interface resistance of ITO electrode in the inverted polymer solar cells.” In: *Organic Electronics* 17 (2015), pp. 94–101. ISSN: 15661199. DOI: `10.1016/j.orgel.2014.11.023`. URL: `http://dx.doi.org/10.1016/j.orgel.2014.11.023`.

[65] Lin Hu et al. “Chemical reaction between an ITIC electron acceptor and an amine-containing interfacial layer in non-fullerene solar cells.” In: *Journal of Materials Chemistry A* (2018). ISSN: 20507496. DOI: `10.1039/c7ta10306a`.

[66] Yanming Sun et al. “Inverted polymer solar cells integrated with a low-temperature-annealed sol-gel-derived ZnO film as an electron transport layer.” In: *Advanced Materials* (2011). ISSN: 09359648. DOI: `10.1002/adma.201004301`.

[67] Vishal Shrotriya et al. “Transition metal oxides as the buffer layer for polymer photovoltaic cells.” In: *Applied Physics Letters* 88.7 (2006), pp. 1–4. ISSN: 00036951. DOI: `10.1063/1.2174093`.

[68] Desalegn Alemu et al. “Highly conductive PEDOT:PSS electrode by simple film treatment with methanol for ITO-free polymer solar cells.” In: *Energy and Environmental Science* 5.11 (2012), pp. 9662–9671. ISSN: 17545692. DOI: `10.1039/c2ee22595f`.

[69] Wenxia Zhang et al. “Graphene:silver nanowire composite transparent electrode based flexible organic solar cells with 13.4% efficiency.” In: *Journal of Materials Chemistry A* 7.38 (2019), pp. 22021–22028. ISSN: 20507496. DOI: `10.1039/c9ta07493g`.

[70] Zhi Guo Zhang et al. “Perylene diimides: A thickness-insensitive cathode interlayer for high performance polymer solar cells.” In: *Energy and Environmental Science* 7.6 (2014), pp. 1966–1973. ISSN: 17545706. DOI: `10.1039/c4ee00022f`.

[71] Wenchao Zhao et al. “Molecular Optimization Enables over 13% Efficiency in Organic Solar Cells.” In: *Journal of the American Chemical Society* 139.21 (2017), pp. 7148–7151. ISSN: 15205126. DOI: `10.1021/jacs.7b02677`.

[72] Yuze Lin et al. “An electron acceptor challenging fullerenes for efficient polymer solar cells.” In: *Advanced Materials* (2015). ISSN: 15214095. DOI: `10.1002/adma.201404317`.

[73] Katharina Reichenbächer, Heike I. Süss, and Jürg Hulliger. *Fluorine in crystal engineering - "The little atom that could"*. 2005. DOI: `10.1039/b406892k`.

[74] Jianhui Hou et al. *Organic solar cells based on non-fullerene acceptors*. 2018. DOI: `10.1038/NMAT5063`.

[75] Maojie Zhang et al. "A Large-Bandgap Conjugated Polymer for Versatile Photovoltaic Applications with High Performance." In: (2015), pp. 4655–4660. DOI: `10.1002/adma.201502110`.

[76] M. T. Dang, L. Hirsch, and G. Wantz. "P3HT:PCBM, best seller in polymer photovoltaic research." In: *Advanced Materials* 23.31 (2011), pp. 3597–3602. ISSN: 09359648. DOI: `10.1002/adma.201100792`.

[77] Jan C. Hummelen et al. "Preparation and Characterization of Fulleroid and Methanofullerene Derivatives." In: *The Journal of Organic Chemistry* 60.3 (1995), pp. 532–538. DOI: `10.1021/jo00108a012`. URL: `https://doi.org/10.1021/jo00108a012`.

[78] Sarah Holliday et al. "High-efficiency and air-stable P3HT-based polymer solar cells with a new non-fullerene acceptor." In: *Nature Communications* 7 (2016), pp. 1–11. ISSN: 20411723. DOI: `10.1038/ncomms11585`.

[79] Derya Baran et al. "Robust nonfullerene solar cells approaching unity external quantum efficiency enabled by suppression of geminate recombination." In: *Nature Communications* 9.1 (2018), pp. 1–9. ISSN: 20411723. DOI: `10.1038/s41467-018-04502-3`. URL: `http://dx.doi.org/10.1038/s41467-018-04502-3`.

[80] Sih Hao Liao et al. "Fullerene derivative-doped zinc oxide nanofilm as the cathode of inverted polymer solar cells with low-bandgap polymer (PTB7-Th) for high performance." In: *Advanced Materials* 25.34 (2013), pp. 4766–4771. ISSN: 09359648. DOI: `10.1002/adma.201301476`.

[81] Quantum Design. *PPMS Dynacool.* URL: `https://www.qdusa.com/products/dynacool.html` (visited on 03/24/2020).

[82] R. N. Jagtap and A. H. Ambre. *Atomic force microscopy (AFM): Basics and its important applications for polymer characterization: An overview.* 2005.

[83] Martin Kaltenbrunner et al. "Flexible high power-per-weight perovskite solar cells with chromium oxide-metal contacts for improved stability in air." In: *Nature Materials* 14.10 (2015), pp. 1032–1039. ISSN: 14764660. DOI: `10.1038/nmat4388`.

[84] Ruixiang Peng et al. "Interface bonding engineering of a transparent conductive electrode towards highly efficient and mechanically flexible ITO-free organic solar cells." In: *Journal of Materials Chemistry A* 7.18 (2019), pp. 11460–11467. ISSN: 20507496. DOI: `10.1039/c9ta02900a`.

[85] Xiaomin Xu et al. "Thermally stable, highly efficient, ultraflexible organic photovoltaics." In: *Proceedings of the National Academy of Sciences of the United States of America* (2018). ISSN: 10916490. DOI: `10.1073/pnas.1801187115`.

[86] Deping Qian et al. “Design rules for minimizing voltage losses in high-efficiency organic solar cells.” In: *Nature Materials* (2018). ISSN: 14764660. DOI: `10.1038/s41563-018-0128-z`.

[87] Craig H. Peters et al. “The mechanism of burn-in loss in a high efficiency polymer solar cell.” In: *Advanced Materials* 24.5 (2012), pp. 663–668. ISSN: 09359648. DOI: `10.1002/adma.201103010`.